Investigating Anisotropies in the Local Universe with Type Ia Supernovae from the Nearby Supernova Factory

Dissertation
zur
Erlangung des Doktorgrades (Dr. rer. nat.)
der
Mathematisch-Naturwissenschaftlichen Fakultät
der
Rheinischen Friedrich-Wilhelms-Universität Bonn

von
Ulrich Feindt
aus
Krefeld

Bonn, 12.06.2015

Dieser Forschungsbericht wurde als Dissertation von der Mathematisch-Naturwissenschaftlichen Fakultät der Universität Bonn angenommen und ist auf dem Hochschulschriftenserver der ULB Bonn `http://hss.ulb.uni-bonn.de/diss_online` elektronisch publiziert.

1. Gutachter:	Prof. Dr. Marek Kowalski
2. Gutachter:	Prof. Dr. Cristiano Porciani
Tag der Promotion:	30.10.2015
Erscheinungsjahr:	2016

Contents

CHAPTER 1

Introduction

The Copernican principle, which postulates that we are not located in a special location of the universe, is a key axiom of modern cosmology. Combined with the observation that the properties of the universe are independent of the direction in which it is observed (isotropy), the principle implies that the universe should have the same properties at all locations (homogeneity). These basic symmetries of the universe were essential for the development of the Friedmann-Lemaître-Robertson-Walker (FLRW) metric that we use today as the standard description of the evolution of the universe. However, since we observe deviations from the homogeneity on small scales in the form of stars, planets and galaxies, these strict notions have been replaced by the cosmological principle, according to which the universe is statistically homogeneous and isotropic on sufficiently large scales.

Within the standard model of cosmology, ΛCDM, the formation of the observed structure can be explained as the growth of initially small fluctuations of the density through gravitational collapse. This sets limits on the amplitude of the inhomogeneities and anisotropies that are expected in the universe. Therefore, it is important to explain one of the strongest observed anisotropies, the dipole anisotropy of the cosmic microwave background (CMB), which is two orders of magnitude larger than the other multipole moments of the fluctuations. The dipole is commonly accepted to originate from the motion of our Local Group of galaxies with a velocity of $627 \pm 22\,\mathrm{km\,s^{-1}}$ relative to the rest-frame, in which the CMB is isotropic (Kogut et al., 1993).

Large velocities are naturally explained by the infall to more massive regions such as superclusters, i.e. groups of galaxy clusters. About a quarter of the Local Group motion is explained by the Virgo cluster (Jerjen & Tammann, 1993), the closest galaxy cluster at a distance of 16 Mpc[1], which is now considered part of the same structure as the Local Group, the Laniakea supercluster (Tully et al., 2014). The next closest mass concentrations behind the Virgo cluster are the clusters in the constellations Centaurus, Hydra and Norma near the centre of Laniakea. This region is also referred to as the Great Attractor and has been first proposed as the source of the missing velocity nearly three decades ago by Lynden-Bell et al. (1988). However, it is located behind the Milky Way and thus difficult to observe in visible light due to extinction by dust. An X-ray survey of this so called zone of avoidance has shown that only 44% of the Local Group motion originates from the attractors in that region (Kocevski & Ebeling, 2006); the remaining velocity is caused by superclusters with similar directions but at greater distances, e.g. the Shapley supercluster centred at a distance of ~ 200 Mpc (redshift $z \sim 0.046$), three to four times as far away from us the Great Attractor.

---

[1] $1\,\mathrm{Mpc} = 3.26 \times 10^{6}$ light years $= 3.09 \times 10^{22}$ m

On scales beyond the Great Attractor, the peculiar velocity data start to become too sparse and noisy to reconstruct the full velocity field but a coherent motion of the local volume can still be constrained. Based on such a bulk flow, the mass outside the observed volume can be constrained. Previous studies of the local bulk flow have found contradicting values. While one set of analyses found a possibly anomalously large flow on scales $\sim 150\,\mathrm{Mpc}$ ($z \sim 0.035$) (Hudson et al., 2004; Feldman et al., 2010; Lavaux et al., 2010; Macaulay et al., 2012), the other v(Courteau et al., 2000; Nusser & Davis, 2011; Turnbull et al., 2012; Ma & Pan, 2014) found lower values on the same scale, which are consistent with the expectations from the current theory of structure formation.

On scales between 300 and 800 Mpc ($0.07 < z < 0.2$), at which the coherent velocity dipole is expected to be $\lesssim 100\,\mathrm{km\,s^{-1}}$, recent studies have detected an even larger bulk flow of $\sim 1000\,\mathrm{km\,s^{-1}}$ that cannot be explained by any known structure (Kashlinsky et al., 2008, 2009, 2010). Such a "dark flow" could point towards extensions of the standard ΛCDM model in the form of pre-inflationary structure that imprints a tilt on the horizon, which would be observed as a velocity dipole that remains constant on all scales (Grishchuk & Zeldovich, 1978; Turner, 1991). The discovery of the dark flow is based on the kinematic component of the Sunyaev-Zeldovich (SZ) effect, which describes the distortion of CMB photons passing through hot gas in galaxy clusters (Zeldovich & Sunyaev, 1969). Other studies of this effect have so far failed to reproduce the dark flow signal. Recently using the results of the Planck Mission (Planck Collaboration Int. XIII, 2014; Hernández-Monteagudo et al., 2015), which constrained the velocities to $\lesssim 250\,\mathrm{km\,s^{-1}}$ at the 95% confidence level. However, Atrio-Barandela (2013) has argued that the differences are due to the choice of methods and not the new data and reports that the dark flow is still detectable in Planck data (Atrio-Barandela et al., 2015). Therefore, it is important to study the bulk flow on these scales using independent data.

In early studies of the local peculiar velocity field, observations of galaxies were used to measure the motion because they are easy to observe in larger numbers and good precision up to redshifts $z \sim 0.05$. This requires knowledge of the cosmological redshift due to Hubble expansion and an independent distance estimate. Since the peculiar motion introduces an additional Doppler shift of the spectral lines, it can be detected as a deviation from the Hubble law. The distances to galaxies are estimated using the Tully-Fisher relation (Tully & Fisher, 1977), the fundamental plane (Djorgovski & Davis, 1987; Dressler et al., 1987) or surface brightness fluctuations (Tonry & Schneider, 1988). However, galaxies as peculiar velocity indicators range out around the distance to the Shapley supercluster because of decreasing accuracy at increasing observational cost. Type Ia supernovae (SNe Ia), on the other hand, are observable to distances far beyond the local structure. After an empirical correction for lightcurve width and colour (Phillips, 1993), they constrain distance up to five times more accurately than galaxies. An early study using nearby SNe Ia found a Local Group motion consistent with the CMB dipole (Riess et al., 1995) based on a very small dataset of 13 SNe. Since then the size of the SN Ia dataset at redshifts ($z < 0.03$) has grown by an order of magnitude and this result has been confirmed at higher significance (Haugbølle et al., 2007; Gordon et al., 2008; Weyant et al., 2011; Colin et al., 2011; Turnbull et al., 2012). However, the existing SN Ia data is still sparse at redshifts immediately beyond that and up to $z \sim 0.1$.

This thesis presents a study of bulk flows and anisotropy in the local universe using the Union2 compilation (Amanullah et al., 2010) and a dataset of 117 SNe Ia from the Nearby Supernova Factory (SNFACTORY, Aldering et al. 2002), a project that aims to obtain a large set of spectrophotometrically observed SNe Ia in the redshift range $0.03 < z < 0.08$. The SNFACTORY dataset more than doubles the number of distance measurements on this scale, providing a considerably better sensitivity to bulk flows behind the Shapley supercluster and at the distances, at which the dark flow was detected. The starting point for this analysis are the results of Colin et al. (2011), who analysed the Union2 data in discrete redshift shells and observed a possible backside infall into the Shapley supercluster. The analysis is extended by a simple attractor model to study this supercluster and concludes with simulation of future surveys like the Zwicky Transient Facility (ZTF). Part of the results presented here have previously been published in Feindt et al. (2013).

The document is organized as the follows: Chapter 2 reviews the standard theory for the evolution of the universe. In chapter 3 methods to measure peculiar distances and velocities are reviewed along with the current results from other studies. The data and model used in this analysis are discussed in chapters 4 and 5, respectively. In chapter 6 the results for models of a dipole anisotropy are present, while the results for a gravitational attractor model are discussed in chapter 7. Chapter 8 presents simulations for future surveys. The final chapter 9 summarizes this thesis and gives an outlook for future studies.

CHAPTER 2

Cosmological Standard Model

Cosmology is the science describing the whole universe, aiming to explain its origin and evolution, and the underlying physical processes. This chapter summarizes the fundamental theory for cosmology, starting with a homogeneous and isotropic universe and then describing how structure formation can be derived with this framework. The various definitions of distance that arise in an expanding universe are described. Finally, the effect of peculiar velocities on distance measurements is derived. This is the basic quantity that will be used in the analyses of this thesis.

2.1 The Cosmological Principle

Our current understanding of the universe is based on the *cosmological principle*, the fundamental assumption that the universe is homogeneous and isotropic, i.e. invariant under translation and rotation. This assumption is only valid on large scales as demonstrated by sky surveys such as the Two-degree-Field Galaxy Redshift Survey (2dFGRS)[1] or the Sloan Digital Sky Survey (SDSS)[2], while it breaks down on smaller scales smaller than 100 Mpc. These symmetries are only imposed on the spatial component of cosmological models, not on the whole space-time. This allows us to study the evolution of the universe.

2.2 The Universe in General Relativity

Physical cosmology is a comparably young science. It developed in the early 20th century after the publication of Einstein's general theory of relativity (GR), which showed that gravity can be expressed as a curved spacetime caused by any energy density. As a consequence, the evolution of the universe can be shown to depend directly on the energy density and pressure in the universe.

2.2.1 Einstein Equation

In GR the curvature of spacetime is described using four-dimensional metric tensor $g_{\mu\nu}$ that defines an invariant differential of distance $\mathrm{d}s$:

$$\mathrm{d}s^2 = g_{\mu\nu}\mathrm{d}x^\mu x^\nu. \tag{2.1}$$

---

[1] `http://2dfgrs.net/`

[2] `http://sdss.org/`

The metric is related to the densities of energy and momentum by Einstein's field equation:

$$R_{\mu\nu} - \frac{1}{2} g_{\mu\nu} R = -8\pi G T_{\mu\nu} + \Lambda g_{\mu\nu}, \tag{2.2}$$

where G is Newton's gravitational constant, $R_{\mu\nu}$ the Ricci curvature tensor and $T_{\mu\nu}$ the energy-momentum tensor. The cosmological constant Λ was introduced by Einstein in order to obtain a static solution to the equation, i.e. a static model of the universe (Einstein, 1917). Due to the discoveries of cosmological expansion by Lemaître (1927) and Hubble (1929), Einstein later abandoned this assumption. Recently, however, the cosmological constant become of great theoretical and empirical interest after the discovery that the expansion of the universe is accelerating (Riess et al. 1998; Perlmutter et al. 1999, see section 3.2.1).

2.2.2 FLRW Metric

Within GR, the most basic model describing a spatially homogeneous and isotropic universe evolving in time is the Friedmann-Lemaître-Robertson-Walker (FLRW) metric (Friedmann, 1922; Lemaître, 1927; Robertson, 1929; Walker, 1933):

$$\mathrm{d}s^2 = c^2 \mathrm{d}t^2 - a^2(t) \left[\mathrm{d}\chi^2 + \mathcal{F}_K^2(\chi) \left(\mathrm{d}\theta^2 + \sin^2\theta \mathrm{d}\phi^2 \right) \right], \tag{2.3}$$

where $a(t)$ is the scale factor of the universe (set to $a(t_0) = 1$ for today[3]), χ is a comoving radial coordinate in units of length, θ and ϕ are angular coordinates and K is the curvature of the universe in units of length^{-2}. $\mathcal{F}(\chi)$ is the comoving angular diameter distance, which depends on K:

$$\mathcal{F}(\chi) = \begin{cases} \sqrt{|K|}^{-1} \sin\left(\sqrt{|K|}\chi \right) & \text{for } K > 0 \\ \chi & \text{for } K = 0 \ . \\ \sqrt{|K|}^{-1} \sinh\left(\sqrt{|K|}\chi \right) & \text{for } K < 0 \end{cases} \tag{2.4}$$

The different cases for K distinguish closed (spherical), flat and open (hyperbolic or "saddle-like") universes, respectively. In a universe with FLRW metric distances between objects (e.g. galaxies) will increase (or decrease in case of a collapsing universe) according to the temporal evolution of the scale-factor $a(t)$. Therefore, the further an object is located from an observer, the faster it will appear to recede. This recession can be observed as a Doppler shift of the light emitted by the object. This effect can be related to the scale factor to the FLRW metric (2.3) along a radial geodesic. Suppose that an object emits two flashes of light at t and $t + \Delta t_{\mathrm{em}}$, which are received at t_0 and $t_0 + \Delta t_{\mathrm{obs}}$. Assuming that the Δt's are small compared to $t_0 - t$, and that $a(t)$ does not change significantly in the time between the flashes, one finds that:

$$\int_t^{t_0} \frac{c\mathrm{d}t'}{a(t')} = \int_{t+\Delta t_{\mathrm{em}}}^{t_0+\Delta t_{\mathrm{obs}}} \frac{c\mathrm{d}t'}{a(t')} = \int_t^{t_0} \frac{c\mathrm{d}t'}{a(t')} + \frac{c\Delta t_{\mathrm{obs}}}{a(t_0)} - \frac{c\Delta t_{\mathrm{em}}}{a(t)}. \tag{2.5}$$

---

[3] The subscript 0 will be used throughout this document to denote the current value of a quantity, e.g. the age of the universe t_0, unless noted otherwise.

Since $a(t_0) = 1$, this means that Δt_{em} is stretched along the way to the observer by a factor $1/a(t)$ and therefore the observed frequency of the light decreases:

$$\frac{\Delta t_{\mathrm{em}}}{\Delta t_{\mathrm{obs}}} = \frac{\nu_{\mathrm{em}}}{\nu_{\mathrm{obs}}} = \frac{\lambda_{\mathrm{obs}}}{\lambda_{\mathrm{em}}} = \frac{1}{a(t)} = 1 + z, \tag{2.6}$$

where z is called the *cosmological redshift*. Thus, the properties of an object's spectrum, viz. the shifted positions of spectral lines, are a direct probe of the scale factor of the universe at the time of emission.

2.2.3 Friedmann Equations

Applying the cosmological principle to the energy-momentum tensor $T_{\mu\nu}$, the distribution of energy in the universe is approximated as a perfect fluid with

$$T_{\mu\nu} = (\rho + pc^2)u_\mu u_\nu - pc^2 g_{\mu\nu}, \tag{2.7}$$

where ρ is the energy density, p the pressure and $u = (1, 0, 0, 0)$ a velocity 4-vector. For the FLRW metric the $(0, 0)$-component of the Ricci tensor and the Ricci scalar becomes:

$$R_{00} = 3\frac{\ddot{a}}{a} \tag{2.8}$$

$$R = \frac{6}{c^2 a^2}(a\ddot{a} + \dot{a}^2 + Kc^2) \tag{2.9}$$

Combining this using Einstein's field equation (2.2), one finds an equation for the temporal evolution of the scale factor:

$$\begin{aligned} 3\left(\frac{\dot{a}}{a}\right)^2 + 3\frac{Kc^2}{a^2} &= 8\pi G\rho + \Lambda c^2 \\ \Rightarrow H^2 \equiv \left(\frac{\dot{a}}{a}\right)^2 &= \frac{8\pi G}{3}\rho + \frac{\Lambda c^2}{3} - \frac{Kc^2}{a^2}, \end{aligned} \tag{2.10}$$

where H is called the *Hubble parameter* and the equation is called the *the first Friedmann equation* (Friedmann, 1922).

To solve this equation, knowledge of the evolution of the density ρ is required. Due to conservation of energy the energy-momentum tensor must have a vanishing divergence. From this follows that

$$\begin{aligned} 0 &= \nabla_\mu T^\mu{}_0 \\ &= -\dot{\rho} - 3\frac{\dot{a}}{a}\left(\rho + \frac{p}{c^2}\right). \end{aligned} \tag{2.11}$$

By further assuming that density and pressure are related by an equation of state $p = w\rho c^2$ with a constant parameter w, this is simplified to

$$\frac{\dot{\rho}}{\rho} = -3(1 + w)\frac{\dot{a}}{a} \tag{2.12}$$

with the general solution

$$\rho \propto a^{-3(1+w)}. \tag{2.13}$$

By differentiating the first Friedmann equation (2.10) in time and substituting equation (2.11), a relation between density, pressure and the acceleration of the expansion of the universe can be found:

$$\frac{\ddot{a}}{a} = \frac{4\pi}{3}\left(\rho + 3\frac{p}{c^2}\right) + \frac{\Lambda c^2}{3} \tag{2.14}$$

This equation is called the *second Friedmann equation*.

2.2.4 Energy Content of the Universe

Three basic cases of energy densities – distinguished by their equation-of-state parameters w – are of particular importance in cosmology:

- matter ($w = 0, \rho_\mathrm{m} \propto a^{-3}$): non-relativistic matter only contributes to the energy density through its rest mass. Therefore, the density decreases proportionally to the volume, i.e. the cube of the scale factor.
- radiation ($w = 1/3, \rho_\mathrm{r} \propto a^{-1}$): photons (and other light ultra-relativistic particles) have a significant kinetic energy that contributes to the energy density. The radiation density decreases faster than that of matter because the photons lose energy when they are redshifted, reducing the energy by an additional factor of a.
- vacuum energy ($w = -1, \rho_\Lambda = \text{const.}$): an energy density of the vacuum that does not dilute for larger scale factors but remains constant. Such an energy provides negative pressure that accelerates the expansion of the universe. It can be related to Einstein's cosmological constant by $\rho_\Lambda = \Lambda c^2/(8\pi G)$.

It is convenient to express all energy densities in units of the *critical density*, which depends on the *Hubble constant* H_0, i.e. the current value of the Hubble parameter $H = \dot{a}/a$:

$$\rho_\mathrm{cr} = \frac{3H_0^2}{8\pi G}. \tag{2.15}$$

Based on this density the curvature cases of the FLRW metric can be distinguished: for $\rho_\mathrm{total} > \rho_\mathrm{cr}$ (including ρ_Λ) the universe is closed, for $\rho_\mathrm{total} = \rho_\mathrm{cr}$ it is flat and for $\rho_\mathrm{total} < \rho_\mathrm{cr}$ it is open. This characteristic scale can be used to define dimensionless density parameters Ω:

$$\Omega_\mathrm{m} = \frac{\rho_\mathrm{m,0}}{\rho_\mathrm{cr}}; \quad \Omega_\mathrm{r} = \frac{\rho_\mathrm{r,0}}{\rho_\mathrm{cr}}; \quad \Omega_\Lambda = \frac{\rho_\Lambda}{\rho_\mathrm{cr}}. \tag{2.16}$$

Using these parameters the Friedmann equation becomes

$$H^2 = \left(\frac{\dot{a}}{a}\right) = H_0^2\left(\Omega_\mathrm{r}a^{-4} + \Omega_\mathrm{m}a^{-3} + \Omega_\mathrm{k}a^{-2} + \Omega_\Lambda\right) \tag{2.17}$$

with $\Omega_\mathrm{k} = 1 - \Omega_\mathrm{r} + \Omega_\mathrm{m} + \Omega_\Lambda = -Kc^2/H_0^2$.

If one of the density parameters is significantly larger than the others, i.e. it *dominates* the total energy of the universe, the Friedmann equation can be simplified and becomes analytically solvable for a flat universe ($\Omega_\mathrm{total} = 1$):

$$a(t) \propto \begin{cases} t^{1/2} & \text{(radiation-dominated)} \\ t^{2/3} & \text{(matter-dominated)} \\ e^{H_0 t} & \text{(vacuum-energy-dominated).} \end{cases} \tag{2.18}$$

Since the densities evolve differently with the scale factor, the universe will go through phases dominated by each density: first radiation, then matter and lastly vacuum energy, which will cause the expansion to accelerate.

In a more general description of the universe, the vacuum energy/cosmological constant can be replaced by a *dark energy* density that has an arbitrary equation-of-state parameter w. While the observation that the universe is expanding acceleratedly requires $w < -1/3$ according to the second Friedmann equation (2.14), it need not necessarily be exactly -1. In fact, interpreting acceleration as a vacuum energy requires a large amount of fine tuning[4]. Since the nature of dark energy is not the subject of this work and the exact value of w has little effect within the studied distance range, $w = -1$ will be assumed throughout this document.

2.3 Structure Formation

The FLRW model explicitly assumes that the universe is homogeneous and isotropic but as mentioned in section 2.1, this assumptions is not valid on small scales. In fact the universe is strongly inhomogeneous as evidenced by the existence of structures like galaxies and stars. Furthermore the CMB anisotropies show that the universe was not perfectly homogeneous at early times, either. Due to gravitational instability, these initial perturbation will grow into the large-scale structure that can be observed now.

As long as the perturbation of the density $|\Delta\rho|/\bar{\rho} \ll 1$, its evolution can be calculated using linear perturbation theory, which can be solved analytically. This is justified for large structures or at early time because the CMB anisotropies are small ($\Delta T/T \sim 10^{-5}$). On smaller scales the perturbations become non-linear and must be simulated numerically. Since non-linear structure formation is not relevant to the analyses presented in this document, it will not be described here. Instead this section will only give a short summary of linear structure formation theory; for further details see Peebles (1980) and Strauss & Willick (1995).

In general, the matter density can be described as a fluid with a well-defined velocity field $\boldsymbol{u}$. Its evolution is governed by the fluid equations of mass continuity, force and gravitation:

$$\frac{\partial \rho}{\partial t} + \nabla_r \cdot (\rho \boldsymbol{u}) = 0 \tag{2.19}$$

$$\frac{\partial \boldsymbol{u}}{\partial t} + (\boldsymbol{u} \cdot \nabla_r)\boldsymbol{u} = -\nabla_r \phi \tag{2.20}$$

$$\nabla_r^2 \phi = 4\pi G \rho \tag{2.21}$$

where ϕ is the gravitational potential and the spatial derivatives are by proper distance r. We are interested in structure formation at a time when the radiation energy density has become insignificant relative to non-relativistic matter. Therefore, the terms depending on pressure were assumed to be negligible and ρ was used for the matter density (dropping the subscript used in section 2.2.4). The equations can now be transformed to comoving coordinates $\boldsymbol{x}$ defined as:

$$\boldsymbol{x} = \frac{\boldsymbol{r}}{a(t)}. \tag{2.22}$$

The time-derivative of $\boldsymbol{r}$ consists of two velocity terms:

$$\dot{\boldsymbol{r}} = \dot{a}\boldsymbol{x} + a\dot{\boldsymbol{x}} = H(t)\boldsymbol{r} + \boldsymbol{v}. \tag{2.23}$$

---

[4] Estimates of the vacuum energy density from particle physics are typically 120 (!) orders of magnitude off (see e.g. Rugh & Zinkernagel 2000).

The first term corresponds to the Hubble expansion while the other defines the *peculiar velocity* $v = a(t)\dot{\boldsymbol{x}}$. Furthermore one can define the *density contrast* δ and the comoving gravitational potential Φ:

$$\delta(\boldsymbol{x}, t) = \frac{\rho(\boldsymbol{x}, t)}{\bar{\rho}(t)} - 1 \tag{2.24}$$

$$\Phi(\boldsymbol{x}, t) = \phi(a\boldsymbol{x}, t) + \frac{a\ddot{a}}{2}|\boldsymbol{x}|^2 \tag{2.25}$$

In comoving coordinates equations (2.19)–(2.21) become:

$$\frac{\partial \delta}{\partial t} + \frac{1}{a}\nabla_x \cdot [(1+\delta)\boldsymbol{v}] = 0 \tag{2.26}$$

$$\frac{\partial \boldsymbol{v}}{\partial t} + \frac{\dot{a}}{a}\boldsymbol{v} + \frac{1}{a}(\boldsymbol{v} \cdot \nabla_x)\boldsymbol{v} = -\frac{1}{a}\nabla_x \Phi \tag{2.27}$$

$$\nabla_x^2 \Phi = 4\pi G a^2 \bar{\rho} \delta = \frac{3H_0^2 \Omega_\mathrm{m}}{2a}\delta \tag{2.28}$$

where the facts that $\bar{\rho}(t) \propto a(t)^{-3}$ and that $\nabla_r = a(t)^{-1}\nabla_x$ were used as well as the second Friedmann equation (2.14), according to which

$$\nabla_r \left(\frac{a\ddot{a}}{2}|\boldsymbol{x}|^2 \right) = 3\frac{\ddot{a}}{a} = -4\pi G \bar{\rho}. \tag{2.29}$$

While equations (2.26)–(2.28) are exact in the Newtonian regime, the first two of them are non-linear and cannot be solved analytically. For $\delta \ll 1$ one can, however, linearize the equations to:

$$\frac{\partial \delta}{\partial t} + \frac{1}{a}\nabla_x \cdot \boldsymbol{v} = 0, \tag{2.30}$$

$$\frac{\partial \boldsymbol{v}}{\partial t} + \frac{\dot{a}}{a}\boldsymbol{v} = -\frac{1}{a}\nabla_x \Phi. \tag{2.31}$$

The time derivative of (2.30) and the divergence of (2.31) both contain $\nabla_x \cdot \partial \boldsymbol{v}/\partial t$, they can be combined to

$$\frac{\partial^2 \delta}{\partial t^2} - 2\frac{\dot{a}}{a^2}\nabla_x \cdot \boldsymbol{v} - \frac{1}{a}\nabla_x^2 \Phi = 0, \tag{2.32}$$

which becomes

$$\frac{\partial^2 \delta}{\partial t^2} - 2\frac{\dot{a}}{a}\frac{\partial \delta}{\partial t} - \frac{3H_0^2 \Omega_\mathrm{m}}{2a^3}\delta = 0. \tag{2.33}$$

This equation only contains derivatives with respect to time. Therefore, the general form of δ has the shape

$$\delta(\boldsymbol{x}, t) = D_1(t)\Delta_1(\boldsymbol{x}) + D_2(t)\Delta_2(\boldsymbol{x}). \tag{2.34}$$

Closed forms for the functions $D_{1,2}$ can be found in Peebles (1980). Since one of these functions is found to decrease monotonically while the other increases, they are commonly referred to as *decaying* and *growing* modes $D_\pm$. Therefore, only one of the solutions, the growing mode D_+, contributes to the formation of structure over a long time and hence it will just be called D from here on.

The *growth factor* f is defined as

$$f \equiv \frac{\mathrm{d}\ln D}{\mathrm{d}\ln a} = \frac{\dot{D}}{HD}. \tag{2.35}$$

Equation (2.30) now becomes:

$$\nabla_x \cdot \boldsymbol{v} = -a\delta\frac{\dot{D}}{D} = -aHf\delta. \tag{2.36}$$

The growth factor f depends on the cosmological parameters, mostly on Ω_m. A good approximation, which is adopted here, is found in Linder (2005):

$$f \simeq \Omega_\mathrm{m}^\gamma \tag{2.37}$$

where the exponent γ depends on the dark energy equation of state parameter w at redshift $z = 1$

$$\gamma = 0.55 + 0.05(1 + w(z = 1)). \tag{2.38}$$

In this document $w = -1$ — and thus $f = \Omega_\mathrm{m}^{0.55}$ — will be assumed consistently. Equation (2.36) has the same shape as Gauss's flux theorem and its solution therefore is

$$\boldsymbol{v}(\boldsymbol{x}) = \frac{afH}{4\pi}\int\frac{\boldsymbol{y}-\boldsymbol{x}}{|\boldsymbol{y}-\boldsymbol{x}|^3}\delta(\boldsymbol{y})\mathrm{d}^3\boldsymbol{y}. \tag{2.39}$$

Thus, peculiar velocity data can be used to map the density contrast in the universe. The derivation of peculiar velocities from cosmological observations is covered in section 2.4.2.

2.4 Cosmological Observables

Section 2.2 introduced the redshift as a fundamental observable of objects at cosmological distances. However, since it only depends on the scale factor at the time of light emission, it cannot be used to determine cosmological parameters by itself. Instead, it must be compared to other quantities that depend on the cosmological parameter, which will be introduced in this section.

2.4.1 Distance

In an expanding universe distances between objects and us cannot be measured directly. One can only observe the light that was emitted at an earlier time when the universe was at a different scale factor than today. Depending on the nature of the observation, several definitions of distance are possible. On very small scales, these definitions coincide but they begin to differ greatly for objects at cosmological distances. A good reference for cosmological distance measure can be found in Hogg (1999; see the references therein for the derivations).

In many publications, distances are given in units of h^{-1} Mpc. This notation originates from a historical parameterization of the Hubble constant as $H_0 = 100\,h\,\mathrm{km\,s^{-1}\,Mpc^{-1}}$, where h is the normalization factor, which is measured to be within a few percent of ~ 0.7. Similarly to the distance, other quantities that depend on the Hubble constant can be stated in units depending on h, e.g. mass estimates based on equation (2.39). This document will use the redshift as the primary quantity to indicate distance but if necessary will assume $h = 0.7$ to convert results of other studies to units independent of h.

Comoving and proper distance The *comoving distance* between two objects remains invariant during the expansion of the universe. It is related to the *proper distance* that one would measure by placing a ruler between those object by a factor of a or $(1 + z)^{-1}$, i.e. while the comoving distance remains the same at all epochs (if structure formation is disregarded), the proper distance increases with the scale factor. Furthermore one must distinguish between radial (or line-of-sight) and transverse distance.

The radial comoving distance d_C can be calculated by integrating over the Hubble expansion since the time of emission at a redshift of z:

$$d_\mathrm{C}(z) = d_\mathrm{H} \int\limits_0^z \frac{\mathrm{d}z'}{E(z')}, \tag{2.40}$$

where $E(z) = H(z)/H_0 = \sqrt{\Omega_\mathrm{r}(1+z)^4 + \Omega_\mathrm{m}(1+z)^3 + \Omega_\mathrm{r}(1+z)^2 + \Omega_\Lambda}$ is the normalized Hubble parameter and $d_\mathrm{H} = c/H_0$ is the Hubble distance.

The transverse comoving distance $d_\mathrm{M}\delta\theta$ measures the distance of two objects at the same redshift but separated by an angle $\delta\theta$. It is also equivalent to the *proper motion distance*, which measures the ratio of an object's actual transverse velocity to its apparent motion on the sky. In a flat universe the transverse comoving distance is equal to its radial counterpart but for a non-zero curvature, the function $\mathcal{F}$ from (2.4) needs to be applied:

$$d_\mathrm{M} = \begin{cases} d_\mathrm{H}\sqrt{\Omega_\mathrm{k}}\sinh\left(\sqrt{\Omega_\mathrm{k}}d_\mathrm{C}/d_\mathrm{H}\right) & \text{for } \Omega_\mathrm{k} > 0 \\ d_\mathrm{C} & \text{for } K = 0 \\ d_\mathrm{H}\sqrt{|\Omega_\mathrm{k}|}\sin\left(\sqrt{|\Omega_\mathrm{k}|}d_\mathrm{C}/d_\mathrm{H}\right) & \text{for } \Omega_\mathrm{k} < 0. \end{cases} \tag{2.41}$$

Angular diameter distance The *angular diameter distance* d_A is defined as the ratio of the physical diameter $2R$ of an object to its apparent angular diameter $\delta\theta$:

$$d_\mathrm{A} = \frac{2R}{\delta\theta}. \tag{2.42}$$

Since it measures the proper size of an object (or the separation between two objects at the same redshift) it is related to the transverse comoving distance by the scale factor:

$$d_\mathrm{A} = \frac{d_\mathrm{M}}{(1+z)}. \tag{2.43}$$

This distance measure is required when observing *standard rulers*, i.e. objects/structures of known size. An example of this are the baryon acoustic oscilations (BAO), periodic fluctuations in the density fluctuations of the matter in the Universe caused by oscillations of the baryon-photon plasma in the early universe.

Luminosity distance The *luminosity distance* d_L is defined by the ratio of the observed flux S of a light source to its intrinsic luminosity L:

$$d_\mathrm{L} = \sqrt{\frac{L}{4\pi S}}. \tag{2.44}$$

In a classical case of a flat and static metric (or on very small scales in FLRW) d_L and d_M would be equal. However, two effects reduce the observed flux in an expanding universe:

- because of time-dilation the time over which the flux is integrated at a telescope corresponds to a shorter time of emission in the rest-frame of the source;

- due to cosmological redshift the energy of each photon is lower than it is was at emission.

As shown in section 2.2.2, both effects depend directly on the scale factor and hence on the redshift; each effect reduces the flux S by a factor $(1 + z)$. Therefore, the luminosity distance can be calculated by:

$$d_\mathrm{L} = (1 + z)d_\mathrm{M} = (1 + z)^2 d_\mathrm{A} \tag{2.45}$$

The luminosity distance is used to compare the flux of *standard candles*, i.e. objects of known luminosity, to their redshift and thereby determine cosmological parameters. Nowadays the term standard candle is most commonly applied to type Ia supernovae (SNe Ia), which are rather "standardizable" because correction for lightcurve width and colour need to be applied (see section 3.1.2). Other objects with a known relation between their luminosity and other properties include Cepheids and galaxies. Both spiral and elliptical galaxies have be used to great extend in studies similar to the one presented in this thesis and are discussed in section 3.1.1.

Distance modulus In astronomy, fluxes are commonly expressed in terms of magnitudes. This logarithmic quantity measures the relative flux in comparison to a reference star with flux f_*. The *apparent magnitude* m of an object is defined as

$$m - m_* = -2.5 \log_{10} \frac{f}{f_*} = -2.5 \log_{10} \frac{L}{L_*} \frac{d_{\mathrm{L}*}^2}{d_\mathrm{L}^2}, \tag{2.46}$$

where L_*, $d_{\mathrm{L}*}$ and m_* are luminosity, luminosity distance and magnitude of the reference star respectively. Historically Vega (α Lyrae) was used as the primary reference start and therefore its magnitude is often set to $m_* = 0$. In order to compare the intrinsic brightness of astronomical objects, the *absolute magnitude* M is defined as the value that its apparent magnitude would have if the object were located at $d_\mathrm{L} = 10\,\mathrm{pc}$:

$$\mu \equiv m - M = 5 \log_{10} \left(\frac{d_\mathrm{L}}{10\,\mathrm{pc}} \right). \tag{2.47}$$

The difference between m and M defines the *distance modulus* μ, which is often used to quantify the distances of standard candles.

Linear Hubble distance and recession velocity Lastly, the distance is occasionally expressed purely based on the linear Hubble law:

$$d = \frac{cz}{H_0}. \tag{2.48}$$

This is often done in studies of velocities and structure in the local universe ($z \lesssim 0.05$), where the linear Hubble law gives a sufficiently accurate value of the proper distance, overestimating it by $\sim 1\%$. Alternatively the recession velocity is used as a distance quantity by some authors; this simply the redshift multiplied by the speed of light, usually rounded to $c = 3 \times 10^8\,\mathrm{m\,s^{-1}}$ to give an easier conversion factor. This quantity is then often still referred to as "distance" despite its unit. Using these definitions, an object at redshift of e.g. $z = 0.05$ may be stated to have a distance of $150\,h^{-1}$ Mpc, 214 Mpc (for $h = 0.7$) or $15\,000\,\mathrm{km\,s^{-1}}$.

2.4.2 Peculiar Velocities

As shown in section 2.3, the peculiar velocity field can be derived from the matter distribution in the universe. Therefore, peculiar velocity measurement of a large number of objects can be used to reconstruct the matter distribution. The transverse proper motion of objects at cosmological distances is not measurable. While one can observe it for Galactic objects (e.g. stars) by tracking their movement on the sky relative to each other, this motion is to small at cosmological distance: at a distance of 100 Mpc ($z \sim 0.023$, within the range of many peculiar velocity studies), a motion of one percent of the speed of light would only amount to an apparent angular velocity of $\sim 6 \times 10^{-6}$ arcseconds per year. The radial component of the peculiar velocity, on the other hand, can be observed as a Doppler shift of the object's spectrum. However, this Doppler shift is indistinguishable from the cosmological redshift and therefore exact knowledge of the cosmological parameters and the distance of the object is required. Furthermore, the dataset must be distributed over a large part of the sky to constrain the whole peculiar velocity field because two of the three peculiar velocity components are unknown for all observed objects.

The radial peculiar velocity can be calculated from an objects *Hubble residual*, i.e. the difference of its measured distance, e.g. μ_{obs}, and the cosmological prediction for the distance to an object at the observed redshift $\mu_{\mathrm{cosmo}}(z_{\mathrm{obs}})$ as the peculiar motion causes a Doppler shift of the emitted light in addition to the cosmological redshift. When disentangling the peculiar redshift z_{pec} from the cosmological component z_H, one may be tempted to simply assume that they can be added linearly as if they were velocities. While this is true for small redshifts, it was pointed out in Harrison (1974) that the correct method of combining redshifts z_i is by calculating the product of $(1 + z_i)$. In the case at hand this means

$$(1 + z_{\mathrm{obs}}) = (1 + z_H)(1 + z_{\mathrm{pec}}) = (1 + z_H)(1 + (\boldsymbol{v}_{\mathrm{e}}/c - \boldsymbol{v}_0/c) \cdot \boldsymbol{n}), \tag{2.49}$$

where $\boldsymbol{v}_{\mathrm{e}}$ and $\boldsymbol{v}_0$ are the peculiar velocities of the emitter and the observer, respectively, and $\boldsymbol{n}$ is the unit vector from the observer to the emitter. There are additional effects of peculiar velocities that depend on how the distance was measured. The first-order effects on the luminosity distance d_{L} were derived in Hui & Greene (2006). The apparent angular diameter $\delta\theta$ is changed due to relativistic boosts, which affect the angular diameter distance according to equation (2.42):

$$\delta\tilde{\theta} = \delta\theta(1 - \boldsymbol{v}_0/c \cdot \boldsymbol{n}) \tag{2.50}$$

$$\Rightarrow \tilde{d}_{\mathrm{A}}(z_{\mathrm{obs}}) = d_{\mathrm{A}}(z_H)(1 + \boldsymbol{v}_0/c \cdot \boldsymbol{n}), \tag{2.51}$$

where a tilde denotes the a quantity that was perturbed for peculiar velocities. Combining equations (2.45) and (2.51), the luminosity distance becomes:

$$\tilde{d}_{\mathrm{L}}(z_{\mathrm{obs}}) = d_{\mathrm{L}}(z_H)(1 + (2\boldsymbol{v}_{\mathrm{e}}/c - \boldsymbol{v}_0/c) \cdot \boldsymbol{n}). \tag{2.52}$$

As the total change of the luminosity distance at the observed redshift is of interest here, one needs to derive the Taylor expansion of d_{L} around z_H:

$$d_{\mathrm{L}}(z_{\mathrm{obs}}) = d_{\mathrm{L}}(z_H)\left(1 + \left[1 + \frac{c(1 + z_H)^2}{H(z_H)d_{\mathrm{L}}(z_H)}\right](\boldsymbol{v}_{\mathrm{e}}/c - \boldsymbol{v}_0/c) \cdot \boldsymbol{n}\right). \tag{2.53}$$

Note that the H and d_{L} in the prefactor can be calculated using either z_H or z_{obs} because the difference is of second order. In combination with equation (2.52) this yields the final expression

$$\tilde{d}_{\mathrm{L}}(z) = d_{\mathrm{L}}(z)\left(1 + \boldsymbol{v}_{\mathrm{e}}/c \cdot \boldsymbol{n} - \frac{(1 + z)^2}{H(z)d_{\mathrm{L}}(z)}(\boldsymbol{v}_{\mathrm{e}} - \boldsymbol{v}_0) \cdot \boldsymbol{n}\right) \tag{2.54}$$

which is accurate to first order and can be used to measure $\boldsymbol{v}_{\mathrm{e}}$ based on measured values of d_{L} and z, since $\boldsymbol{v}_0$ is known accurately from the CMB dipole.

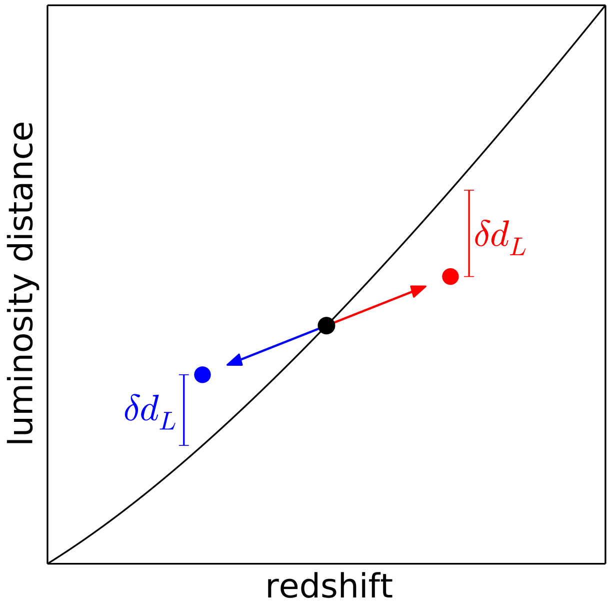

Figure 2.1: Illustration of the effect of peculiar motion on the luminosity distance. The solid line shows the luminosity distance as expected in a homogeneous universe. An object in such a universe would be e.g. at the location of the black circle. If it has a peculiar velocity, both its redshift and it luminosity (and therefore its luminosity distance) will change such that it is shifted to blue or red circles, depending on whether the peculiar motion is towards from the observer or away from him, respectively. The luminosity distance difference used in this analysis is $\delta d_\mathrm{L}(z) = \tilde{d}_\mathrm{L}(z) - d_\mathrm{L}(z)$, see equation (2.54).

In cosmology, redshifts are commonly transformed to the CMB frame, i.e. setting $\boldsymbol{v}_0 \to 0$ and $\boldsymbol{v}_\mathrm{e} \to \boldsymbol{v}_\mathrm{e} + \boldsymbol{v}_0$. This transformation does not affect the second perturbation term in equation (2.54) but the first term is increased by $\boldsymbol{v}_0/c \cdot \boldsymbol{n}$.[5] However, at low redshifts ($z < 0.1$) the first term (0.1% for $v \sim 300\,\mathrm{km\,s^{-1}}$) is negligible compared to the second ($1\% - 10\%$). Therefore, the choice of the frame of reference will not affect peculiar velocity measurements greatly.

---

[5] See Hui & Greene (2006) for explanation of the asymmetry in the formula. More recently, however, Kaiser & Hudson (2015) have shown that the asymmetry disappears if one accounts for the time evolution of the velocity field and for gravitation.

CHAPTER 3

Observational Cosmology

The final two sections of the previous chapter described how distance is defined in an expanding universe and how peculiar velocities affect measurements of distance. This chapters discusses the most commonly used probes of distance and velocities for studies of the local structure and flows. Then the current results of SN Ia cosmology and anisotropy studies are summarized.

3.1 Distance and Velocity Probes

3.1.1 Galaxies

As shown in the previous section, radial peculiar velocities can be estimated for any object with a known independent distance measurement. Galaxies are the most widely used probes of peculiar velocities. Their luminosity distances can be determined using relations between the luminosity of the galaxy and the velocities of the stars in the galaxy.

Tully-Fisher relation The intrinsic luminosity of spiral galaxies is correlated to their rotation velocity (Tully & Fisher, 1977). The latter quantity can be obtained from the width of the emission lines, which are broadened by larger rotation velocities due to Doppler shift. These measurements require additional knowledge of the inclination angle ξ of the galaxy's rotation axis relative to us, estimated by the apparent axial ratio of the galaxy:

$$\cos^2 \xi = \frac{(b/a)^2 - r_0^2}{1 - r_0^2}, \tag{3.1}$$

where a and b are the semi-major and semi-minor axes and $r_0 = 0.2$ is the assumed axial ratio that would be observed if the galaxy were seen completely edge-on (Tully & Fisher, 1977). In the extreme case where the rotation axis is pointing towards us, no broadening of spectral lines due to rotation is observable. The Tully-Fisher relation is then expressed as:

$$L \propto v_{\mathrm{rot}}^b, \tag{3.2}$$

where L is the luminosity and v_{rot} the rotation velocity. The exponent b is determined empirically. The natural explanation of this correlation is that the rotational velocity is related to the mass of the galaxy through the gravitational potential. Thus, studies using near-infrared luminosities (instead of the optical measurements of the original discovery) have found a stronger correlation, because those emissions trace the galaxies stellar mass better. When using estimates of the full baryonic mass (including clouds of gas), an even tighter relation is found (McGaugh et al., 2000). In this form, the relation is also called the *Baryonic Tully-Fisher relation* and is found to have an exponent between 3 and 4 (Gurovich et al., 2010; Stark et al., 2010).

Fundamental Plane For elliptical galaxies, no rotation axis can be defined. Therefore, instead of the rotation velocity, the central velocity dispersion σ_0 is found to correlate with the luminosity of the galaxy; this is called the *Faber-Jackson relation* (Faber & Jackson, 1976). In addition, there is a correlation between the mean surface brightness I_e and the effective radius R_e, i.e. the radius within which half of a galaxy's light is emitted (Djorgovski & Davis, 1987; Dressler et al., 1987). Since the luminosity is a function of surface brightness and effective radius, a relation between the σ_0, R_e and I_e can be found:

$$R_e \propto \sigma_0^\alpha I_e^\beta, \tag{3.3}$$

where the given exponents need to be determined empirically. This relation is know as the *Fundamental Plane*, since it defines a plane in the 3D logarithmic space. Recent measurements found $\alpha = 1.52 \pm 0.03$ and $\beta = -0.89 \pm 0.01$ (Magoulas et al., 2012). Therefore, by measuring σ_0 and I_e, R_e can be estimated. The effective angular radius $R_e^\theta = R_e d_\mathrm{A}(z)$ can then be used to determine the angular diameter distance.

Surface Brightness Fluctuations An independent method for distance determination is the measurement of *surface brightness fluctuations* (Tonry & Schneider, 1988). The method is based on the fact that individual stars can be resolved better in a nearby galaxy than in a distant one. This can be quantified by the Poisson fluctuations in the number of unresolved stars encompassed by a CCD pixel. The mean pixel intensity is $N\bar{f}$ while its variance is $N\bar{f}^2$, where N is the mean number of stars and $\bar{f}$ the mean flux per star. By dividing the variance by the intensity, we then obtain the mean flux $\bar{f}$. If, in addition, the mean luminosity $\bar{L}$ can be measured, we can determine the luminosity distance. For surface brightness fluctuations this can be achieved for old stellar populations (e.g. in elliptical galaxies) because the mean flux is dominated by red giant branch stars. Their absolute I-band magnitude $\bar{M}_I$ can be calibrate but must be corrected linearly for the $(V - I)$ colour index (Blakeslee et al., 1999).

Galaxies have clear advantages as probes of the peculiar velocity field because they provide large statistics in the nearby universe. However, at redshifts $z \gtrsim 0.03$, the required observation of e.g. rotation velocities or the surface brightness fluctuations becomes increasingly inaccurate and expensive. Type Ia supernovae (see next section) offer an alternative to galaxies. While their statistics is currently still lower, they can be observed up to much large distances ($z > 1$) and can be standardized more accurately ($\sigma_d \sim 5 - 8\%$ compared to $15 - 25\%$ for galaxies (Magoulas et al., 2012; Watkins et al., 2009; Johnson et al., 2014)).

3.1.2 Type Ia Supernovae

Much like galaxies, type Ia supernovae (SNe Ia) can be used to determine distances. The maximum absolute magnitudes of SNe Ia have a scatter of $\sigma \sim 0.4$ mag, which corresponds to a scatter of $\sim 20\%$ in distance and is already comparable to the precision of galaxy distances. However, SNe Ia can be standardized even further using two correlations:

- **brighter-wider:** a.k.a. the Phillips relation (Phillips, 1993), the slower the lightcurve declines, the brighter the SN is at the peak of its lightcurve (see figure 3.1),

- **brighter-bluer:** the smaller the SN's $B - V$ colour index, i.e. the difference of its magnitude in B- and V-band, is at peak, the brighter it is.

To correct for these correlations, a full lightcurve must be observed in multiple filter bands. These observations can then be standardized using various methods referred to as *lightcurve fitters*, notably MLCS (Riess et al., 1996), MLCS2k2 (Jha et al., 2007), SALT (Guy et al., 2005) and SALT2 (Guy et al., 2007).

Supernova classification is based on historical observations of their spectra, not on the physical mechanism behind their explosions. Type I supernova have no hydrogen lines while those of type II do. SNe Ia are further distinguished by a strong ionized silicon line at 615 nm near peak brightness. The interpretation of the homogeneity of SN Ia magnitudes is that they are caused by a thermonuclear explosion of a carbon-oxygen white dwarf (C-O WD) which accreted sufficient matter from a companion star to reach the Chandrasekhar mass limit M_{Ch}, above which the electron degeneracy pressure fails to balance the white dwarf's own gravitational self-attraction (Chandrasekhar, 1931). This mass limit can be calculated from fundamental physical constants:

$$M_{\mathrm{Ch}} = \frac{\omega_3^0 \sqrt{3\pi}}{2} \left(\frac{\hbar c}{G}\right)^{3/2} \frac{1}{(\mu_e m_H)^2} \sim 1.4 M_\odot \tag{3.4}$$

where μ_e is the molecular weight per electron (which depends on the chemical composition of the white dwarf), m_H is the mass of a hydrogen atom and $\omega_3^0 \approx 2.018236$ is a constant from the solution of the Lane-Emden equation for the gravitational potential of a self-gravitating fluid (Chandrasekhar, 1931, 1935).

Possible progenitor systems for an SN Ia are a C-O WD accreting matter from a companion star (e.g. a red giant) or a system of two C-O WDs (double-degenerate system) which merge. When the C-O WD approaches the Chandrasekhar limit, thermonuclear fusion of the carbon begins near the centre of the white dwarf and creates a deflagration front which burns at sub-sonic speed initially. This fusion flame transitions to a supersonic detonation near the white dwarf's surface. (Hillebrandt & Niemeyer, 2000)

The correlation of peak magnitude and lightcurve decline rate was first observed by Phillips (1993) using the difference Δm_{15} between maximum B-band magnitude and the magnitude 15 rest frame days after the maximum. The absolute magnitude is then parameterized as $M_{\mathrm{max}} = a + b\Delta m_{15}$ and fit to Hubble's law. Using this correction, the scatter can be reduced to $\sigma \sim 0.15$ (Hamuy et al., 1996a). Other parameterizations have been used to express the shape-luminosity correlation: one possibility is a stretch parameter s (e.g. used by SALT) which stretches the rest-frame time such that the lightcurve decline rate matches a fiducial template. SALT2 parameterizes the shape with a generic parameter x_1 that is derived by training a lightcurve model. This parameter describes an effect similar to stretch even though no prior information on lightcurve shape was used in training the template. In all cases a linear correction is made to the peak magnitude and the coefficient of this correction is determined along with the cosmological parameters when the Hubble law is fit to the data. Simulations (e.g. Woosley et al. 2007; Kasen et al. 2009; Sim et al. 2013) have shown that this correlation is likely due to the amount of ^{56}Ni that is produced in the explosion as the decay of this radioactive nickel isotope powers the subsequent lightcurve. The amount of ^{56}Ni produced depends on the initial conditions. As it is produced in the explosion and not by carbon fusion, a weak or asymmetrical ignition of the carbon burning may lead to a larger production of ^{56}Ni (Kasen et al., 2009).

The colour-luminosity correlation is in part expected because extinction by dust is wavelength dependent, absorbing more light for shorter wavelengths (Cardelli et al., 1989). This means that a source will appear redder if the absorption along the way is stronger. This effect is usually quantified by the absorption in a given passband (e.g. $A_V = R_V \cdot E(B-V)$) or the colour parameter $c = (B-V)_{\mathrm{max}} - \langle B-V \rangle$ that

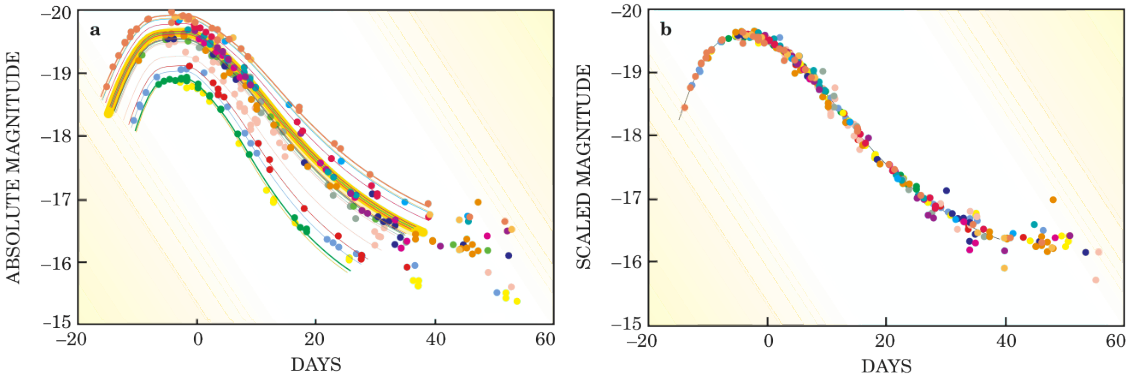

Figure 3.1: Lightcurves of nearby, low-redshift type Ia supernovae Hamuy et al. (1996c). Left: without correction. Right: stretch corrected and normalized to peak magnitude, showing the similarity of SN Ia lightcurves. (Figures from Perlmutter 2003)

expresses the colour excess. The physical interpretation of this correlation differs between lightcurve fit methods. While the colour is attributed to extinction and hence limited to positive colour parameter when using MLCS2k2, SALT2 interprets it as a general colour excess that need not be solely due to extinction and hence can be negative. When one corrects the peak magnitude similarly to the stretch correction, the resulting coefficient does not match the extinction ratio of the Milky Way $R_V = 3.1$ but one rather finds values around $R_V \sim 2$ (Tripp, 1998; Hicken et al., 2009b). This indicates that the brighter-bluer relation is indeed partly due to some intrinsic effect. Recent SN simulations (Kasen et al., 2009) with various ignition conditions, deflagration to detonation transitions and viewing angles exhibit such an intrinsic colour variation. The models show a range of $B - V$ colours at maximum which is not fully correlated with the decline rate. In addition a study of the spectra of 76 SNe Ia near their peak brightness (Chotard et al., 2011) found an extinction ratio $R_V = 2.8 \pm 0.3$ after correcting for signatures correlated with the equivalent widths of spectral features due to silicon and calcium. This further suggests that the colour variations of SNe Ia are partly intrinsic.

Other methods for SN Ia standardization exist. Instead of using a full photometric lightcurve, a single spectrum at maximum light can be standardized to a similar level by correcting for the ratio of the fluxes at 642 nm and 443 nm (Bailey et al., 2009).

3.1.3 Kinematic Sunyaev-Zeldovich Effect

The *Sunyaev-Zeldovich effect* (SZ effect, Zeldovich & Sunyaev 1969) is a distortion in the CMB spectrum on small angular scales. It occurs when CMB photons pass through the hot intracluster plasma in galaxy clusters and scatter on the high-energy electrons therein. While the effect is mostly driven by the temperature (thermal SZ or tSZ effect) and density of the intracluster medium, there is a second order kinematic component of the distortion (kinematic SZ or kSZ effect). By themselves, measurements of this effect can only provide very weak constraints on the peculiar velocities of the clusters because the kinematic component cannot be fully distinguished from its thermal counterpart. However, as proposed by Kashlinsky & Atrio-Barandela (2000), a large dataset of clusters can be used to constrain large-scale bulk flows. This is possible because the thermal component is uncorrelated between the clusters and therefore it is expected to average out for large samples. On the other hand, the kinematic component can be correlated by a large-scale peculiar motion and therefore detectable as a dipole. Unlike SNe and galaxies, which measure peculiar velocities as a deviation from the Hubble expansion rate that decreases in relative amplitude with redshift, the kSZ effect directly measures the velocity relative to the CMB. This allows peculiar velocity detection at distances where galaxies are difficult to standardize and velocities from SNe Ia, while still measurable, become increasingly noisy. However, the method for detecting a dipole proposed by Kashlinsky & Atrio-Barandela (2000) requires filtering out the primary CMB component without the removing the kSZ signal as well as isolating the tSZ contribution to the dipole (Atrio-Barandela et al., 2015). Due to different approaches to this filtering, markedly different results have been published based on the same data, see section 3.2.3.

3.2 Current Results

3.2.1 SN Ia Cosmology

Since the discovery that the expansion of the universe is accelerating at present time (Riess et al., 1998; Perlmutter et al., 1999), observations of SNe Ia have been established as a key method to constrain the energy content of the universe. While many theoretical models exist that could explain the acceleration, the most straight-forward one is the ΛCDM model, a FLRW model where the acceleration is caused by a cosmological constant expressed as the density parameter Ω_Λ. More generally the source of the acceleration is often parameterized as a dark energy with an equation of state parameter $w < -1/3$, which adds a positive term to the second Friedmann equation (2.14), see section 2.2.4. This model is then often dubbed wCDM to distinguish it from a cosmological constant model, which would correspond to $w = -1$, i.e. it does not dilute when the universe expands. Furthermore, an evolving equation of state may be of interest to distinguish models for dark energy. This evolution is often parameterized as a linear slope:

$$w(z) = w_0 + w_a\left(1 - \frac{1}{1+z}\right). \tag{3.5}$$

The largest datasets of SNe Ia that were compiled in the recent years are the Union compilations (Kowalski et al. 2008; Amanullah et al. 2010; Suzuki et al. 2012, see also section 4.4.2) and the joint light-curve analysis (JLA) sample (Betoule et al., 2014). The latter is the largest analysis of SN Ia data to date, using a total of 740 SNe from SDSS-II (Frieman et al., 2008) and the (Astier et al., 2006), several low-redshift samples, and a few high-redshift HST SNe. The best constraints can be derived from these data when using priors from the Planck CMB results and measurements of baryon acoustic oscilations (BAO).

The Hubble diagram for the JLA sample is shown in the left panel of figure 3.2. When only determining the density contribution to the universe, they find a matter density of $\Omega_\mathrm{m} = 0.305 \pm 0.010$ and curvature consistent with zero ($\Omega_\mathrm{k} = 0.03 \pm 0.02$), meaning almost 70% of the energy in the universe are made up by dark energy. For a flat w-CDM model, in which the dark energy equation of state parameter is varied, they find the acceleration to be consistent with a cosmological constant ($w = -1.027 \pm 0.055, \Omega_\mathrm{m} = 0.303 \pm 0.012$). Finally, models of a redshift-dependent equation of state find no significant evolution ($w_0 = -0.957 \pm 0.124, w_a = -0.336 \pm 0.552$. Currently these are the most stringent constraints on the nature of dark energy.

3.2.2 CMB Dipole and Local Group Motion

The dipole anisotropy of the CMB ($\Delta T/T \sim 10^{-3}$) is two orders of magnitude larger than the higher multipole orders. It is therefore unlikely to be fully intrinsic but is instead assumed to be caused by Doppler shift due to the motion of the solar system at $369.5 \pm 3.0\,\mathrm{km\,s^{-1}}$ towards the Galactic coordinates

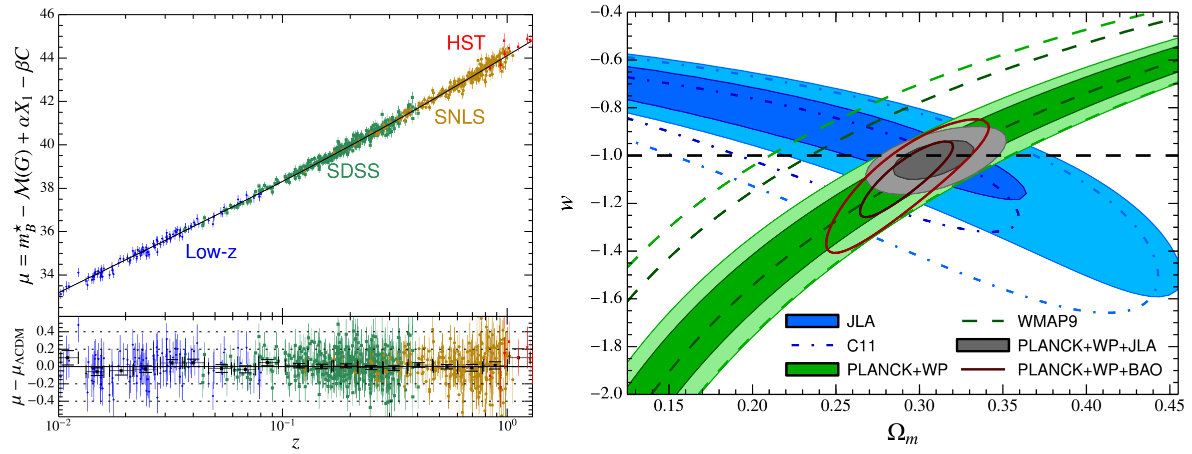

Figure 3.2: *Left:* Hubble diagram of the JLA sample. The bottom panel shows the distance modulus residuals from the best-fit ΛCDM cosmology; *Right:* Confidence contours for Ω_m and w at 68% and 95% including systematic uncertainties. (Figures from Betoule et al. (2014), also available at `http://supernovae.in2p3.fr/sdss_snls_jla/ReadMe.html`)

($l = 264.4° \pm 0.3°, b = 48.4° \pm 0.5°$; Kogut et al. 1993). When combining this result with the motion of the solar system within our galaxy and that of our galaxy in its Local Group (LG), one finds a velocity of the LG of $627 \pm 22\,\mathrm{km\,s^{-1}}$ towards ($l = 276° \pm 3°, b = 30° \pm 3°$)[1]. As seen in equation (2.39), this motion can be explained by the attraction of mass concentrations near the LG. This has been studied extensively using distance estimates to nearby galaxies. Lynden-Bell et al. (1988) analysed the dynamics of 400 elliptical galaxies, finding that their velocities appear to converge at a Great Attractor (GA) at $z \sim 0.015$ in the direction ($l = 307°, b = 9°$). The nearest overdensity is the Virgo cluster, which has been shown to generate an infall velocity of $240 \pm 40\,\mathrm{km\,s^{-1}}$ by Jerjen & Tammann (1993), contributing about a quarter of the LG motion[2]. Further studies of this region mapped several rich galaxy clusters, e.g. the Norma cluster (Kraan-Korteweg et al., 1996) and CIZA J1324.7-5736 (Ebeling et al., 2002) near the Hydra-Centaurus region, but these are also not massive enough to explain the full motion. Based on an all-sky sample of X-ray clusters, Kocevski & Ebeling (2006) concluded that the attractors in the GA region account for 44% of the LG motion while the remainder must be caused by a large-scale flow caused by attractors at redshifts between $0.04 < z < 0.06$. As a major contributor at these distances they cite the Shapley supercluster (SSC, Shapley 1930; Scaramella et al. 1989; Raychaudhury et al. 1991), which extends to redshifts $0.035 < z < 0.055$ with its centre at a redshift of $z \sim 0.046$ close to the direction of the LG motion at ($l = 306.44°, b = 29.71°$). However, they also note other clusters and filaments that are located further from the dipole direction and contribute to this large-scale motion, e.g. the Horologium-Reticulum supercluster. In addition to attraction by overdensities, equation (2.39) also shows that underdense regions (voids), will cause peculiar velocities away from them. For instance, Tully et al. (2008) showed that the motion of the LG contains a component of $259\,\mathrm{km\,s^{-1}}$ towards ($l = 209.7°, b = -2.6°$), which originates from the outflow out of the Local Void.

---

[1] After this section, this document will refer to this direction as the “direction of the CMB dipole”. Even though technically incorrect, this simplification of the terms is justified since the dynamics within the LG occur on scales much smaller than those studied here.

[2] The Virgo cluster is not located exactly in the direction of the LG motion but at an angular separation of ~45°. Therefore, not the whole infall velocity amplitude is contributed to the LG motion.

3.2.3 Bulk Flow

Since the LG motion was found to be caused in part by a large-scale flow, it is interesting to constrain this *bulk flow* and put it in context with expectations from structure formation. Peculiar velocities that are caused by random fluctuations of the density in the universe are expect to average out over large volumes. However, in sufficiently small volumes, velocities of several hundred $\mathrm{km\,s^{-1}}$ are expected. Based on the peculiar velocity power spectrum – the ΛCDM expectation for the correlation between peculiar velocities of two objects as a function of their separation – the velocity dispersion v_{rms} of a sphere up to a distance d or a redshift z can be predicted as (Kashlinsky et al., 2010, 2012)

$$v_{\mathrm{rms}} \simeq 250 \left(\frac{100\,h^{-1}\,\mathrm{Mpc}}{d} \right) \mathrm{km\,s^{-1}} \tag{3.6}$$

$$\simeq 80 \left(\frac{0.1}{z} \right) \mathrm{km\,s^{-1}}, \tag{3.7}$$

where the conversion to redshift used the linear Hubble law and the relation was derived for redshifts $z > 0.03$. Therefore, the bulk flow is expected to decrease with distance and significantly larger velocities would potentially challenge our understanding of structure formation. For example, the velocity averaged over a sphere that extends to the centre of the SSC is expected to be $\lesssim 180\,\mathrm{km\,s^{-1}}$. The bulk flow up to such distances has been studied in multiple analyses using galaxies and (more recently) SNe Ia. Examples of these studies are listed in table 3.1. The table is split into a low-redshift and a high-redshift part, which probe at redshifts below and above $z \sim 0.05$, respectively. In this case, low-redshift studies are not necessarily restricted to having data at redshifts $z < 0.05$, but the main weight of the data is at such a redshift while there can be sparser data at higher redshifts. Similarly, the high-redshift studies may contain data at $z < 0.05$, but the low redshift range is usually sparsely covered. This is particularly true for the kSZ studies, which have little nearby data.

The low-redshift studies show a possible tension between the bulk flow results. One set of results shows a possibly anomalous amplitudes (e.g. Hudson et al. 2004; Lavaux et al. 2010; Feldman et al. 2010), while the other (Courteau et al., 2000; Nusser & Davis, 2011; Nusser et al., 2011; Dai et al., 2011) found lower values that are compatible with the ΛCDM prediction. These two sets of results are not clearly divided by the type of data used but rather by details of the analysis method; in fact, some of the listed analyses use the same data. Lavaux et al. (2010), for instance, found a large velocity of $473 \pm 128\,\mathrm{km\,s^{-1}}$ in the Two Micron All-Sky Redshift Survey (2MRS) catalogue using an orbit-reconstruction algorithm that finds a unique displacement field of the galaxy redshifts, which can be interpreted as peculiar velocities. Similar values were found by Watkins et al. (2009) and Feldman et al. (2010) using distance indicators of galaxies and SNe Ia on a dataset containing the 2MRS catalogue. Nusser et al. (2011), on the other hand, analysed the same data using a method based on the systematic variations of the galaxy luminosities, and found a bulk flow consistent with ΛCDM. The authors point towards uncertainties in the standardization methods for galaxies, especially the luminosity function that relates the observed luminosity to the actual mass, as a possible reason for the overestimated bulk flow. SNe Ia may help to mitigate this tension in the future since they provide better constraints on the distance and their biases have been studied extensively.

3.2.4 Dark Flow

On larger scales, analyses using the kinematic Sunyaev-Zeldovich (kSZ) effect on WMAP data have reported even larger bulk flows of the order of $\sim 1000\,\mathrm{km\,s^{-1}}$, extending well beyond redshifts $z = 0.1$ (Kashlinsky et al. 2008, 2009, 2010, see the lower block of table 3.1). A bulk flow of that amplitude

Reference	Object type	Redshift range	l [°]	b [°]	v [km s^{-1}]
Low redshift					
Courteau et al. (2000)	galaxies	$0.015 < z < 0.023$	–	–	70^{+100}_{-70}
Hudson et al. (2004)	galaxies	$z < 0.04$	273	6	372 ± 127
Haugbølle et al. (2007)	SNe Ia	$z < 0.021$	281^{+21}_{-24}	14^{+16}_{15}	239^{70}_{-96}
Lavaux et al. (2010)	galaxies	$z < 0.033$	220	25	473 ± 128
Feldman et al. (2010)	galaxies & SNe Ia	$z < 0.033$	282 ± 11	6 ± 6	416 ± 78
Nusser & Davis (2011)	galaxies	$z < 0.033$	279	10	257 ± 44
Colin et al. (2011)	SNe Ia	$0.015 < z < 0.06$	287^{+62}_{-48}	21^{+34}_{-52}	250^{+190}_{-160}
Dai et al. (2011)	SNe Ia	$z < 0.05$	290^{+39}_{-31}	20 ± 32	188^{+119}_{-103}
Macaulay et al. (2012)	galaxies & SNe Ia	$z < 0.033$	295 ± 18	14 ± 18	380^{+99}_{-132}
Turnbull et al. (2012)	SNe Ia	$z < 0.05$	319 ± 18	7 ± 14	249 ± 76
Lavaux et al. (2013)	kSZ (galaxies)*	$z < 0.05$	324 ± 27	-7 ± 17	533 ± 263
Ma & Pan (2014)	galaxies & SNe Ia	$z < 0.03$	281 ± 7	8^{+6}_{-5}	290 ± 30
Watkins & Feldman (2015)	galaxies	$z < 0.1$	290	12	262 ± 60
High redshift					
Kashlinsky et al. (2010)	kSZ	$z < 0.12$	282 ± 34	22 ± 20	934 ± 352
	kSZ	$z < 0.25$	296 ± 29	39 ± 15	1005 ± 267
Dai et al. (2011)	SNe Ia	$z > 0.05$	–	–	–
Lavaux et al. (2013)	kSZ (galaxies)*	$z < 0.17$	–	–	<470**
Planck Collaboration Int. XIII (2014)	kSZ	$z < 0.5$	–	–	<254**
Hernández-Monteagudo et al. (2015)	kSZ	$z < 0.12$	–	–	<290**

Table 3.1: Bulk flow velocities obtained from previous studies. The upper block shows results that have mostly nearby data (though the may extend to $z = 0.1$), while the lower block shows those that probe higher redshifts. These studies may still have data at low redshift but their main weight lies at $z > 0.1$. If values are not stated, they were either not given by the authors or they only reported a non-detection.

*Instead of galaxy clusters, Lavaux et al. (2013) used the kSZ effect in galaxies themselves. **The results of Lavaux et al. (2013), Planck Collaboration Int. XIII (2014), and Hernández-Monteagudo et al. (2015) are 95% upper limits.

would be far beyond any prediction from ΛCDM structure formation. Its existence could point towards extensions of our cosmological standard model, e.g. a tilt imprinted on our horizon by pre-inflationary structure (Grishchuk & Zeldovich, 1978; Turner, 1991). This tilt would then be observable as a bulk flow extended throughout the whole observable universe. Given its inconsistency with ΛCDM and in allusion to the terms dark matter and dark energy this large-scale bulk flow has also been referred to as "dark flow". Other analyses of the kSZ signal using WMAP (Keisler, 2009; Osborne et al., 2011; Mody & Hajian, 2012; Lavaux et al., 2013) and Planck Planck Collaboration Int. XIII (2014); Hernández-Monteagudo et al. (2015), have failed to reproduce the dark flow and reject bulk flows larger than $250\,\mathrm{km\,s^{-1}}$ at the 95% confidence level. However, the authors of the dark flow detection papers have pointed out differences in analysis methods, e.g. the filter used to remove the tSZ component of the effect, in these publications. The earlier studies, especially Keisler (2009), have been shown to overestimate the uncertainties based on misconceptions of the method (Atrio-Barandela et al., 2010). Atrio-Barandela (2013) further points out that spherically symmetric filters of the CMB map can remove the bulk flow signal if it exists but cannot imprint it if it does not exist. Furthermore, it has been pointed out that the results based on Planck data (Planck Collaboration Int. XIII, 2014) in fact show the dark flow but use random sampling methods that overestimate the uncertainties. Atrio-Barandela et al. (2015) reanalysed the WMAP and Planck data, finding the reported dark flow in both.

Given the great differences in the reported results, it is important to test the claim of a dark flow with independent methods. Galaxy surveys generally do not have the required precision and depth to constrain the bulk flow at those distances. SNe Ia may offer a good alternative but still lack isotropically distributed data at the redshift in question. Previous studies (e.g. Dai et al. 2011) probe large distances but usually lead to large uncertainties because most data is at too large distances, where the individual peculiar velocity cannot be well constrained, and the data is clustered in comparably small fields of the sky, which can bias the bulk flow estimates.

3.2.5 General Anisotropy

Instead of directly measuring peculiar velocities as described in the previous sections, the cosmological principle can be tested in more generalized ways. Within the ΛCDM model, these analyses are expected to detect anisotropy only up to redshift of $z \sim 0.1$, where the bulk flow is expected to be lower $\lesssim 100\,\mathrm{km\,s^{-1}}$, and see a convergence to isotropy at higher redshifts.

As an example, Colin et al. (2011) used a statistic based weighting the Hubble residuals of SNe Ia of the Union2 compilation based on their location. This method of smoothed residuals detects region where the SNe are brighter/fainter on average and will be used in this thesis as well, see section 5.2. At low redshifts, they detected a dipole anisotropy that matches the direction and significance of the observed bulk flow, while the results were consistent with isotropy. At redshifts immediately behind the SSC they found a reversal of the dipole direction, which could be caused by a backside infall into the SSC. However, this particular result can be shown to be originate from SNe on the other side of the sky, which are not correlated with the SSC, see the results in chapter 6 of this document, some of which were published in Feindt et al. (2013). Using a larger dataset than Colin et al. (2011), Appleby et al. (2015) draw similar conclusions.

Another test of the isotropy consists in looking for directional variations of the Hubble expansion. Schwarz & Weinhorst (2007) found a significant (95% confidence level) difference in the expansion rate on opposite hemispheres based SN Ia data up to $z < 0.2$. However, the direction of the detected anisotropy was close to the equatorial poles, indicating a possible systematic differences between surveys of the northern and southern sky as a possible explanation. Kalus et al. (2013) repeated this analysis for a larger dataset and confirmed the result of Schwarz & Weinhorst (2007) for multiple methods of SN Ia standardization. They found that the amplitude does not contradict the ΛCDM expectations and that the direction of the anisotropy is compatible with local structure such as the SSC.

More general anisotropy studies have furthermore put into question the interpretation of the CMB dipole as a motion of the LG. Wiltshire et al. (2013) analysed the angular variance of the Hubble expansion of 4534 galaxy distances and found that the mean of the Hubble parameter of consecutive redshift shells is more compatible with its global value when using the LG rather than the CMB as rest frame. They suggest that the CMB dipole cannot be simply explained by the standard kinematic interpretation but that in part the Hubble expansion is anisotropic due to the non-linear structure. Similarly, studies of the cosmic radio dipole (Rubart & Schwarz, 2013) found it to be inconsistent with the assumption of a purely kinematic origin.

CHAPTER 4

Data

The analyses presented in this document are based on SN Ia data from the Nearby Supernova Factory (SNFACTORY, Aldering et al. 2002) and the Union2 compilation of SNe Ia (Amanullah et al., 2010). First the anisotropy of each dataset is determined separately, but eventually they will be combined for a full analysis of the available data. In section 4.1, the SNFACTORY project is described, while section 4.2 explains surveys looking for nearby SNe based on the example of the La Silla/QUEST (LSQ) supernova search. Section 4.3 will discuss the fitting method the lightcurves to standardize SNe Ia (see section 3.1.2). Finally the full dataset used in this study is described in section 4.4.

4.1 The Nearby Supernova Factory

The SNFACTORY (Aldering et al., 2002) is an international collaboration with the objective to study a large sample of SNe Ia in the Hubble flow ($0.03 < z < 0.08$), in order to improve them as standard candles for cosmology. The project started in 2000 as a collaboration of researchers at facilities in France (LPNHE, Paris; CRAL and IPNL, Lyon) and the United States (LBNL, Berkeley; Yale). The project entered its second phase in 2010 and was expanded to China (Tsinghua university, Beijing) and Germany (Max-Planck-Institut für Astrophysik, Garching; Universität Bonn[1]).

To improve SNe Ia as standard candles, the SNFACTORY takes spectrophotometric time series of a large number of low-redshift SNe Ia. This differs from typical SN surveys, which only use one or two spectroscopic exposures to classify the SN but subsequently follow it with photometric observations to obtain lightcurves for standardization. The SNFACTORY dataset, on the other hand, is made up of absolutely flux-calibrated spectral observations. This technique makes the measurement harder by increasing the amount of information recorded by more than two orders of magnitude (~ 2000 wavelength bins vs. 5 filter bands), and hence decreases the quality of each individual measurement accordingly. On the other hand, it has the significant advantage of obtaining a full spectral time series of the SN, and thus all the relevant information to investigate the explosion mechanism (spectral lines of specific elements). Similarly, lightcurves can this way be generated in any filter system using synthetic photometry. Figure 4.1 shows an example of such a synthetic lightcurve. Therefore, the high-quality data taken by SNFACTORY can be used to reduce the uncertainties of cosmological parameters by better constraining the zero point of the Hubble diagram, which is required in addition to high-redshift observations (see chapter 2).

---

[1] In 2014, this group moved to the Humboldt-Universität zu Berlin.

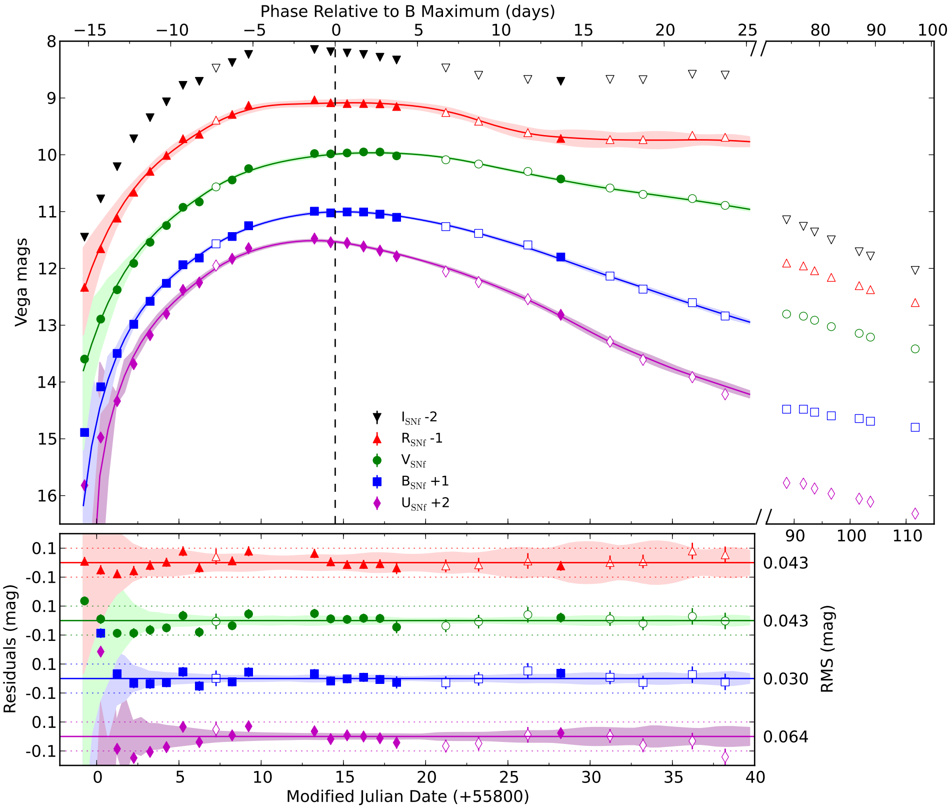

Figure 4.1: Top panel: synthetic lightcurves of SN 2011fe (spectrophotometric time series in figure 4.3) using the SNFACTORY *UBVRI* filter set (non-overlapping top-hat filters, see Bailey et al. 2009). The results of a SALT2 lightcurve fit (see section 4.3) of *UBVR* in the phase range $-16 < t < +25$ days are shown as solid lines. The shaded areas represent the SALT2 model error. Bottom Panel: corresponding residuals (SALT2 − SNIFS). (Figure from Pereira et al. 2013)

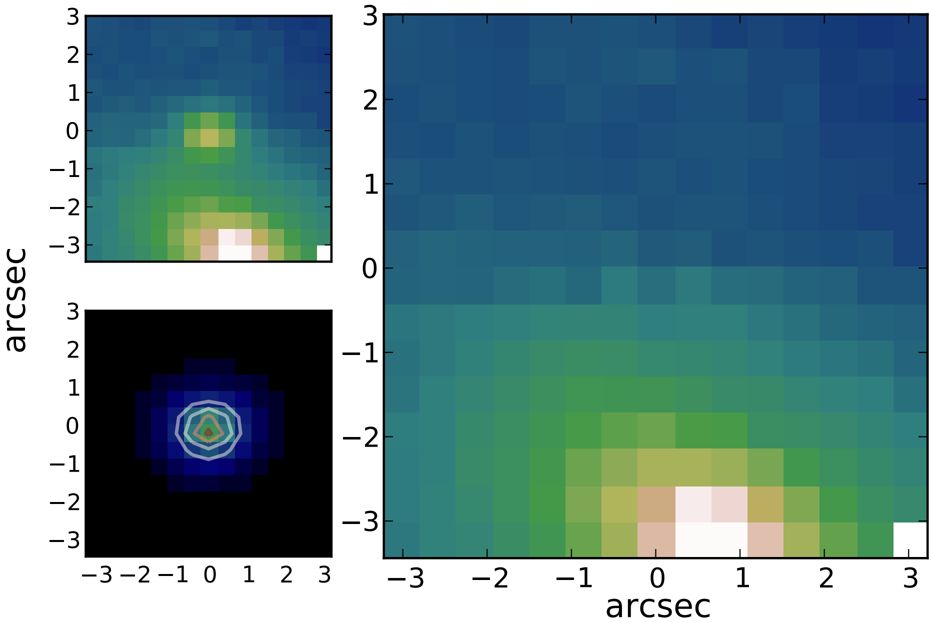

Figure 4.2: Example for the SN subtraction from a host cube used by the SNFACTORY. Different reconstructed images, made by integrating cubes with two angular dimensions and one in wavelength along the wavelength axis, are shown for a single observation of SNF20070326-012. Top left panel: original flux-calibrated cube containing host, sky, and SN signals. Bottom left panel: pure SN cube obtained after host subtraction (image) and fitted PSF model (contours). Right panel: SN-subtracted host cube. (Figure from Rigault et al. 2013)

The choice of distances at which to observe SNe for this depends on two factors: firstly the SNe need to be at distance where the effect of peculiar velocities of the measurements has become small ($z > 0.03$) and secondly the observation of high-quality spectra must not require an excessive amount of telescope time ($z < 0.08$). Additionally, the spectral time series can be used to find better means of standardizing SNe Ia or compared to numerical simulations of SN explosion, thereby helping us understand the nature of SN Ia explosions.

The SNFACTORY observations are performed by a custom-built two-channel *SuperNova Integral Field Spectrograph* (SNIFS, Lantz et al. 2004) mounted on the University of Hawaii 2.2 m telescope at Mauna Kea. SNIFS is an integral field unit (IFU) that obtains 3D data, called *cubes*, which are composed of data at sky positions x, y and wavelengths λ. Each cube thus contains the full information of the SN signal, host galaxy and sky, allowing a better measurement of the spectra than by slit-spectroscopy, for which the fraction of light entering the instrument depends on the wavelength and accuracy of centring the slit on the SN. SNIFS has a field of view of $6.4'' \times 6.4''$ and two spectroscopic channels: a blue channel from 3200 – 5400 Å and a red channel and 5200 – 10 000 Å, covering 3200 – 10 000 Å in combination. In each channel the light is divided a 15×15 microlens array, giving 225 spectra in total. The SN signal is extracted from the data cube using point spread function fitting techniques, as well as host galaxy subtraction (Bongard et al., 2011). To extract the SNe from structured background (host galaxies), the collaboration developed an original extraction technique, composed by two individual steps. First, based on pure host observations taken months after the SN faded away, DDT (Bongard et al., 2011) creates a model of the host galaxy, upon which the point spread function (PSF) can be adjusted to match the exact observation of the host during SN observation. Based on this model, Copin (2013) constructed a PSF model that will extract the SN as a point source using the background from DDT. Such an extraction is illustrated in figure 4.2, where we see that the PSF modelling accurately remove the SN from the SN+galaxy cube. This way, we are confident that the SN data are free from host contamination. The calibration procedures, which fits for nightly atmospheric extinction and instrumental response, are detailed in Buton et al. (2013) and Pereira (2008). Descriptions of SNFACTORY, SNIFS and its operation can be found in Aldering et al. (2002) while more information on the data processing is presented in Aldering et al. (2006) and updated in Scalzo et al. (2010). Figure 4.3 shows the spectral time series of SN 2011fe (Pereira et al., 2013) as an example of the final data produced by the SNFACTORY pipeline.

Until the end of 2008, the targets for SNFACTORY observations were mainly provided by a search using the QUEST-II camera (Rabinowitz et al., 2003; Baltay et al., 2007), which at that time was mounted at Mount Palomar. Later it was moved to La Silla where it resumed the SN search in 2012 (see the next section). In the meantime, targets from other searches such as PTF (Palomar Transient Factory, Law et al. 2009) were used. Since 2004 SNFACTORY followed ~ 300 SNe Ia, observed 617 SNe Ia at least once and classified more than 1500 objects spectroscopically most of them supernovae (see figure 4.4). In general, the first observation of an object is used to determine its type but in some cases the classifications have already been published in an Atel (Astronomer's Telegram).

4.2 Supernova Search

Supernova search strategies differ depending on the target redshift range. High-redshift surveys such as SDSS (Holtzman et al., 2008) or SNLS (Astier et al., 2006) only need to observe comparably small patches of the sky (2 square degrees in case of SNLS) regularly to obtain several hundred lightcurves. Surveys at low redshifts, on the other hand, cannot discover many SNe this way because the observed volume is too small. Instead the survey must either use a wide-field telescope to observe a large part of the sky or must target galaxies from a pre-determined catalogue to increase the number of found transients. The latter approach has the drawback that it is potentially biased towards SNe in more massive galaxies, which are chosen since they show more stars per pointing, improving the probability of finding SNe.

For studies of anisotropies and peculiar velocities, the optimal search strategy needs to cover the whole sky to allow significant constraints on the large-scale correlation of observations. Due to this and the fact that peculiar velocities can be constrained better the closer a SN is to us, an untargeted low-redshift survey is the most promising in this field of research.

La Silla/QUEST An example for such a survey is the La Silla/QUEST (LSQ) Low Redshift Supernova Survey (Baltay et al., 2013) that (among others) provides data for SNFACTORY. The survey is part of the LSQ Southern Hemisphere Variability Survey (Hadjiyska et al., 2012) using the large area QUEST camera mounted at the ESO 1 m Schmidt telescope in La Silla, Chile. This broader survey includes surveys of Kuiper Belt Objects (Rabinowitz et al., 2012), RR Lyrae variable stars (Vivas et al., 2008), tidal disruption events, quasar variability and other transients (Rabinowitz et al., 2011; Hadjiyska et al., 2013). From 2009 to 2011, the search focused on finding Kuiper Belt Objects and RR Lyraes. These searches provided the reference images of the survey fields that are required for the supernova search, which commenced in late 2011 and is expected to run until 2016. Schmidt telescopes (Schmidt, 1938) are generally used for wide field surveys because they have a large field of view with limited aberrations. The QUEST camera consists of 112 CCDs that capture a 8.7 square degree field and uses to broad band $g + r$ filter that covers roughly 4000 – 7000 Å. The telescope is completely robotic but a schedule needs to be provided for each night. The schedule is determined such that observed field are no closer than 15° to the Moon and such that SNe found in these fields can be followed for about another two months to

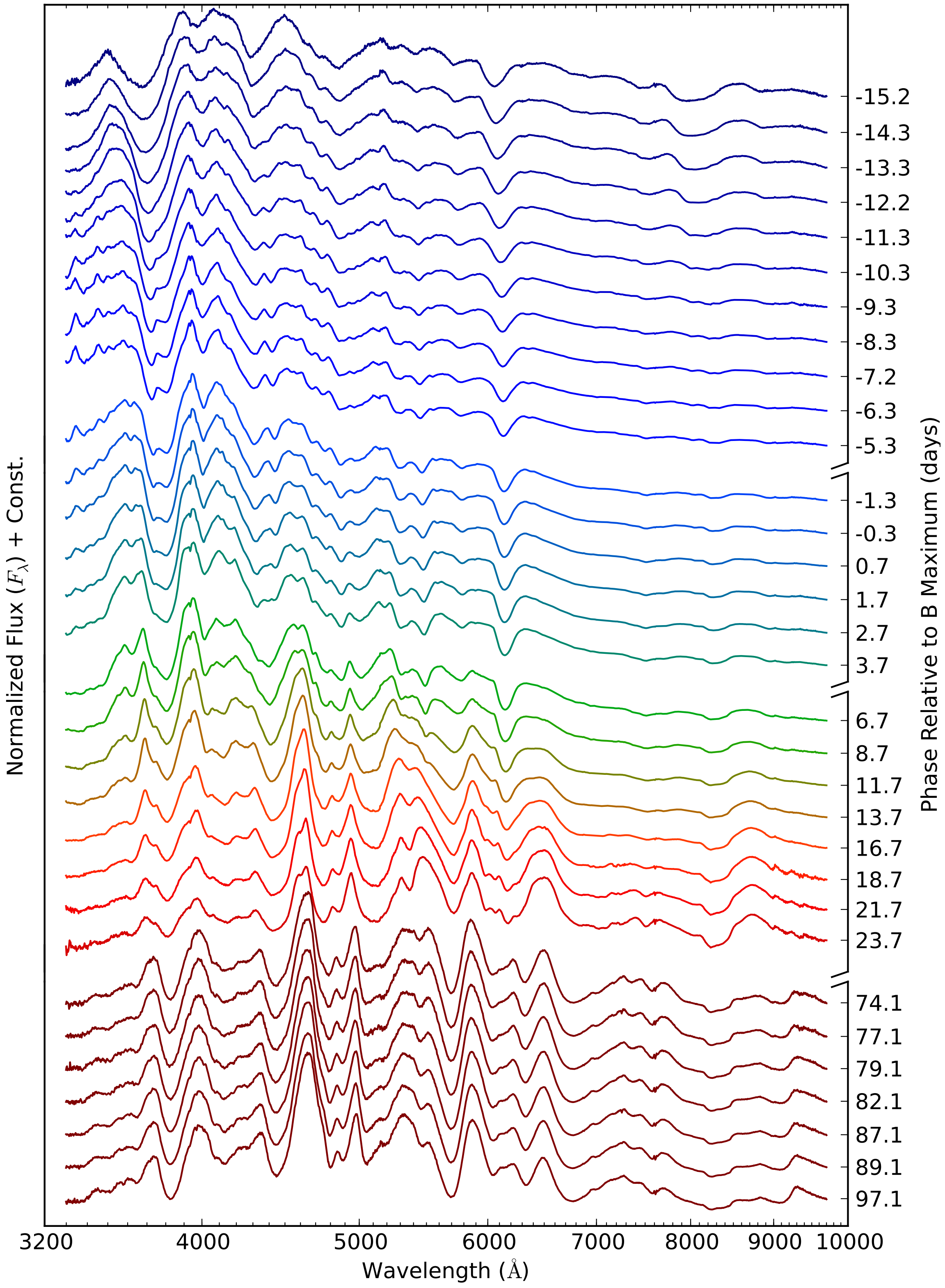

Figure 4.3: SNIFS spectrophotometric time series of SN 2011fe from −15 to 100 days relative to B-band maximum light. (Figure from Pereira et al. 2013)

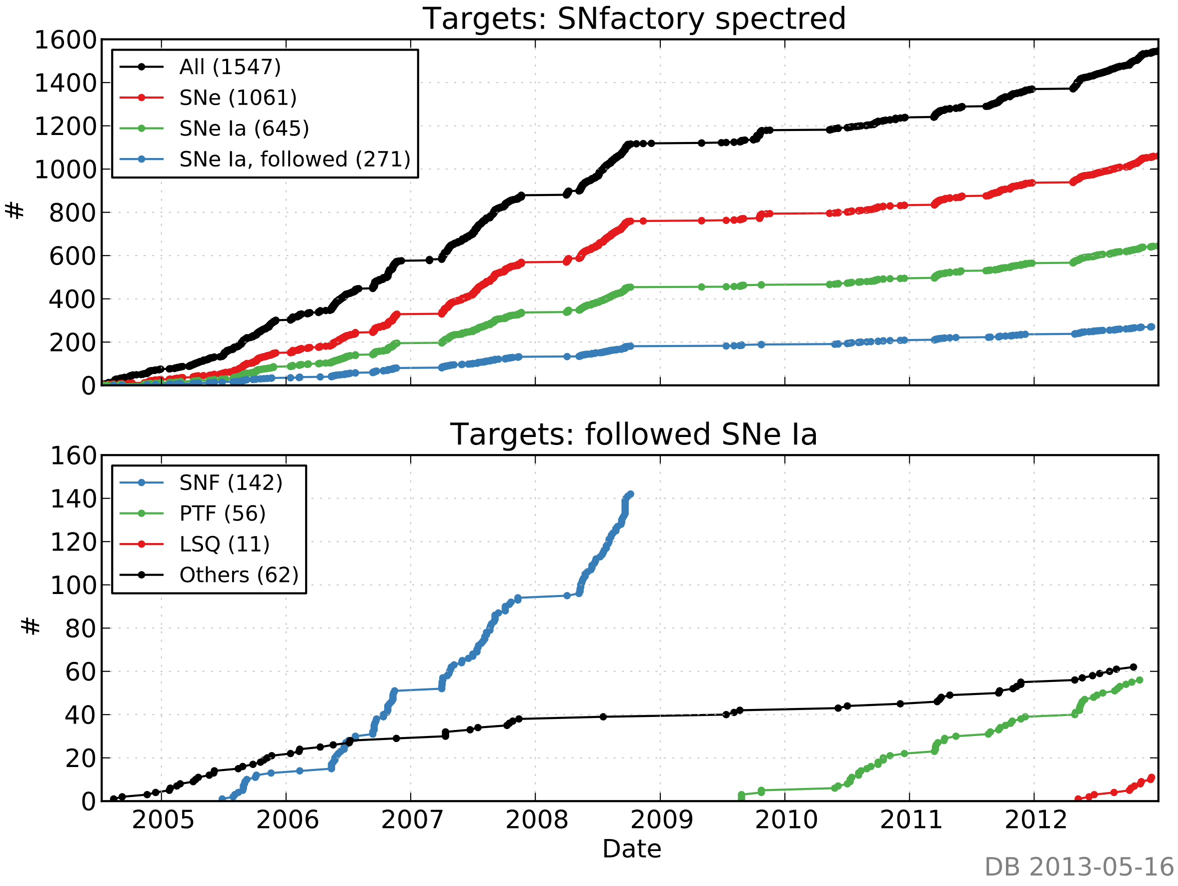

Figure 4.4: Evolution of the number of objects observed by the SNFACTORY. Top panel: number of objects with spectroscopic observation. Bottom panel: number of SNe followed by the SNFACTORY. (Figure from Copin 2013)

obtain lightcurves. Furthermore, each field is scheduled twice a night, a few hours apart, to veto asteroid detection.

After a night's observations are processed, the previous reference images are subtracted and the remaining sources are extracted. Since the resulting set of candidates will be contaminated by various false positives due to e.g. misalignment for subtraction and artefacts of the image reduction, a set of cuts based on their shaped and the number of negative pixels (due to misaligned subtractions) in their vicinity. The cuts were tuned based on a set of images in which fake images of stars were inserted that should then show up as candidates. This filtering process leaves a few hundred objects each night, which are then assessed by a human "scanner" who can distinguish real from bogus object better than the selection cuts. The scanner can also check previous observations of the candidates location to reject it because of previous variability and check catalogues for know variable sources. Since the start of the survey 256 SNe Ia have been found at redshifts $z \lesssim 0.15$ on a $\sim$22000 square degree area of the sky.

4.3 Lightcurve Fitting

For the lightcurves of all SNe used in this analysis the SALT2[2] (Guy et al., 2007, 2010) lightcurve fitter was used to determine width, colour and peak brightness. The fitter is based on an empirical model for the spectrophotometric time evolution of SNe Ia and uses the following functional form for the flux:

$$F(p,\lambda) = x_0 \cdot [M_0(p,\lambda) + x_1 \cdot M_1(p,\lambda)] \cdot \exp(c \cdot CL(\lambda)) \tag{4.1}$$

where the phase p is the rest-frame time since the date of the maximum B-band luminosity. $M_0(p,\lambda)$ is the average spectral sequence whereas $M_1(p,\lambda)$ is an additional component that describes the main variability of SNe Ia. x_0 is the normalization of the spectral energy distribution (SED) and x_1 an intrinsic parameter of the SN which measures its main variability, the brighter-wider relation, with $x_1 = 0$ being the average for all SNe. $CL(\lambda)$ is the average colour correction law for the colour excess $c = (B - V)_{\mathrm{max}} - \langle B - V \rangle$. In summary, the M_0, M_1 and CL are properties of the global model while the x_0, x_1 and c are parameters of a given SN that are determined by the fit. M_0 and M_1 are implemented using third-order B-splines which ensure continuous second derivatives.

The model is defined for p between -20 and 50 days and for λ between 2000 and 9200 Å. While M_0 has 10 parameters in time and 120 in wavelength (yielding a spectral resolution of the order of 60 Å), only 60 wavelength parameter are use for M_1. The colour law CL has only two free parameters as it implemented as a third-order polynomial with the conditions that $CL(\lambda_B) = 0$ and $CL(\lambda_V) = 0.4\log(10)$. This corresponds to the condition that $CL(B) - CL(V) = 1$.

The model is fit to the observed SN lightcurves jointly for all phases to determine x_0, x_1 and c of a supernova as well as the time of its B-band maximum. This is done by redshifting the model, correcting for galactic extinction (using the extinction law from Cardelli et al. (1989) using $R_V = 3.1$) and multiplying by the effective filter transmission functions. The peak B-band magnitude that is used to fit the Hubble law is then determined according to

$$m_B^{\mathrm{max}} = -2.5\log_{10}\left[\int F(0,\lambda) T_B(\lambda) \lambda \mathrm{d}\lambda\right] \tag{4.2}$$

---

[2] `http://supernovae.in2p3.fr/salt/`

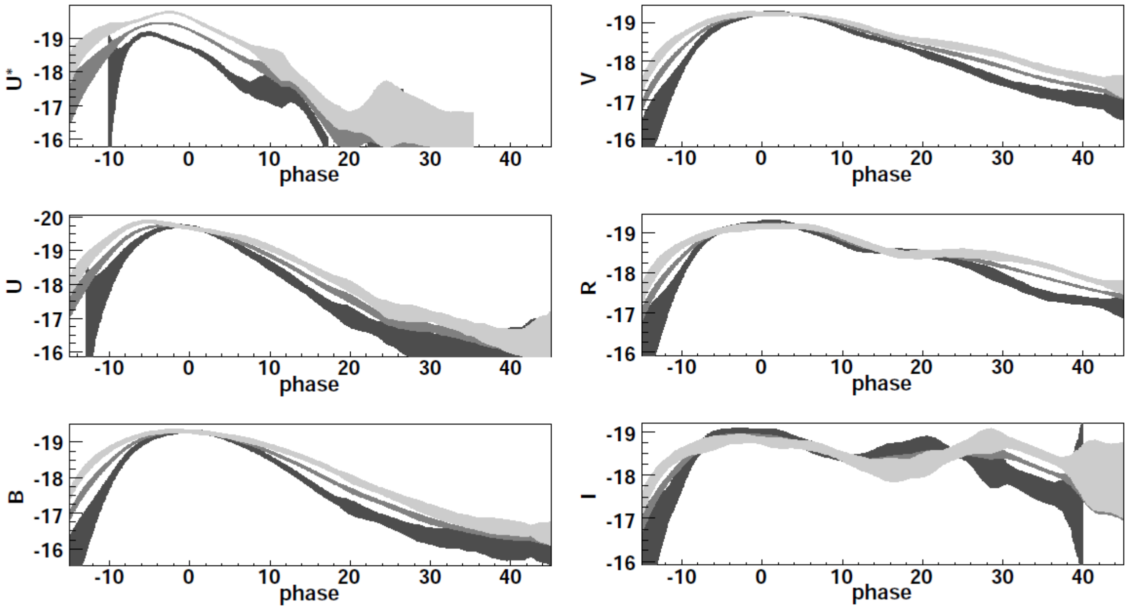

Figure 4.5: SALT2 lightcurve template for U^*UBRIV filters for values of x_1 of $-2, 0, 2$ (dark to light curves). U^* is a synthetic top hat filter in the range 2500-3500Å. (Figure from Guy et al. 2007)

with the B-band transmission function $T_B(\lambda)$ and $F(0, \lambda)$ being the model flux (equation 4.1) at maximum, i.e. $p = 0$. The distance moduli μ_B for each SN can then be obtained by

$$\mu_B = m_B - M + \alpha x_1 - \beta c, \tag{4.3}$$

where α, β and the absolute magnitude M are global parameters in the fit of the SN Hubble diagram.

For the first release of SALT2 (Guy et al., 2007), the model template was trained using a nearby ($0.05 \lesssim z$) and a high-redshift ($0.2 < z \lesssim 1$) SN sample. The nearby sample consisted of 52 SNe from previous surveys selected for their lightcurve sampling quality. For 16 of these SNe spectra were available. Furthermore, UV spectra from the International Ultraviolet Explorer (INES 2006) were included which makes up for the fact that most high-redshift spectra covering rest-frame UV have a low signal-to-noise ratio. The high-redshift sample was a set of 121 SN Ia lightcurves from the first two years of the Supernova Legacy Survey (SNLS). Additionally 39 high-redshift SNLS spectra were used which were obtained at VLT (Balland et al., 2009) and Gemini (Howell et al., 2005) during the SNLS observation programs. With the publication of the SNLS 3-year analysis (Guy et al., 2010), the template was retrained using an extended nearby sample and a sub-sample of the SNLS SNe. Again the SNe were selected for good lightcurve sampling and unambiguous spectroscopic identification. Most recently the template has been updated in the *joint light-curve analysis* (JLA, Betoule et al. 2014), in which the training sample was extended by SDSS-II photometric data. The result of the model training is shown in figure 4.5 for several filter bands and different values of x_1 and figure 4.6 shows the resulting colour law $c \cdot CL(\lambda)$. The analysis presented in this document has been started in 2012 and therefore older versions of the SALT2 template were used for consistency.

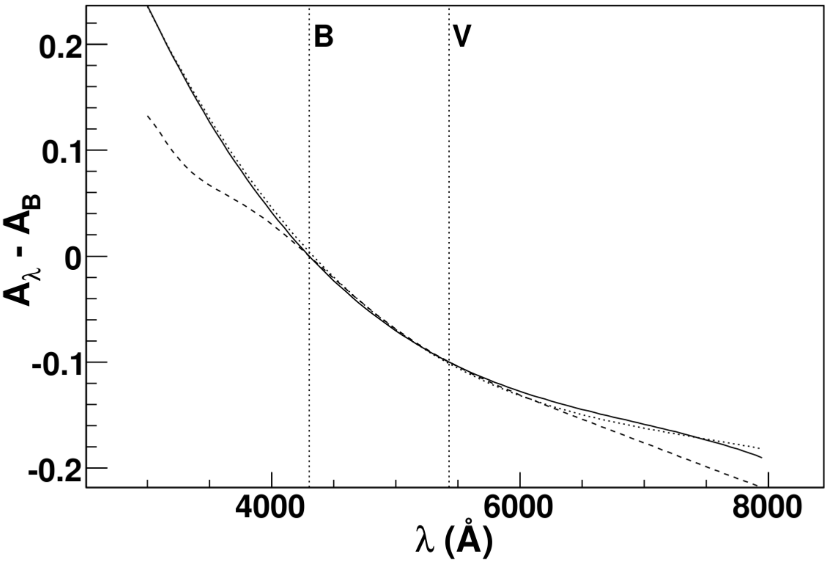

Figure 4.6: SALT2 colour law for a value of $c = 0.1$. The dashed line shows the extinction law with respect to the B-band ($A_\lambda - A_B$) from Cardelli et al. (1989) with $R_V = 3.1$ and $E(B - V) = 0.1$, and the dotted line is the colour law obtained for SALT Guy et al. (2005) which is very close to the SALT2 result. (Figure from Guy et al. 2007)

4.4 Dataset

4.4.1 SNfactory

The analyses in this document are based on the internal data release "ACEv3" of the SNFACTORY dataset. Lightcurves were synthesized from the flux-calibrated spectra as recorded with the SNIFS instrument. For this, box filters were applied roughly matching B, V, and R (see Bailey et al. 2009 for details). The SALT2 lightcurve fitter was then used to standardize the SNe and the following quality criteria were applied:

(a) the SALT2 lightcurve fit includes more than 5 independent epochs,

(b) the normalized median absolute deviation (nMAD) of the fit residuals over all used filters is smaller than 0.2 mag,

(c) there is less than a 20% rejection rate of data points in SALT2,

(d) suspected super-Chandrasekhar SNe were removed (Scalzo et al., 2012).

A sample of 117 SNe Ia passed the selection criteria; 115 of those are at redshifts $0.015 < z < 0.1$, which are of main interest to this study. The lightcurve parameters and Hubble residuals for most of the SNe have previously been published (Bailey et al., 2009; Chotard et al., 2011). The systemic host redshifts are published in Childress et al. (2013a). For the analyses, the data were grouped in redshift bins as given in table 4.1. The redshift bin are the same as those used by Colin et al. (2011), with the exception that we combined their first two bins ($0.015 < z < 0.025$ and $0.025 < z < 0.035$) into one as the SNFACTORY dataset only contains few SNe at $z < 0.03$. Figure 4.7 shows the radial peculiar velocities of individual SNe[3] and their distribution on the sky in the four low redshift bins for the Union2 and

---

[3] For each SN, the velocity was determined from its luminosity distance and its Hubble residual by solving equation (2.54) for v.

z	Number of SNe Union2	 SNFACTORY
0.015-0.035*	109	20
0.035-0.045	16	20
0.045-0.06	17	21
0.06-0.1	23	54
0.1-0.2	55	–
0.2-0.3	62	–
0.3-0.4	62	–
0.4-0.5	58	–
0.5-0.6	44	–
0.6-0.8	50	–
0.8-1.4	60	–

Table 4.1: Numbers of SNe per redshift bin for the Union2 and SNFACTORY datasets. Note: *SN 2005eu (= SNF20051003-004) is included in both datasets. The Union2 measurement was used for the combined datasets.

SNFACTORY datasets respectively. The SNFACTORY dataset is limited to declinations easily observable from Mauna Kea ($-25° < \delta < 65°$) and therefore covers approximately 70% of the sky.

4.4.2 Union2 Compilation

In addition to the SNFACTORY dataset, the 557 SNe from the Union2 compilation (Amanullah et al., 2010) are used in this thesis. Union2 combined the world's SN Ia data of samples in various redshift ranges at the time of its publication. The nearby samples include the Calan/Tololo survey (Hamuy et al., 1996b), the SCP nearby 1999 Supernova Campaign (results presented in the first Union compilation Kowalski et al. 2008) and CfA3 (Hicken et al., 2009a). For the redshift range $0.3 < z < 1.0$ the SNe are taken from (among others) the early SCP and HZT samples (Perlmutter et al., 1999; Riess et al., 1998) and more recent surveys like the first year SNLS data (Astier et al., 2006) and ESSENCE (Miknaitis et al., 2007; Wood-Vasey et al., 2007). The gap between nearby and distant SNe is closed by the SDSS SN survey (Holtzman et al., 2008; Kessler et al., 2009) which provides SNe at $0.1 < z < 0.3$, a redshift range relatively neglected until then. For redshift larger than $z \sim 1$, ground-based observations become less feasible and hence the Hubble Space Telescope (HST) played a key role in the optical and infrared follow-up (Knop et al., 2003; Tonry et al., 2003; Barris et al., 2004) and also in carrying out an own SN search and follow-up using the Advanced Camera for Surveys (ACS Riess et al. 2004, 2007). Also along with the Union2 compilation new SNe followed-up by the HST were published. The Union2 compilation has since then been updated to the Union2.1 compilation (Suzuki et al., 2012) but this new compilation contains only few new SNe, all of which are at high redshifts

When combining these samples to a dataset, several analysis issues must be addressed. For the first Union compilation (Kowalski et al., 2008) these issues were described in a list of goals which needed to be achieved by the dataset:

(a) The analysis needs to account for the heterogeneous nature of the dataset. This was addressed by Kowalski et al. by weighting each sample according to the dispersion that was determined for it, i.e. different values of the intrinsic scatter σ_{int} are used for each sample, hence deweighting samples with significant unaccounted statistical or systematic uncertainties.

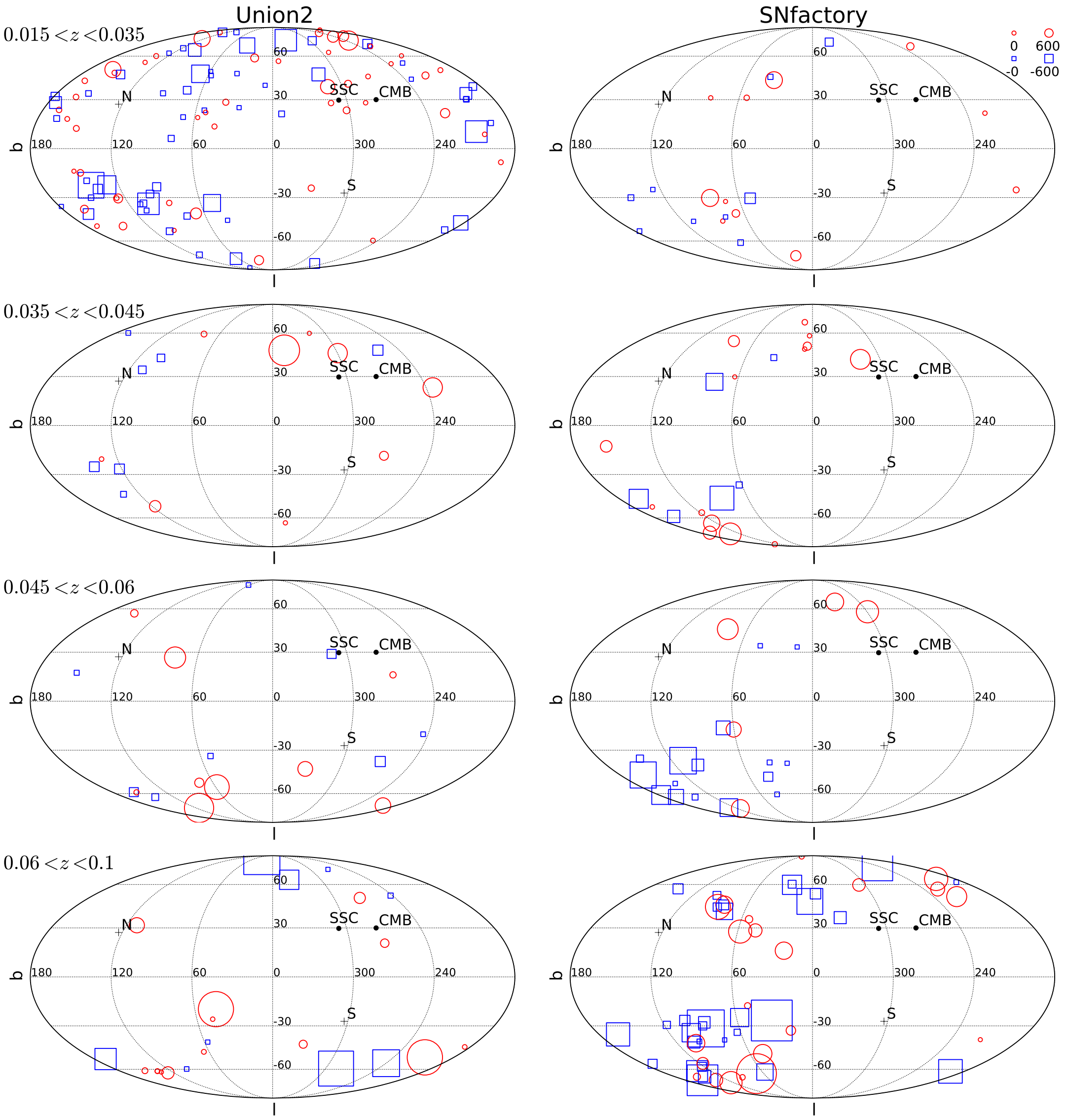

Figure 4.7: Peculiar velocities of individual SNe determined determined from their luminosity distances and Hubble residuals by solving equation (2.54) for v. The plot shows the Union2 (left column) and SNFACTORY (right column) datasets in the redshift bins $0.015 < z < 0.035$ (first row), $0.035 < z < 0.045$ (second row), $0.045 < z < 0.06$ (third row) and $0.06 < z < 0.1$ (fourth row). The marker diameter of each SN is proportional to the absolute value of the velocity plus an offset (see the scale at the top right), with red circles corresponding to positive velocities and blue squares corresponding to negative ones. For reference, the directions of the CMB dipole and the Shapley supercluster (SSC) are shown.

(b) The various samples should be analysed using the same procedure. This requires all SNe to be fit with the same lightcurve fitter, SALT2 in the case of Union2.

(c) The quality requirements for the SNe should be reproducible and well-characterized. Earlier compilations relied heavily on the heterogeneous classification information provided by the original authors. This can be avoided by adopting a robust analysis technique based on outlier rejection that was shown to be resilient against contamination.

(d) The analysis should introduce as little bias as possible to the fit. This was achieved by using a blinded analysis chain, i.e. hiding the resulting cosmological parameters until the analysis is finalized.

Like the SNFACTORY dataset, the distribution in the redshift bins and on the sky of the SNe in the Union2 compilation are shown in table 4.1 and figures 4.7 and 4.8. The dataset is well distributed on the sky for low redshifts but are increasingly clustered for higher redshifts, first along lines and then in relatively small fields. While the Union2 compilation contains 164 SNe at redshifts $z < 0.1$, most of them (109) are in the first bin ($z < 0.035$). Therefore, the SNFACTORY data greatly expands the data available in the intermediate range ($0.035 < z < 0.1$).

4.4.3 SNe in Galaxy Clusters

The peculiar velocities of galaxies and SNe in galaxy clusters are dominated by virial motion. Since this analysis focuses on large-scale correlations between the velocities, the redshifts of the galaxies are a better choice than the host galaxy redshifts. Since galaxy clusters roughly have a radius of the order of 1 Mpc, the error introduced by using the cluster redshift is smaller than the potential virial component of the peculiar velocity, which can be of the order of $1000\,\mathrm{km\,s^{-1}}$.

To determine whether a SN host galaxy is located in a galaxy cluster, the NASA/IPAC Extragalactic Database (NED[4]) was queried for galaxy clusters within a projected transverse separation of 1 Mpc and a redshift difference $\Delta z < 0.01$ (corresponding to $\sim 40\,\mathrm{Mpc}$). The redshift criterion was left very wide, to allow finding clusters with large velocity dispersions. The query results were then further investigated by comparing the redshift difference to velocity dispersions reported in analyses of the clusters. Therefore, only clusters that were thoroughly studied and have several references were considered for this correction. In the two datasets a total of 11 SNe were found to be located in a galaxy cluster according to the criteria explained above, see table 4.2.

4.4.4 Combined Dataset

After analysing the datasets separately, they were combined to create a new sample of 279 SNe[5] spanning $0.015 < z < 0.1$. As the absolute magnitudes, M, of the SNe and the parameters α and β of equation (2.4) were determined separately for the datasets following the Union procedure, their normalizations may differ. This would lead to a larger than usual scatter of the Hubble residuals. Therefore, an offset between the distance moduli was determined in a χ^2 fit of a flat ΛCDM cosmology, with Ω_M and the absolute corrected magnitude M of SNe the parameters of the fit. These parameters were determined using all 674 SNe of both datasets (including the two SNe in the SNFACTORY dataset that are outside of the redshift range $0.015 < z < 0.1$) and were left blinded to preserve the impartiality of ongoing SNFACTORY cosmology analyses.

---

[4] `http://ned.ipac.caltech.edu/`

[5] SN 2005eu (Hicken et al., 2009a) was also observed by the SNFACTORY as SNF20051003-004. We included it in both datasets when analysing them separately. Since the results agree we only used the Union2 value in the combined dataset.

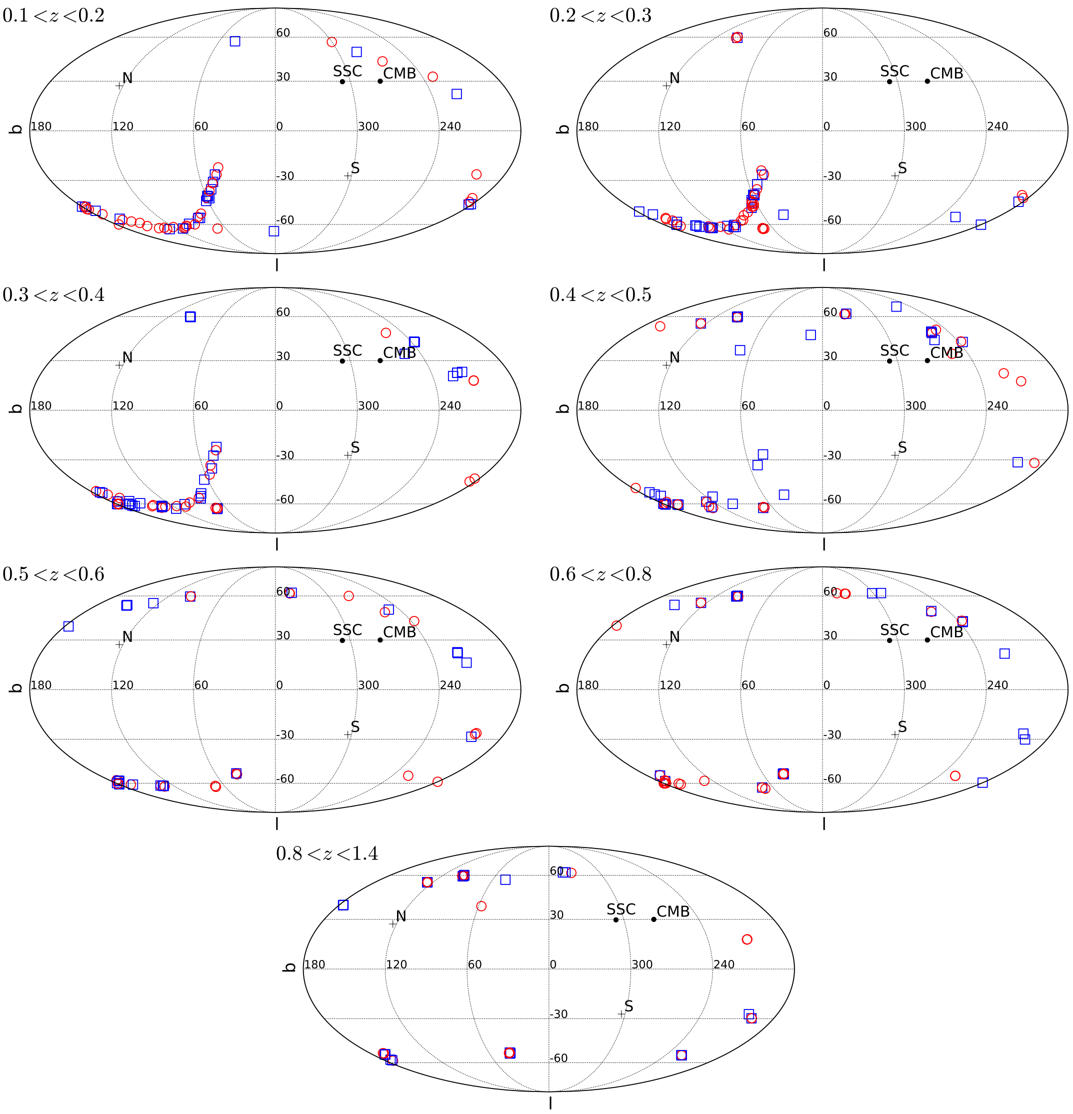

$0.1 < z < 0.2$ $0.2 < z < 0.3$ $0.3 < z < 0.4$ $0.4 < z < 0.5$ $0.5 < z < 0.6$ $0.6 < z < 0.8$ $0.8 < z < 1.4$

Figure 4.8: Distribution the high-redshift Union2 SNe on the sky for the redshift bins as used in the analysis. Unlike figure 4.7, the marker diameter does not correspond to the absolute value of the velocities, but the colours and shapes still distinguish SNe with positive velocities (red circles) from those with negative ones (blue squares).

SN Name	z_{host}	RA [°]	Dec. [°]	Cluster Name	z_{cluster}
SNFACTORY					
PTF09foz	0.053156	10.55	-9.88	ABELL 0087	0.053909
SNF20061020-000	0.037225	10.27	6.79	ABELL 0076	0.039510
SNF20080731-000	0.075091	266.01	33.04	ZwCl 1742.1+3306	0.075474
Union2					
SN 1993ah	0.028500	357.96	-27.96	ABELL 4049	0.028907
SN 1993O	0.052900	202.78	-33.22	ABELL 3560	0.049825
SN 1998dx	0.053700	272.80	49.86	UGCl 442	0.049784
SN 2003ic	0.054600	10.46	-9.31	ABELL 0085	0.054534
SN 2005hf	0.042100	21.77	19.12	ABELL 0195	0.041986
SN 2006al	0.069000	159.87	5.18	ABELL 1066	0.071097
SN 2007ci	0.019200	176.44	19.77	ABELL 1367	0.023093
SN 2008L	0.018900	49.32	41.38	Perseus CLUSTER	0.017363

Table 4.2: SNe in galaxy clusters with their host galaxy redshift z_{host} and cluster redshift z_{cluster}.

CHAPTER 5

Anisotropy Models

In this chapter the models that constrain anisotropy in the universe are described. The first model measures the velocity dipole amplitude and direction in redshift shells, which quantifies the bulk flow on various scales. The second model analyses the anisotropy in a more general way by smoothing the error-weighted Hubble residuals as a function of the direction. The third method describes to peculiar velocity field of a simple gravitational attractor, which can be used to constrain the mass of structures such as the Shapley supercluster (SSC). The fourth and final method represents an extension of the first by adding monopole and shear terms. Results for the first three methods will be presented in chapters 6 and 7. The last method cannot be constrained with the data at hand and will be investigated using simulations in chapter 8.

5.1 Dipole Fit

The simplest model for anisotropy is a peculiar velocity dipole. This corresponds to a bulk flow, i.e. the coherent motion of galaxies in the same direction at the same speed. While a dipole motion is expected on small scales, finding it on large scales would challenge our understanding of ΛCDM structure formation, which predicts the coherent motion to decrease with the size of the volume, over which it is averaged. As stated in section 3.2.3, the bulk flow is expected to be reciprocal to the distance, with an amplitude of $\lesssim 250\,\mathrm{km\,s^{-1}}$ at $z = 0.033$ and $\lesssim 80\,\mathrm{km\,s^{-1}}$ at $z = 0.1$.

The effect of anisotropy on our observations can be expressed as the angular power spectrum of fluctuations of the luminosity distance (Bonvin et al., 2006a). When recalculating the luminosity distance using a metric with a dipole anisotropy, one finds that the luminosity distance d_L from an unperturbed FLRW metric becomes

$$\begin{aligned}\tilde{d}_\mathrm{L}(z) &= d_\mathrm{L}(z) + d_\mathrm{L}^{(1)}(z)\\ &= d_\mathrm{L}(z) + \frac{(1+z)^2}{H(z)}\boldsymbol{n}\cdot\boldsymbol{v}_\mathrm{d}\end{aligned} \tag{5.1}$$

where $\boldsymbol{n}$ is the unit vector of the observed object's position and $\boldsymbol{v}_\mathrm{d}$ is the dipole velocity vector (Bonvin et al., 2006b). Note that this formula is very similar to equation (2.54) for the luminosity distance of an object with a peculiar velocity. In fact it follows directly from it by setting $\boldsymbol{v}_\mathrm{e} = 0$. This corresponds to a universe in which only the observer has a peculiar velocity.

For an object at galactic coordinates (l_i, b_i) and redshift z_i the dipole term in equation (5.1) becomes

$$d_{\mathrm{L}}^{(1)}(z_i, l_i, b_i; v_{\mathrm{d}}, l_{\mathrm{d}}, b_{\mathrm{d}}) = \frac{(1+z_i)^2 v_{\mathrm{d}}}{H(z_i)} \cos(\Delta\theta\,(l_i, b_i, l_{\mathrm{d}}, b_{\mathrm{d}}))\,, \tag{5.2}$$

where $\Delta\theta$ is the angle between the position vector of the object (defined by l_i and b_i) and the direction of the dipole (defined by l_{d} and b_{d}). This angular separation can be calculated from the scalar product of the corresponding unit vectors:

$$\cos(\Delta\theta\,(l_i, b_i, l_{\mathrm{d}}, b_{\mathrm{d}})) = \sin b_i \sin b_{\mathrm{d}} + \cos b_i \cos b_{\mathrm{d}} \cos(l_i - l_{\mathrm{d}})\,. \tag{5.3}$$

The dipole can thus be constrained by minimizing the variance-weighted least-squares function

$$\chi^2 = \sum_{i=1}^{n} \frac{\left|\mu_i - 5\log_{10}\left(\left(d_{\mathrm{L}}(z_i) - d_{\mathrm{L}}^{(1)}(z_i, l_i, b_i; v_{\mathrm{d}}, l_{\mathrm{d}}, b_{\mathrm{d}})\right)/10\,\mathrm{pc}\right)\right|^2}{\sigma_i^2}, \tag{5.4}$$

for the parameters v_{d}, l_{d} and b_{d}, where μ_i are the observed distance moduli and the uncertainties σ_i include an intrinsic scatter term of ~ 0.15 mag. Note that the sign in front of $d_{\mathrm{L}}^{(1)}$ was changed. This is necessary because the observed redshifts are used, i.e. those including the effect of peculiar velocities. Since the dipole velocity amplitude v_{d} is used as a linear coefficient above. Mathematically, negative values are therefore allowed and due to rotational symmetry, minimizing χ^2 for v_{d} in opposite directions would only result in a sign change. To break this degeneracy, the χ^2 value will be set to the value for $v_{\mathrm{d}} = 0$ if the best-fit value for a given direction is negative. Alternatively, the $\boldsymbol{v}_{\mathrm{d}}$ can be expressed in Cartesian coordinates, for which the dipole term becomes

$$d_{\mathrm{L}}^{(1)}(z_i, l_i, b_i; v_x, v_y, v_z) = \frac{(1+z_i)^2}{H(z_i)} \left(v_x \cos b_i \cos l_i + v_y \cos b_i \sin l_i + v_z \sin b_i\right). \tag{5.5}$$

In this representation, no degeneracy occurs and the minimization converges better numerically. Therefore the dipole fit results listed in section 6.1 were calculated in Cartesian coordinates and then converted to spherical coordinates, which are easier to interpret.

For a single velocity component (Cartesian or spherical), the uncertainties (at 68% confidence level) of the components of $\boldsymbol{v}_{\mathrm{d}}$ can be determined by finding the values for which the χ^2-value increases to $\Delta\chi^2 = 1$ while marginalizing over the other parameters. When converting between coordinate systems, however, one requires the full covariance matrix of the parameters to propagate their uncertainties properly. This can be obtained from the Jacobian of the error-weighted residuals:

$$\mathrm{Cov}(\boldsymbol{v}_{\mathrm{d}}) = \left(J^{\mathrm{T}} J\right)^{-1} \tag{5.6}$$

$$\text{with} \quad J = \begin{pmatrix} \frac{\partial q_1}{\partial v_1} & \frac{\partial q_1}{\partial v_2} & \frac{\partial q_1}{\partial v_3} \\ \vdots & \vdots & \vdots \\ \frac{\partial q_n}{\partial v_1} & \frac{\partial q_n}{\partial v_2} & \frac{\partial q_n}{\partial v_3} \end{pmatrix}, \tag{5.7}$$

$$q_i = \frac{\mu_i - 5\log_{10}\left(\left(d_{\mathrm{L}}(z_i) - d_{\mathrm{L}}^{(1)}(z_i, l_i, b_i; v_{\mathrm{d}}, l_{\mathrm{d}}, b_{\mathrm{d}})\right)/10\,\mathrm{pc}\right)}{\sigma_i}. \tag{5.8}$$

To express the significance of the results in a single value instead of three separate uncertainties of the fit parameters, two very similar tests to determine the p-value of the results were performed. They will be referred to as tests A and B:

A) The dataset is split into a list of (z_i, μ_i, σ_i) and one of (l_i, b_i). The latter is shuffled and recombined with the former.

B) The values of μ_i are replaced by the expected values from Hubble's law at redshift z_i ($\mu = 5\log_{10}(d_\mathrm{L}(z_i)/10\,\mathrm{pc})$) and then offset by a random value drawn from a Gaussian distribution of width σ_i.

Test A was used in Feindt et al. (2013), in which part of the analysis presented in this thesis has been published. Test B, on the other hand, was used in Colin et al. (2011) and a comparison of the methods was made in Appleby & Shafieloo (2014). Both methods will recreate random datasets that are expected to contain no anisotropy signal but may show one by random chance. By comparing the χ^2-value at minimum for the real data from that of large number of random samples, the anisotropy hypothesis against the null hypothesis of a completely isotropic universe. The fraction of random datasets that have a lower χ^2-value than the real data is called the p-value and states the probability of an anisotropy signal being due to random noise.

The difference between tests A and B consists in the assumed distributions. While test A uses an empirical distribution by redistributing the measured values, test B makes use of the assumption that our measurement uncertainties are Gaussian (which is implicitly used when minimizing χ^2). Furthermore test A generates a dataset with objects at the same coordinates (l_i, b_i) but possibly at different redshifts z_i, whereas test B keeps the object at the same coordinates and redshifts fixed. Despite these differences both tests are expected to give similar distributions of χ^2-values. For test B, this distribution is the probability density function of the statistical χ^2-distribution. For test A, the distribution is expected to be very similar to that since the residuals have any approximately Gaussian distribution.

The procedure did not account for cosmic variance, i.e. the fact that one can only observe a single universe with a single realization of the random structure formation, in the determination of the p-values and thus may underestimate the uncertainties. For a typical magnitude of the cosmic variance ($\sim 100\,\mathrm{km\,s^{-1}}$), the intrinsic dispersion will dominate the uncertainties for all but the nearest redshifts for the SN dataset analysed in this document. Furthermore, the uncertainties of μ_i were treated as being uncorrelated, but peculiar velocities are expected to be correlated because the closer two objects are to each other, the more likely they will be attracted by the same structure (Hui & Greene, 2006; Gordon et al., 2007, 2008; Davis et al., 2011b). To verify the latter claim, the covariance derived from the full power spectrum of the velocity correlation function according to Hui & Greene (2006) was compared to that expected for a bulk flow of $300\,\mathrm{km\,s^{-1}}$, which is already included through the dipole model (figure 5.1). The correlation for a dipole is larger than the full correlation for objects with separations $\gtrsim 70\,\mathrm{Mpc}$. For the datasets used here, only few SNe at low redshifts are closer to each other than that. Therefore, the effect is expected to be small for the higher-redshift bins ($z > 0.035$) where the main interest of this study lies. Furthermore, the effect of the random noise of the sample is expected to be dominant compared to the either covariance term and thus reduces the correlation.

Additionally, since the analysis will be performed for two datasets and their combination, one must investigate possible tension between the samples that are to be combined. For this a scheme similar to the consistency test described by Watkins et al. (2009) can be used. It uses the following value to compare the results:

$$\Delta^2 = \sum_{i,j} \left(\Delta v_\mathrm{d}^{(i)}\right) \left(C^{-1}\right)_{ij} \left(\Delta v_\mathrm{d}^{(j)}\right) \tag{5.9}$$

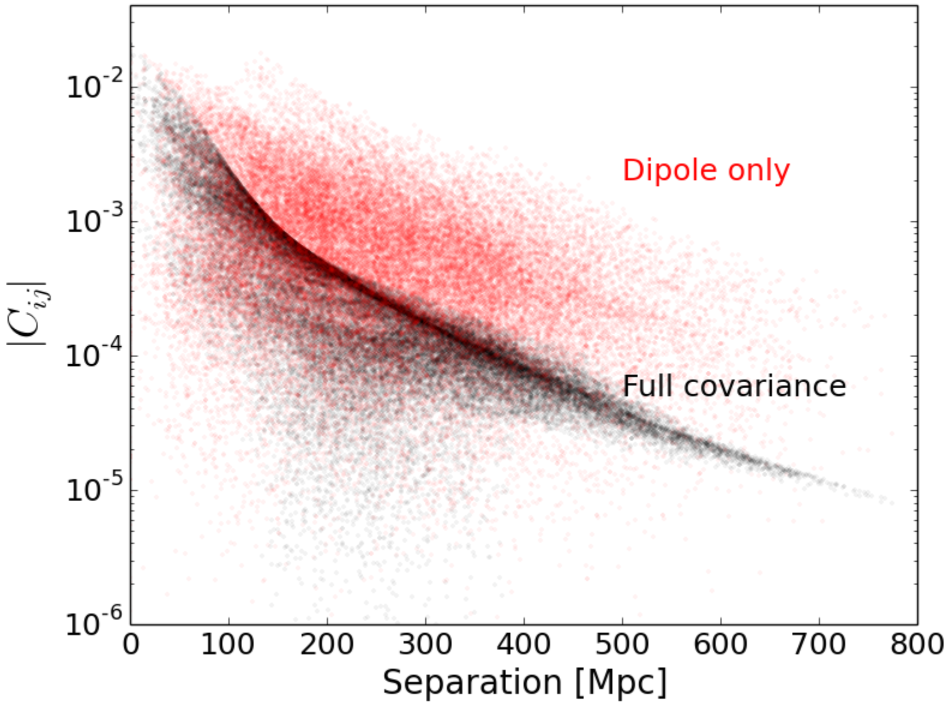

Figure 5.1: Absolute values of the covariance of luminosity distances as function of separation between two SNe for the combined dataset at redshifts $z < 0.1$. The black markers show the full covariance calculated from the full peculiar velocity power spectrum using the code from Hui & Greene (2006, `http://user.astro.columbia.edu/~lhui/PairV/index.html`); the red markers show only the contribution of the dipole component expected from a bulk flow of 300 km s^{-1}. The latter covariance term dominates the correlation for separation $\gtrsim 70$ Mpc

where $\Delta v_{\mathrm{d}}^{(i)}$ are the Cartesian components of the vectorial difference between the bulk flow estimates from each sample and C is their combined covariance. This consistency check is based on χ^2 statistics, but the value calculated in the equation above was named Δ^2 here instead of χ^2 (as in Watkins et al. 2009) to avoid confusion with the definition of χ^2 used in equation (5.4). The probability for the tension to be real can be determined using the χ^2 probability distribution function:

$$\chi_k^2(x) = \frac{1}{2^{\frac{k}{2}}\Gamma\left(\frac{k}{2}\right)} x^{\frac{k}{2}-1} e^{-\frac{x}{2}}, \tag{5.10}$$

where Γ is the Gamma function and k is the number of degrees of freedom (3 in this case). The probability that the tension is not random is then found by integrating equation (5.10) for values $x > \Delta^2$.

5.2 Smoothed Residuals

As an alternative method to detect more general anisotropies, the direction with the highest deviation from an isotropic universe can be identified using the method of *smoothed residuals*. The required test statistic is calculated from the error-weighted Hubble residuals r_i, similar to q_i in equation (5.8),

$$r_i = \frac{\mu_i - 5\log_{10}\left(d_{\mathrm{L}}(z_i)/10\,\mathrm{pc}\right)}{\sigma_i}. \tag{5.11}$$

To calculate the value of the test statistic at given direction (l, b), the residuals are then weighted by the angular separation of their coordinates to that direction:

$$Q(l_{\mathrm{SR}}, b_{\mathrm{SR}}) = \frac{\sum_i W(l_{\mathrm{SR}}, b_{\mathrm{SR}}, l_i, b_i) r_i}{\sum_i W(l_{\mathrm{SR}}, b_{\mathrm{SR}}, l_i, b_i)}, \tag{5.12}$$

where the window function $W(l_{\mathrm{SR}}, b_{\mathrm{SR}}, l_i, b_i) \equiv W_i$ reads

$$W(l_{\mathrm{SR}}, b_{\mathrm{SR}}, l_i, b_i) = (2\pi\delta^2)^{-1/2} \exp\left(-\frac{\Delta\theta(l_{\mathrm{SR}}, b_{\mathrm{SR}}, l_i, b_i)^2}{2\delta^2}\right). \tag{5.13}$$

Here δ is a smoothing parameter, which in the following is chosen as 90° in order to identify dipoles in the Hubble expansion. (l_i, b_i) are the coordinates of a SN and $(l_{\mathrm{SR}}, b_{\mathrm{SR}})$ those of the direction in which Q is evaluated. While the angular separation $\Delta\theta$ can be calculated by taking the arccosine of equation (5.3), this formula has been shown to be numerically inaccurate for small separations because in those cases where the cosine is close to 1 and rounding errors may occur. Even though this numerical instability is of no great concern for this analysis since the window function is flat around zero, an alternative formula based on the tangent was used because it is accurate at all separations. It can be derived from the scalar and cross products of two unit vectors $\boldsymbol{n}_1$ and $\boldsymbol{n}_2$:

$$\boldsymbol{n}_1 \cdot \boldsymbol{n}_2 = \cos(\Delta\theta) \tag{5.14}$$

$$|\boldsymbol{n}_1 \times \boldsymbol{n}_2| = \sin(\Delta\theta) \tag{5.15}$$

$$\Rightarrow \tan(\Delta\theta) = \frac{|\boldsymbol{n}_1 \times \boldsymbol{n}_2|}{\boldsymbol{n}_1 \cdot \boldsymbol{n}_2}. \tag{5.16}$$

The expression for the scalar product in spherical coordinates is given in equation (5.3); the cross product can be written as

$$|\boldsymbol{n}_1 \times \boldsymbol{n}_2| = \sqrt{(\cos b_2 \sin \Delta l)^2 + (\cos b_1 \sin b_2 - \sin b_1 \cos b_2 \cos \Delta l)^2}. \tag{5.17}$$

Instead of simply taking the arctangent of equation (5.16), it is better to use the arctan2 function implement in many programming languages:

$$\operatorname{arctan2}(y, x) = \begin{cases} \arctan \frac{y}{x} & \text{for } x > 0 \\ \arctan \frac{y}{x} + \pi & \text{for } y \geq 0, x < 0 \\ \arctan \frac{y}{x} - \pi & \text{for } y < 0, x < 0 \\ +\frac{\pi}{2} & \text{for } y > 0, x = 0 \\ -\frac{\pi}{2} & \text{for } y < 0, x = 0 \\ \text{undefined} & \text{for } y = 0, x = 0 \end{cases}. \tag{5.18}$$

The angular separation then becomes:

$$\begin{aligned} \Delta\theta &= \operatorname{arctan2}(|\boldsymbol{n}_1 \times \boldsymbol{n}_2|, \boldsymbol{n}_1 \cdot \boldsymbol{n}_2) \\ &= \operatorname{arctan2}\Big(\sqrt{(\cos b_2 \sin \Delta l)^2 + (\cos b_1 \sin b_2 - \sin b_1 \cos b_2 \cos \Delta l)^2}, \\ &\qquad \sin b_1 \sin b_2 + \cos b_1 \cos b_2 \cos \Delta l \Big) \end{aligned} \tag{5.19}$$

When using the smoothed residual method, the directions for the extreme values of Q need not be on exactly opposite sides of the sky but for a large smoothing scale such as $\delta = 90°$ this is very likely. Therefore, it is of interest to record the directions of both Q_{max} and Q_{min}. Since objects moving away from us faster than the Hubble expansion have a negative Hubble residual (they are brighter than expected for their redshifts), the direction of Q_{min} will roughly correspond to that of the dipole fit. As for the dipole fit, p-values can be calculated using the randomization methods described in the previous section with $\Delta Q = Q_{\text{max}} - Q_{\text{min}}$ as the quantity defining the distribution. The p-value is then the fraction of random samples with a larger ΔQ.

Alternatively to the smoothed residuals described above, just the numerator of equation (5.12) can be used to define non-normalized smoothed residuals:

$$\tilde{Q}(l_{\text{SR}}, b_{\text{SR}}) = \sum_i W(l_{\text{SR}}, b_{\text{SR}}, l_i, b_i) r_i. \tag{5.20}$$

In the original study (Feindt et al., 2013) normalized smoothed residuals were used, which were adapted from the non-normalized ones used in Colin et al. (2011). The division by the sum of the weights in the definition of Q was introduced in order to avoid large values in regions that are oversampled. This effect could could shift the direction of maximum anisotropy to those regions. However, the normalization may also lead to less significant results if the oversampled region is located in the actual dipole direction because it suppresses those regions by division with a large value. This difference between these test statistics has been discussed based on simulations by Appleby & Shafieloo (2014); a comparison based on data will made in the next chapter.

5.3 Gravitational Attractor

As an alternative to the general tests of anisotropy described in the previous sections, equations (2.39) and (2.54) can be used to constrain the mass of an overdensity (e.g. the SSC) directly. The study is restricted to the simplified model of a spherical attractor with constant density ρ and radius $R = 50\,\mathrm{Mpc}$, which therefore has a total mass of

$$M_{\mathrm{attractor}} = \frac{4\pi R^3}{3}\rho. \tag{5.21}$$

This approach was also chosen in Muñoz & Loeb (2008), where the authors point out that the SSC is not an object at linear scale[1] but that results from linear theory will still give good estimates of the velocities. Also, because the observed bulk motion at larger redshifts is only marginally significant, this approach is chosen in favour of a more conventional reconstruction of the entire galaxy density field (as in e.g. Erdoğdu et al. 2006; Lavaux et al. 2010; Tully et al. 2014) which would require larger SN statistics for meaningful results.

Furthermore, the region of interest is located at the distance of the SSC and beyond where the SNfactory dataset contributes the most new data. At lower redshifts, where the overdensities have already been mapped, the model will be much less accurate because known (but less massive) structures are not included.

For a simple spherical attractor the density contrast can be defined as a function of the the distance r to the centre of the attractor:

$$\delta(r) = \begin{cases} \delta_0 & \text{for } r < R_{\mathrm{att}} \\ 0 & \text{for } r \geq R_{\mathrm{att}} \end{cases}, \tag{5.22}$$

where R_{att} is the radius of the attractor. Using equation (2.39) and solving the integral therein, the peculiar velocity then becomes:

$$\boldsymbol{v}_{\mathrm{pec}}(\boldsymbol{x}) = \frac{\Omega_{\mathrm{m}}^{0.55} H_0 \delta_0}{3(1+z)} (\boldsymbol{r}_{\mathrm{att}} - \boldsymbol{x}) \begin{cases} 1 & \text{for } r < R_{\mathrm{att}} \\ R_{\mathrm{att}}^3 / r^3 & \text{for } r \geq R_{\mathrm{att}} \end{cases}, \tag{5.23}$$

where $\boldsymbol{x}$ is the position vector pointing from the observer to the peculiar velocity probe (SN in our case) and $\boldsymbol{r}_{\mathrm{att}}$ the vector to the centre of the attractor. The calculations of distance are performed using proper distances and Euclidean geometry. While the latter assumption is technically incorrect in the curved FLRW metric, the results are expected to be sufficiently accurate for the distances investigated here. When assuming this density contrast, the total mass of the attractor is given by rewriting equation (5.21) as

$$M_{\mathrm{att}} = \frac{4\pi R_{\mathrm{att}}^3}{3} \rho_c \Omega_M (1 + \delta_0). \tag{5.24}$$

The overdensity profile within the sphere is of little importance to our analysis as most SNe are outside its boundary. However, as a single object inside the sphere can have a large effect on the results, one needs to decrease its influence by introducing weights w_i that are defined as

$$w_i = \begin{cases} \sin^{16}\left(\frac{\pi}{2}\frac{r_i}{R}\right) & \text{for } r_i < R \\ 1 & \text{for } r_i \geq R \end{cases} \tag{5.25}$$

---

[1] Linear structure formation theory (section 2.3) assumes that the density contrasts are small ($\delta \ll 1$), but the SSC is considerably more dense ($\delta > 1$).

where r_i is the distance from the centre of the overdensity for i-th object. This particular shape of the weighting function was chosen for two reasons: (1) a sine-function was used because it grows monotonously up to $\pi/2$, where has a maximum – this makes the transition to the constant weight outside the attractor smooth – and (2) the large exponent leads to a rapid decrease of the function when approaching the centre of the attractor; the weight is 0.45 for $r_i = 0.8R$ and 0.03 for $r_i = 0.6R$.

The constant density contrast, δ_0, is then determined by minimizing the expression

$$\chi^2 = \sum_i \frac{\left|\mu_i - \log_{10}\left(d_\mathrm{L}(z_i)\left(1 + \left(1 - \frac{(1+z_i)^2}{H(z_i) d_\mathrm{L} z_i}\right)\boldsymbol{v}_\mathrm{pec}(\boldsymbol{x}_i)/c \cdot \boldsymbol{n}_i\right)\right)\right|^2}{\sigma_\mu^2} w_i^2. \tag{5.26}$$

Varying the redshift of such a hypothetical concentration along the direction $(l_\mathrm{SSC}, b_\mathrm{SSC})$ towards the SSC and minimizing the expression in equation (5.26) yields the corresponding overdensity at a redshift z, i.e. $\delta = \delta(z, l_\mathrm{SSC}, b_\mathrm{SSC})$, necessary to account for the peculiar motions (see equation 5.23) present in the data.

5.4 Peculiar Velocity Tidal Field

The natural extension of the dipole fit (section 5.1) is a quadrupole term that probes the anisotropy on a smaller scale. A common parameterization of this is the *peculiar velocity tidal field* (see e.g. Lynden-Bell et al. 1988; Kaiser 1991; Hoffman et al. 2001):

$$\boldsymbol{v}(\boldsymbol{x}) = \boldsymbol{v}_\mathrm{d} + (\tilde{H} + \Sigma) \cdot \boldsymbol{x}, \tag{5.27}$$

where $\boldsymbol{v}_\mathrm{d}$ is a constant dipole vector as before, $\tilde{H}$ is a scalar (corresponding to a monopole) and Σ is a traceless, symmetric tensor (the quadrupole or shear). A monopole term would be a locally isotropic perturbation of the Hubble constant and is expected to vanish for a large observed volume. The shear tensor is defined as traceless and symmetric because the trace is degenerate to the monopole and the velocity field is assumed to be irrotational (it is defined by an equation for its divergence). This definition of a quadrupole differs to that found in some analyses (e.g. Haugbølle et al. 2007), which only assume the velocity to change with the direction but not with distance. Indeed the absolute value of the quadrupole term above will grow linearly with distance to the observer. Therefore, this model is not a good description for anisotropies at high redshift. However, in a more local study, like the search for an attractor as in the previous section, it is very useful. The model is called tidal field because it describes the effect of an attractor outside the observed volume and thus meaningful results can only be obtained when restricting the data to a local volume. This interpretation as the effect of an outside attractor can be understood by calculating the Taylor expansion of the velocity field of the attractor (Hoffman et al., 2001).

The velocity field created by a spherical overdensity of a given mass M_att takes the same shape outside of the attractor regardless of its radius. Using Cartesian coordinates, the field of an attractor located at distance r_att on the x-axis is described as

$$\boldsymbol{v}(\boldsymbol{x}) = \frac{-v_0 r_\mathrm{att}^2}{\sqrt{(x - r_\mathrm{att})^2 + y^2 + z^2}^3} \begin{pmatrix} x - r_\mathrm{att} \\ y \\ z \end{pmatrix}, \tag{5.28}$$

where the normalization v_0 can be expressed in terms of the density contrast using equation (5.23):

$$v_0 = \frac{\Omega_\mathrm{m}^{0.55} H_0 \delta_0}{3(1+z)} \frac{R_\mathrm{att}^3}{r_\mathrm{att}^2}. \tag{5.29}$$

Expanding equation (5.28) to first order yields:

$$\boldsymbol{v}(\boldsymbol{x}) = \begin{pmatrix} v_0 \\ 0 \\ 0 \end{pmatrix} + \frac{v_0}{r_\mathrm{att}} \begin{pmatrix} 2 & 0 & 0 \\ 0 & -1 & 0 \\ 0 & 0 & -1 \end{pmatrix} \cdot \boldsymbol{x}. \tag{5.30}$$

From this one can see that v_0 can be determined from the dipole while the shear also depends on the distance to the attractor; the larger the distance, the smaller the shear. As pointed out by Kaiser (1991), this relation can then be used to constrain the distance to the attractor as

$$r_\mathrm{att} = \frac{2\,|\boldsymbol{v}_d|^3}{\boldsymbol{v}_d^T \cdot \Sigma \cdot \boldsymbol{v}_d}, \tag{5.31}$$

i.e. by dividing the bulk flow by the shear component in bulk flow direction. Furthermore, predictions can be made for the eigenvectors and eigenvalues of the shear tensor based on equation (5.30). The eigenvector for the largest eigenvalue λ_1 is expected to be aligned with the bulk flow and the other eigenvalues are expected to be negative $\lambda_2 = \lambda_3 = -\lambda_1/2$. However, since the relation $\lambda_1 + \lambda_2 + \lambda_3 = 0$ follows directly from Σ being traceless, the relation between the eigenvalues follows trivially from the symmetry of the assumed model and is thus true for similar models. If the bulk flow is not caused by a single attractor but by several mass concentrations located in the same direction, this can be approximated by a power law with an exponent other than -2 (Kaiser, 1991):

$$\boldsymbol{v}(\boldsymbol{x}) = \frac{-v_0 r_\mathrm{att}^\gamma}{\sqrt{(x-r_\mathrm{att})^2 + y^2 + z^2}^{\,\gamma+1}} \begin{pmatrix} x - r_\mathrm{att} \\ y \\ z \end{pmatrix}, \tag{5.32}$$

which has the Taylor expansion

$$\boldsymbol{v}(\boldsymbol{x}) = \begin{pmatrix} v_0 \\ 0 \\ 0 \end{pmatrix} + \frac{v_0}{r_\mathrm{att}} \frac{(\gamma-2)}{3} \boldsymbol{x} + \frac{v_0}{r_\mathrm{att}} \begin{pmatrix} \frac{2(\gamma+1)}{3} & 0 & 0 \\ 0 & -\frac{\gamma+1}{3} & 0 \\ 0 & 0 & -\frac{\gamma+1}{3} \end{pmatrix} \cdot \boldsymbol{x}. \tag{5.33}$$

Based on this the characteristic distance can still be estimated by equation (5.31) but must by multiplied by $3/(\gamma+1)$. The exponent γ in turn can be determined from the monopole term that appears for $\gamma \neq -2$, so measuring the monopole may be important to correct this distance estimate properly.

Therefore, the measurement of the shear offers a constraint on the characteristic distance to the attractor when combined with the bulk flow. Compared to the attractor model of the previous section, this approach has the advantage of being model-independent while still enabling us to narrow down the location of the attractor. However, as it requires the inference of nine model parameters instead of one, the results will be much less significant for the current data. Thus, instead of optimizing this model for the available dataset, it was investigated in simulations of future surveys, see chapter 8.

CHAPTER 6

Dipole Anisotropy

The first two methods discussed in the previous chapter are both designed to be sensitive to a dipole anisotropy. Therefore their results are summarized in this chapter, whereas the gravitational attractor results are the discussed in the next.

Since both analysis methods are sensitive to the same kind of signal (dipole), the results will be presented for both methods sorted by redshift shell. This is then followed by a discussion of systematic effects and a comparison of the randomization methods. Part of the results presented in this chapter have been published in Feindt et al. (2013). Most of the analysis has been re-implemented, especially the smoothed residuals, which are now fully maximized and not only evaluated on a grid. The p-values for the dipole fit results were corrected as described in the recently published corrigendum (Feindt et al., 2015).

6.1 Results

The analyses were first performed for each individual dataset, Union2 and SNfactory, and then for the combined data. Both methods had a common first step, in which the cosmological parameters are determined for the whole dataset in a Hubble fit assuming a flat ΛCDM universe. The only parameters in this fit were the matter density parameter Ω_m and the absolute magnitude M of SNe Ia; the Hubble constant H_0 was fixed at $H_0 = 70\,\mathrm{km\,s^{-1}\,Mpc^{-1}}$ because it is degenerate to M. The SNfactory dataset only covers the low redshift range and thus cannot constrain Ω_m by itself. Therefore, the density was fixed to $\Omega_\mathrm{m} = 0.28$ when using only SNfactory data. For the combined dataset an additional offset between the absolute magnitudes for each dataset was included as a fit parameter, to account for possible differences in the standardization (see section 4.4.4).

In the next step, the data is split into several redshift shells to determine the evolution of the anisotropy with distance. As described in section 4.4, the choice of redshift shells was based on Colin et al. (2011) and is in part motivated by studying a possible backside infall for SNe behind the SSC. In particular the boundary between the second an third shell at $z = 0.045$ corresponds to the approximate distance to the centre of the SSC. The analysis in those redshift shells could therefore detect a backside infall into the SSC as a reversal in the dipole direction.

The results of the dipole fit for each dataset in the redshift shells are listed in table 6.1, showing both Galactic spherical coordinates and Cartesian coordinates. The axes of the Cartesian coordinate system were chosen such that the x-axis points towards ($l = 0°, b = 0°$), i.e. towards the Galactic centre, while

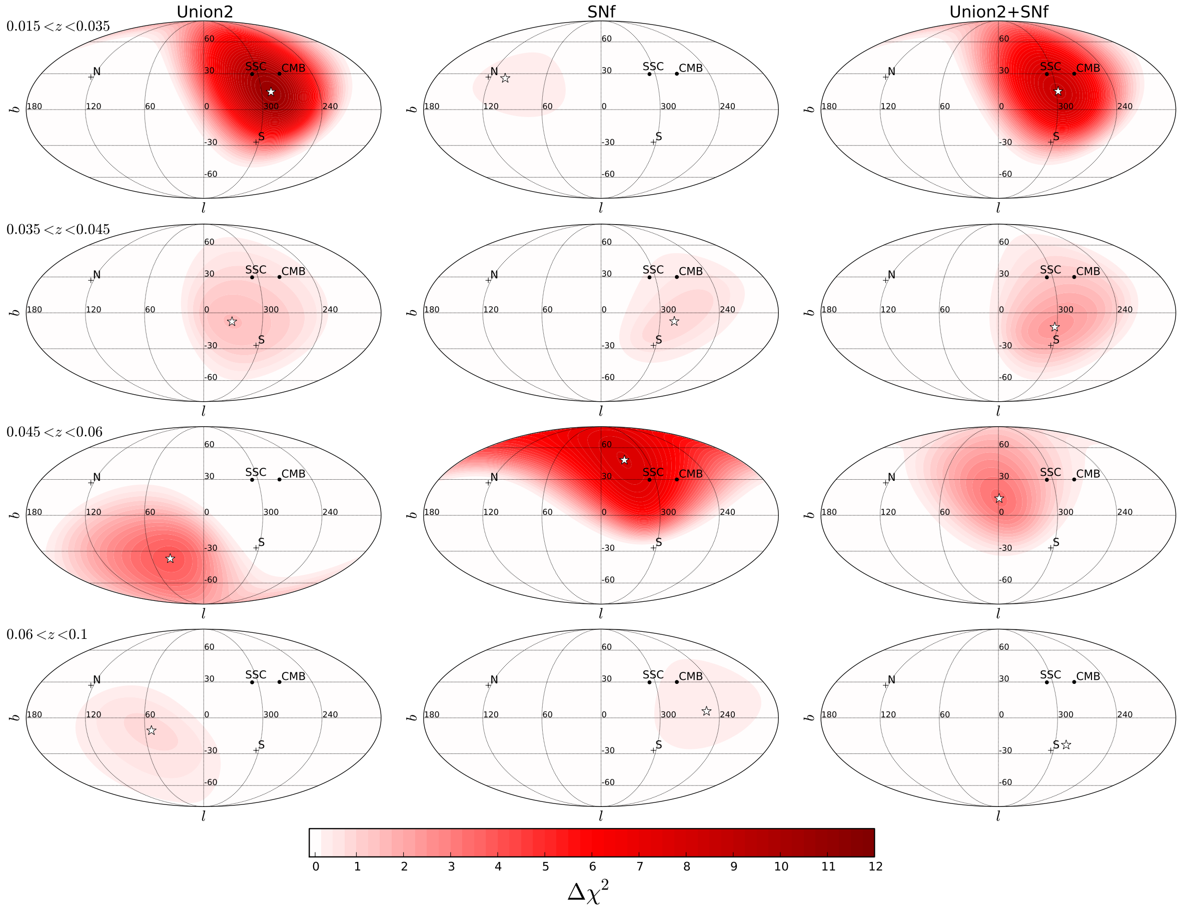

Figure 6.1: Variation of χ^2 for a dipole fit of low-redshift SNe Ia from Union2 (left column), SNFACTORY (centre column) and their combination (right column) datasets as a function of Galactic coordinates (l, b) in the redshift bins $0.015 < z < 0.035$ (first row), $0.035 < z < 0.045$ (second row), $0.045 < z < 0.06$ (third row) and $0.06 < z < 0.1$ (fourth row). The best fit direction is marked by a star at minimum χ^2.

the y-axis points towards a location on the Galactic plane, 90° east of the centre ($l = 90°, b = 0°$) and the z-axis corresponds to the rotation axis of the Galaxy, i.e. ($l = 0°, b = 90°$). The right-most column of the table lists the p-values calculated using the two methods described in section 5.1, for which the data in each shell was randomized 250 000 times. Such a large number of realizations was needed to average out random fluctuations for very small p-values. For most redshift shells the p-values agree well but a few cases show differences. The methods will be compared in greater detail in section 6.3. Figure 6.1 shows the variation of the χ^2-value for the low-redshift SNe ($0.015 < z < 0.1$) of the two datasets and their combination as determined by minimizing equation (5.4) for a fixed direction on the sky. The colourmap corresponds to the decrease of χ^2 for a dipole in a given direction to the value for no dipole:

$$\Delta\chi^2 = \chi^2_{\text{no dipole}} - \chi^2_{\text{dipole}}. \tag{6.1}$$

This value can also be interpreted as a significance based in the χ^2-distribution function defined in equation (5.10) using $k = 3$ for three degrees of freedom (the Cartesian components of the dipole velocity).

		Galactic coordinates			**Cartesian coordinates**				
N_{SN}	z	l [°]	b [°]	$\lvert v_{\mathrm{d}}\rvert$ [km s^{-1}]	v_x [km s^{-1}]	v_y [km s^{-1}]	v_z [km s^{-1}]	p_A	p_B
Union2									
109	0.015-0.035	290(22)	15(18)	292(96)	98(100)	−265(111)	73(85)	0.015	0.011
16	0.035-0.045	331(59)	−7(37)	496(468)	431(567)	−239(386)	−63(331)	0.732	0.672
17	0.045-0.06	39(45)	−36(28)	870(490)	547(628)	438(439)	−516(365)	0.154	0.261
23	0.06-0.1	54(93)	−10(53)	509(601)	294(766)	406(674)	−92(442)	0.783	0.837
55	0.1-0.2	256(90)	−18(34)	1238(1976)	−294(1430)	−1139(2059)	−387(1267)	0.388	0.437
62	0.2-0.3	14(131)	11(75)	1221(1458)	1167(2038)	282(2433)	226(1449)	0.644	0.776
62	0.3-0.4	257(84)	−36(27)	2590(2841)	−478(2668)	−2028(2974)	−1538(1693)	0.349	0.605
58	0.4-0.5	161(48)	28(29)	4190(4014)	−3482(3824)	1204(3415)	1995(1924)	0.711	0.671
44	0.5-0.6	15(100)	−17(33)	3977(4113)	3690(4333)	955(6367)	−1133(2638)	0.715	0.807
50	0.6-0.8	343(81)	−50(43)	5576(4279)	3460(5021)	−1066(5548)	−4241(2485)	0.313	0.354
60	0.8-1.4	75(55)	−14(28)	7238(8933)	1845(6675)	6789(8713)	−1700(4305)	0.860	0.864
SNFACTORY									
20	0.015-0.035	104(95)	26(44)	229(410)	−50(387)	200(319)	101(253)	0.896	0.928
20	0.035-0.045	286(70)	−7(42)	484(516)	128(613)	−463(469)	−59(380)	0.861	0.780
21	0.045-0.06	330(48)	48(46)	941(390)	548(618)	−319(656)	695(451)	0.016	0.040
54	0.06-0.1	252(134)	5(75)	232(360)	−72(514)	−219(402)	22(296)	0.909	0.912
Union2+SNFACTORY									
128*	0.015-0.035	298(25)	15(20)	243(88)	110(95)	−207(102)	64(79)	0.027	0.030
36	0.035-0.045	302(48)	−12(26)	452(314)	235(379)	−375(282)	−92(232)	0.560	0.483
38	0.045-0.06	359(32)	14(27)	650(398)	631(423)	−6(355)	157(273)	0.244	0.326
77	0.06-0.1	285(234)	−23(112)	105(401)	25(426)	−93(343)	−41(244)	0.991	0.993

Table 6.1: Reconstructed velocities (in Galactic and Cartesian coordinates) as p-values according to a dipole fit in different redshift bins for the *Union2* and SNFACTORY datasets and their combination. Note: Cartesian coordinates were chosen such that the x-axis points towards ($l = 0°, b = 0°$), the y-axis towards ($l = 90°, b = 0°$) and the z-axis towards ($l = 0°, b = 90°$). *SN 2005eu (= SNF20051003-004) is included in both datasets. The Union2 measurement was used for the combined datasets.

The methods of smoothed residuals described in section 5.2 were then used as a more generic test for anisotropy. For this the data were again split into redshift shells. The results of this analysis are listed in table 6.2 and shown in figures 6.2 and 6.3. Unlike the dipole fit where the $\Delta\chi^2$-values can be interpreted in a similar fashion for all shells, the distribution of the ΔQ-value for the smoothed residuals cannot be predicted analytically. Therefore the plotted values were scaled to allow use of a common colourmap. The scale is defined by the maximum of the absolute smoothed residual values in each redshift shell. The colours distinguish the sign of the smoothed residuals and were chosen to reflect the peculiar velocity interpretation of the values, i.e. positive values (blue) correspond to a motion towards us while negative values (red) indicate a motion away from us. This information is important since some shells have only positive or negative smoothed residuals on the whole sky, which indicates a possible monopole term in addition to the dipole.

The results for the smoothed residual mostly agree with those of the dipole fit but there are shells, in which they disagree. Since this method was adapted from Colin et al. (2011) and modified by a normalization (dividing by the sum of the Gaussian weights) here, both methods were used to find the direction of maximum anisotropy, allowing a comparison of the methods. The directions of the minimum smoothed residual values, which correspond to the bulk flow direction, are consistent for both methods in shells with significant results but can differ greatly if the shell is dominated by noise. In general, the normalized smoothed residuals appear to vary on smaller angular scales and the original method is more similar to the dipole that one expects for a smoothing angle of 90°. Accordingly the angular separations between the directions of the maximum and minimum values of the test statistic are closer to 180° for the non-normalized smoothed residuals while they can be as small as 90° for the normalized method. Neither method shows a clear trend towards smaller p-values than the other, since the sensitivity of each methods fluctuates with the distribution of the data. This has also been pointed out by Appleby & Shafieloo (2014) based on simulations for both methods.

The results for each redshift shell are discussed in detail in the following paragraphs.

$0.015 < z < 0.035$ In the nearest redshift shell the SNfactory dataset has only low statistics because higher redshifts were targeted in the survey. Thus, the constraints here are dominated by data from the Union2 SN compilation, which shows a significant bulk flow ($p_A = 0.015, p_B = 0.011$) with a velocity of $v_\mathrm{d} = 292 \pm 96\,\mathrm{km\,s^{-1}}$ towards ($l = 290° \pm 22°, b = 15° \pm 18°$). The combined data show a slightly higher p-value of 0.030 than the Union2 dataset alone for $0.015 < z < 0.035$. While the direction of the bulk flow barely changes, the velocity is slightly lower at $v_\mathrm{d} = 243 \pm 88\,\mathrm{km\,s^{-1}}$ for the combined dataset. The direction of the bulk flow is compatible both with the SSC ($l = 306.44°$, $b = 29.71°$) and the CMB dipole ($l = 276° \pm 3°$, $b = 30° \pm 3°$). The bulk flow found in this shell is also consistent with those results of previous studies listed in table 3.1 that found bulk flows of $\sim 250\,\mathrm{km\,s^{-1}}$, which are compatible with the ΛCDM expectation on this scale. Note, however, that many SNe in the Union2 sample were used in several other studies as well.

The smoothed residual method finds similar results; the direction of the minimum value for the Union2 dataset is ($l = 295°, b = 32°$) for both test statistics. All methods to determine the significance agree with each other as well, finding values between 0.018 and 0.025, which is slightly larger than the results for the dipole fit. As mentioned above the directions of the maximum values are not necessarily exactly opposite of the minimum. In this shell, the distribution is symmetric for the non-normalized method but for the normalized smoothed residuals the directions minimum and maximum are separated by 152°. As for the dipole fit, the results in the first shell of the SNfactory dataset are completely insignificant with p-values larger than 0.85.

		normalized						**non-normalized**					
		minimum		maximum				minimum		maximum			
N_{SN}	z	$l\,[°]$	$b\,[°]$	$l\,[°]$	$b\,[°]$	p_A	p_B	$l\,[°]$	$b\,[°]$	$l\,[°]$	$b\,[°]$	p_A	p_B
Union2													
109	0.015-0.035	295	32	99	−58	0.023	0.021	295	32	117	−31	0.025	0.018
16	0.035-0.045	309	13	126	−24	0.245	0.216	304	24	126	−26	0.331	0.296
17	0.045-0.06	60	−29	240	55	0.243	0.371	71	−53	244	55	0.121	0.176
23	0.06-0.1	67	−25	250	41	0.744	0.781	69	−42	248	38	0.670	0.731
55	0.1-0.2	239	40	34	13	0.484	0.459	219	−4	38	7	0.560	0.635
62	0.2-0.3	358	56	227	24	0.393	0.379	24	38	201	−29	0.372	0.614
62	0.3-0.4	155	−80	320	64	0.132	0.205	217	−86	316	82	0.701	0.742
58	0.4-0.5	219	61	20	−51	0.334	0.378	277	75	49	−76	0.334	0.347
44	0.5-0.6	15	13	202	6	0.428	0.353	14	14	193	−15	0.272	0.223
50	0.6-0.8	26	−74	297	77	0.067	0.068	46	−78	248	78	0.068	0.077
60	0.8-1.4	356	−39	220	52	0.989	0.987	90	13	266	−22	0.990	0.989
SNFACTORY													
20	0.015-0.035	326	46	215	−43	0.891	0.932	67	6	245	−10	0.867	0.883
20	0.035-0.045	268	22	96	−16	0.585	0.507	273	16	102	−16	0.886	0.834
21	0.045-0.06	311	60	167	−60	0.003	0.009	327	60	140	−63	0.002	0.007
54	0.06-0.1	268	32	24	−64	0.939	0.953	268	32	81	−41	0.775	0.803
Union2+SNFACTORY													
128*	0.015-0.035	304	28	113	−51	0.062	0.065	301	32	121	−33	0.049	0.052
36	0.035-0.045	292	16	116	−21	0.186	0.160	295	21	119	−24	0.369	0.314
38	0.045-0.06	336	57	180	−47	0.108	0.151	347	48	174	−51	0.182	0.281
77	0.06-0.1	248	−88	249	63	0.999	0.999	271	29	99	−27	0.990	0.994

Table 6.2: Reconstructed directions (in Galactic coordinates) for the minimum and maximum values of the smoothed residual statistics and p-values in different redshift bins for the *Union2* and SNFACTORY datasets and their combination. Note: *SN 2005eu (= SNF20051003-004) is included in both datasets. The Union2 measurement was used for the combined datasets.

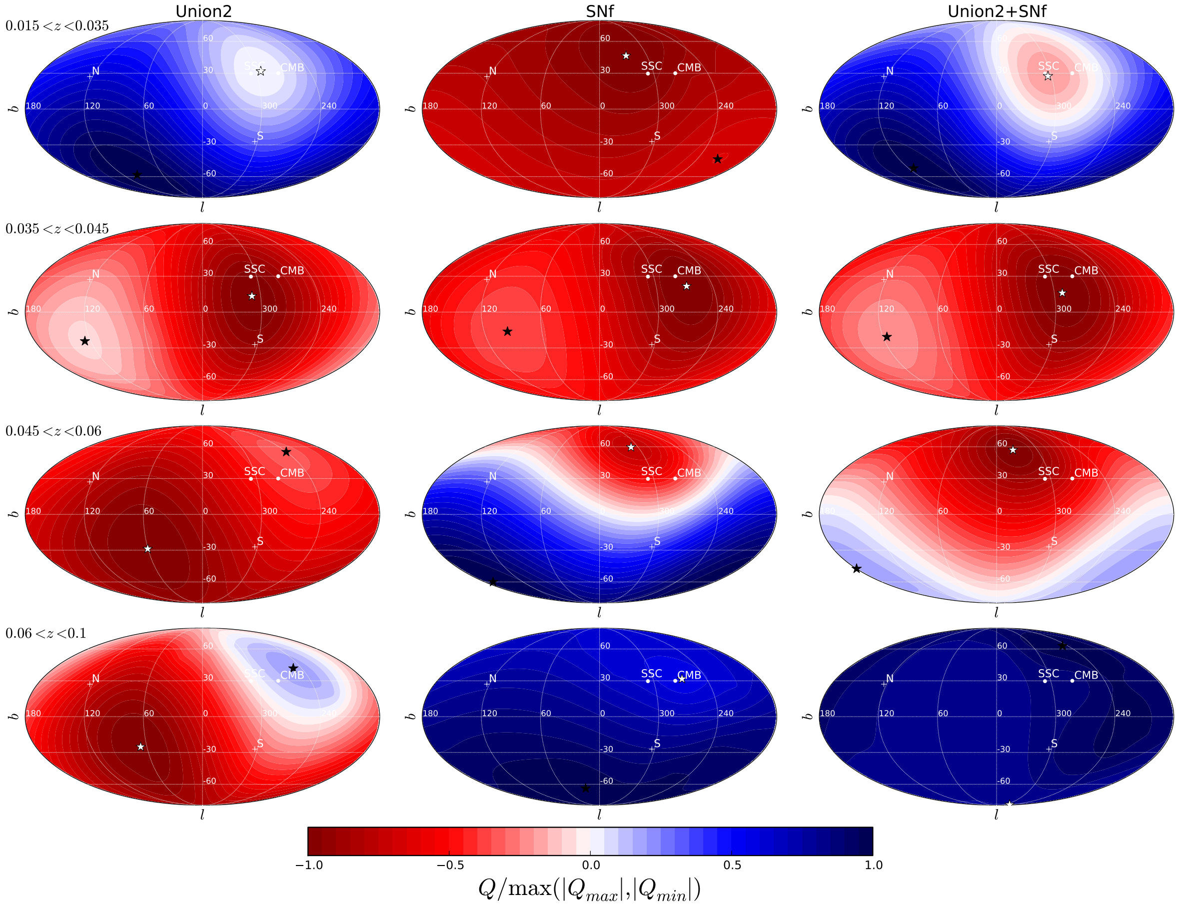

Figure 6.2: Magnitude residuals of low-redshift SNe Ia as a function of galactic coordinates (l, b) after smoothing with a Gaussian window function of width $\delta = 90°$ normalized by the sum of the Gaussians (columns and rows as in figure 6.1). The Q-values are scaled by $\max(|Q_{max}|, |Q_{min}|)$ to make the results more comparable and show bins with mostly positive or negative values. The colours correspond to a velocity interpretation of the anisotropy, using red and blue for a motion away from and towards the observer, respectively. The minimum and maximum values of the smoothed residual statistic are marked by a white and black star, respectively.

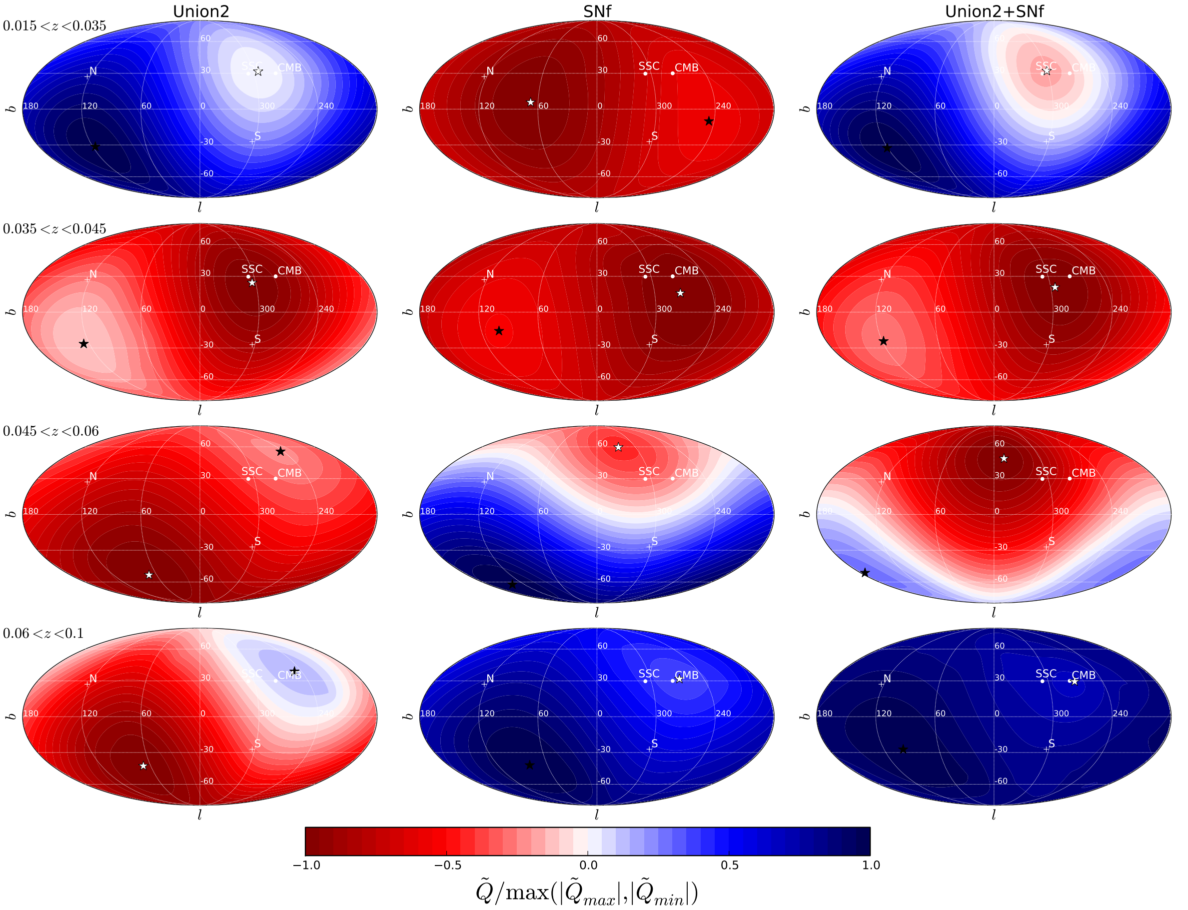

Figure 6.3: Magnitude residuals of low-redshift SNe Ia as a function of galactic coordinates (l, b) after smoothing with a Gaussian window function of width $\delta = 90°$ without normalization by the sum of the Gaussians (columns, rows, colourmap and marks as in figure 6.1).

There is some tension between the two SN datasets: While insignificant ($p_A = 0.896, p_B = 0.928$), the bulk flow obtained from the SNFACTORY data points towards a direction ~ 140° away from that found for Union2. A similar tension is observed for the non-normalized smoothed residuals (~ 120°) but not for the normalized ones (~ 28°). This is solely due to the different ($l_{\mathrm{min}}, b_{\mathrm{min}}$) found for the SNFACTORY data; the directions for the Union2 data agree completely. However, the consistency of the measured bulk flows from the dipole fit should still be investigated to assess whether the samples should be combined in the first place. The method for this consistency check is given by equation (5.9) at the end of section 5.1. For this redshift shell we find $\Delta^2 = 2.62$ which corresponds to a probability of 0.455 that the disagreement is random, verifying that the observed tension is not significant.

$0.035 < z < 0.045$ In the next redshift shell the data from SNFACTORY starts to dominate the available SN statistics. However, even the combined dataset does not show a significant bulk flow in the dipole fit ($p_A = 0.560, p_B = 0.483$). For the smoothed residuals the p-values are considerably lower but not significant, either, and the normalized method gives consistently lower p-values than the non-normalized one for all datasets. For the combined data, they are $p_A = 0.186$, $p_B = 0.160$ (normalized) and $p_A = 0.369$, $p_B = 0.314$ (non-normalized).

The reason for this difference to the dipole fit is that there are mostly negative residuals in this shell. Therefore the values of the smoothed residual statistics are negative on the whole sky. In terms of the dipole fit this means that there are SNe with large positive peculiar velocities but none with large negative velocities (see also figure 4.7). The dipole model will only fit well if there are similarly large values on opposite sides of the sky. A sample that only has large values in one direction but mostly noise in the opposite direction will therefore show a larger anisotropy when analysed using the more generic smoothed residuals method. If the dipole fit is extended by an isotropic monopole velocity, this case can be observed as a non-zero monopole (see section 6.2). The effect of this monopole term will also be investigated in section 6.3.

The large p-values in this shell are mostly due to the choice of redshift shells, which led to a relatively small sample in this shell. Recall that, as described above, the first shell ($0.015 < z < 0.035$) was chosen to be comparable with previous velocity studies and the upper boundary of this shell ($z = 0.045$) was chosen such that it intersects the centre of the SSC, whose influence on the bulk flow is of interest to this studied. Therefore, it was necessary to separate the data in front of and behind it for this part of the analysis. A model that makes better use of the data in this shell is the attractor model used in chapter 7.

$0.045 < z < 0.06$ The third redshift bin ($0.045 < z < 0.06$) intersects the SSC at the lower redshift boundary. Hence, if the missing component of the LG velocity is due to the infall into the SSC, one would expect the dipole to reverse its direction in the hemisphere around the SSC while it remains the same in the other hemisphere. This would then be detectable as a bulk flow pointing roughly in a direction opposite to that found in lower redshift shells. For the Union2 data, the direction of anisotropy appears to be reversed in such a fashion, pointing towards $l = 39° \pm 45°$, $b = -36° \pm 28°$, whereas the amplitude of the velocity $v_{\mathrm{d}} = 870 \pm 490\,\mathrm{km\,s^{-1}}$ is rather large but also has a large uncertainty. This is in agreement with the turnover seen by Colin et al. (2011) using the same data. However, with p-values of $p_A = 0.154$ and $p_B = 0.261$ the reversal is not significant. The smoothed residual method shows the same apparent reversal, though there is a slight difference between the two versions of the method. For the non-normalized method the p-values are slightly smaller than for the dipole fit but the normalized version they are larger. Similarly the normalized smoothed residuals does not point to a direction as far away from the SSC as the non-normalized ones do, though this change is small since the direction from the normalized method is only 11° closer to the SSC. This effect is in part by design. Recall that the normalization was introduced the effect of oversampled region.

The SNFACTORY data do not support this tentative reversal of the dipole. Rather, the bulk flow in the corresponding shell maintains its global direction with $l = 330° \pm 48°$, $b = 48° \pm 46°$ with a small p-values ($p_A = 0.016, p_B = 0.04$). Both smoothed residual methods show the same anisotropy with even higher significances. The best fit bulk flow velocity $v_\mathrm{d} = 941 \pm 390\,\mathrm{km\,s^{-1}}$ appears to be large, but due to its uncertainty not completely inconsistent with the values at lower redshifts. Furthermore, the p-values for the dipole fit disagree by a factor of 2.5 between the two randomization methods, with test B (using random Gaussian noise) giving a larger value than test A (shuffling the residuals). This seems to be caused by the fact that most residuals in this shell of the SNFACTORY data are fairly large.

When combining the SNFACTORY and Union2 datasets, this bulk flow beyond the SSC seen in the SNFACTORY data is not significant any longer, but still no turnover can be observed: the bulk flow is shifted slightly away from the SSC, pointing towards $l = 359° \pm 32°$, $b = 14° \pm 27°$ with a lower velocity of $v_\mathrm{d} = 650 \pm 398\,\mathrm{km\,s^{-1}}$.

As for the first redshift shell, there is some tension between the datasets in this shell. In this case it is more significant with $\Delta^2 = 8.59$, corresponding to a probability $p = 0.035$ that the tension occurred by chance. Due to the significance of this redshift shell for the study of the SSC, it is important to understand the source of this disagreement between the Union2 and SNFACTORY data in the $0.045 < z < 0.06$ shell. Recall the underlying distribution of SN peculiar velocities on the sky from the Hubble fit was shown in figure 4.7, with the size of the markers correlating to the amplitude of the velocity and colour and shape corresponding to the direction. When looking at the Union2 data for redshifts $0.045 < z < 0.06$ (third plot in the left column) it becomes clear that the putative turnover in flow direction is not exclusively induced by SNe falling into the SSC but also driven by two distant SNe in the direction opposite the SSC, SN 1995ac (Riess et al., 1999) and SN 2003ic[1] (Hicken et al., 2009a). In this shell SNe in the vicinity of the SSC should otherwise be significantly blueshifted giving positive residuals, however Union2 only contains a single slightly blueshifted SN there. Therefore the Union2 compilation has insufficient area coverage in this critical redshift shell to address the question of whether the SSC is the source of the CMB-dipole. For the SNFACTORY sample, on the other hand, there are two redshifted SNe that show large residuals ($\sim 1.5\sigma$) behind the SSC while SNe in the opposite part of the sky are mostly blueshifted.

For the dipole fit, the effect of removing SNe from the sample was thoroughly tested by jackknifing the dataset, i.e. removing SNe and re-performing the analysis. Removing either or both of the two Union2 SNe in question (1995ac and 2003ic) stands out as decreasing the tension significantly more than any other SNe. When one of them is removed at a time, the tension decreases to Δ^2-values of 6.37 ($p = 0.095$) and 6.32 ($p = 0.097$) respectively. Removing any other SN, will decrease the tension to 7.21 ($p = 0.067$) at best. Similarly, removing both SNe decreases the tension to $\Delta^2 = 4.15, p = 0.246$, whereas removing any pair of SNe that does not include SNe1995ac and 2003ic will only decrease the tension to 5.98 ($p = 0.113$) at best. It is therefore reasonable to assume that the two SNe in question are the main cause of the apparent reversal of the anisotropy in the Union2 dataset and the tension with the SNFACTORY data.

Without SNe 1995ac and 2003ic the amplitude of v_d determined from Union2 (cf. table 6.1) alone decreases to $498 \pm 573\,\mathrm{km\,s^{-1}}$ while its direction shifts to $l = 35° \pm 66°, b = -20° \pm 46°$. The effect of removing both SNe on the combined dataset is insignificant as we find $v_\mathrm{d} = 629 \pm 336\,\mathrm{km\,s^{-1}}$ towards

---

[1] This SN has been previously identified as an outlier in the host-luminosity relation (Kelly et al., 2010). Furthermore, as shown in section 4.4.3, it is located in the galaxy cluster Abell 0085. The difference in redshifts is insignificant ($\Delta z = 0.00007$).

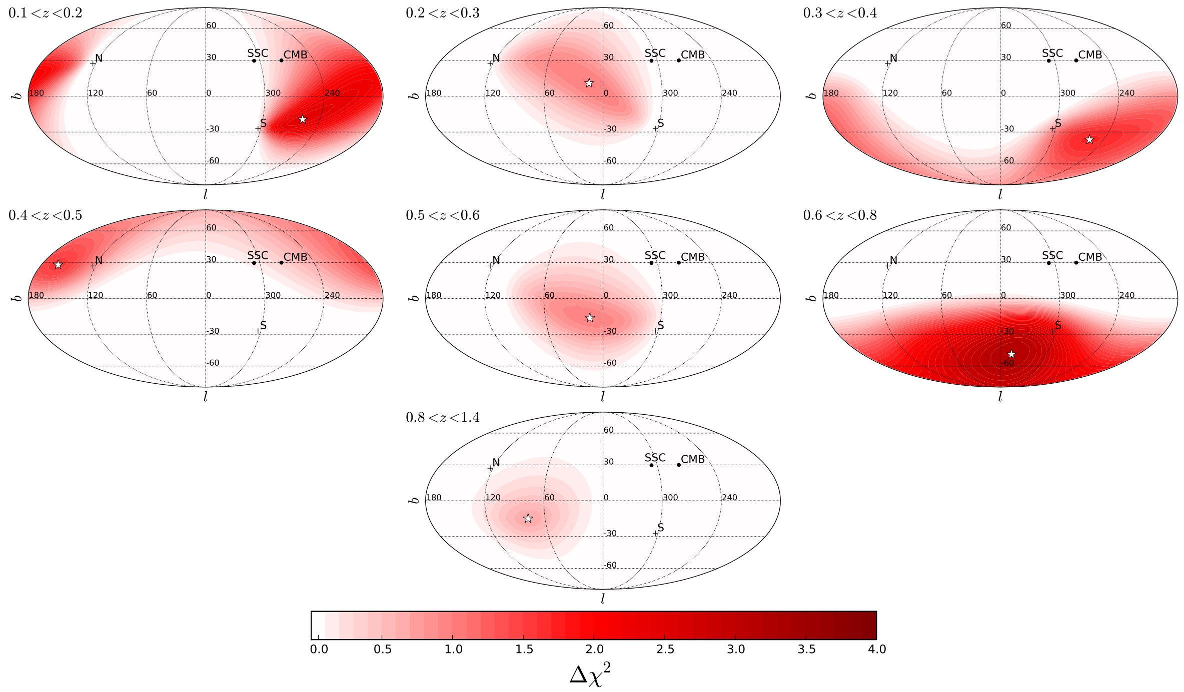

Figure 6.4: Variation of χ^2 for a dipole fit of high-redshift SNe Ia from Union2 for the redshift bins for $z > 0.1$. Note that the scaling of the colourmap differs to that in 6.1 and the results in these bin are generally less significant.

$l = 351° \pm 40°, b = 37° \pm 37°$. Furthermore, note that the probability of finding a p-value of less than 0.035 for at least one of four measurements is 13.3% and hence finding this tension in one of four redshift shells is not as significant as it may seem by itself.

$0.06 < z < 0.1$ Finally, for the $0.06 < z < 0.1$ shell, no bulk motion is detected for any of the samples — the best fit velocity is consistent with zero with an associated uncertainty of $\sim 400\,\mathrm{km\,s^{-1}}$ and both p-values are > 0.99 for all three methods. Note that the bulk flow uncertainties in Galactic coordinates may seem contradictory at first glance because they increase for the combined dataset if compared to the individual datasets. This is due to the fact that the dipole velocities for the individual datasets point in different directions[2] and therefore the best-fit velocity amplitude for the combined data is closer to zero. In spherical coordinates a velocity amplitude consistent with zero will lead to large uncertainties in the direction. The Cartesian components of the velocity, on the other hand, have smaller uncertainties for the combined dataset as one would expect.

The result in this shell contradicts the results of Kashlinsky et al. (2010) who measured bulk flows of $\sim 1000\,\mathrm{km\,s^{-1}}$ aligned with the CMB dipole direction at similar distances. In their lowest redshift sample ($z < 0.12$ with z_{median} between 0.06 and 0.086 depending on the X-ray luminosity bin used), they found a velocity of $934 \pm 352\,\mathrm{km\,s^{-1}}$ in the direction ($l = 282° \pm 34°, b = 22° \pm 20°$), less than 10° off the CMB dipole direction. For a better comparison to their results, the fit was repeated for the absolute value of the dipole velocity alone while keeping its direction fixed at the one found by Kashlinsky et al.. This yields a velocity of $34 \pm 254\,\mathrm{km\,s^{-1}}$, i.e a bulk flow of $\sim 1000\,\mathrm{km\,s^{-1}}$ in that direction is ruled out at almost 4σ.

---

[2] There is no significant tension in this case. The uncertainties are too large.

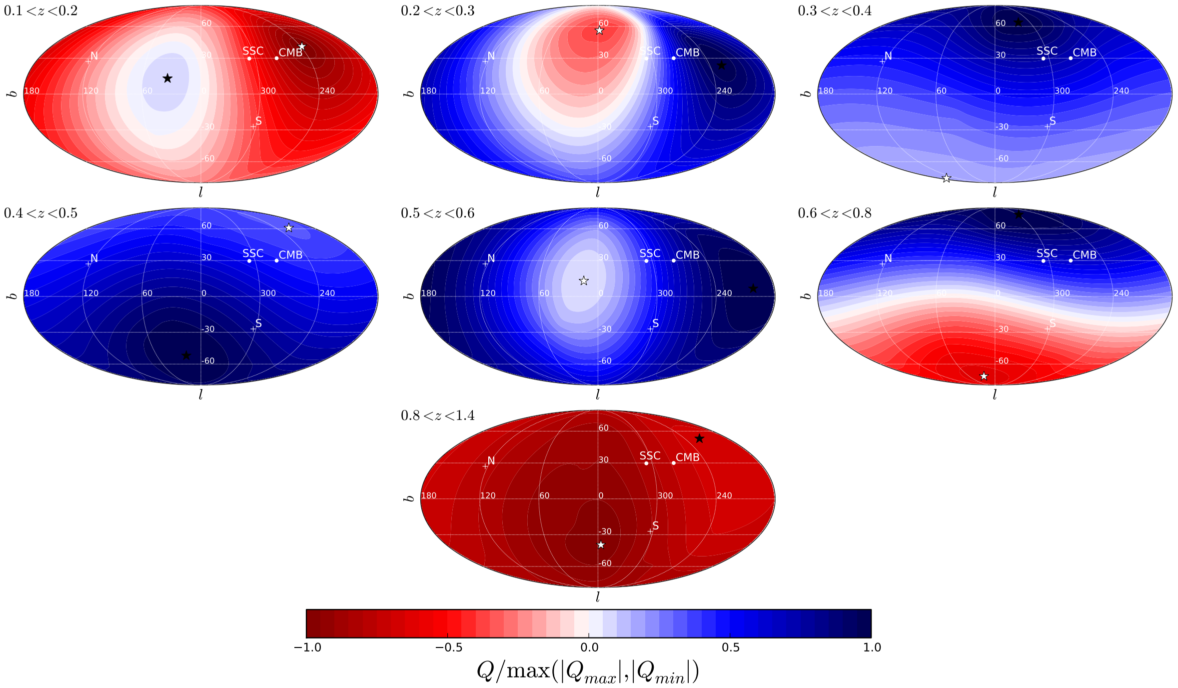

Figure 6.5: Magnitude residuals of high-redshift SNe Ia as a function of galactic coordinates (l, b) after smoothing with a Gaussian window function of width $\delta = 90°$ normalized by the sum of the Gaussians (columns, rows, colourmap and marks as in figure 6.1).

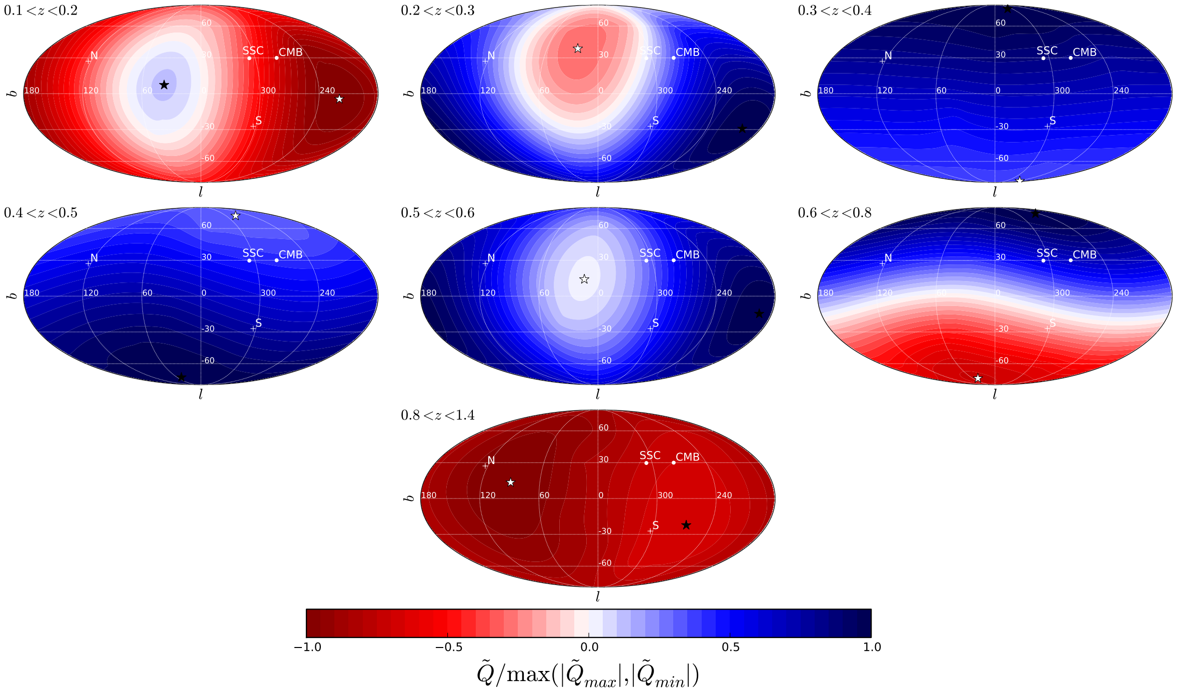

Figure 6.6: Magnitude residuals of high-redshift SNe Ia as a function of galactic coordinates (l, b) after smoothing with a Gaussian window function of width $\delta = 90°$ without normalization by the sum of the Gaussians (columns, rows, colourmap and marks as in figure 6.1).

$z > 0.1$ Figures 6.4 – 6.6 show the same results as the previous three figure for the SNe of the Union2 compilation with redshifts $z > 0.1$.

In the higher-redshift shells, no significant dipole anisotropies are observed. The p-values for nearly all shells at redshift $z > 0.1$ are larger than $p = 0.3$, i.e. the significances are at a 1σ-level at best, for all methods. There are some exceptions, most notably in the shell at $0.6 < z < 0.8$, for which the both smoothed residuals find p-values around 0.07, which is still not a 2σ significance. However, given the uneven distribution of the data on the sky at high redshifts and the fact that the dipole fit is not significant there, it is more likely that this is just an artefact of the method and not a real anisotropy. It is furthermore worth noting, the best-fit amplitudes of the dipole velocity become increasingly large with distance but their uncertainties grow by the same factor. These large amplitudes are purely due to the fact that peculiar velocities have only a small relative effect on the luminosity distances at larger distances, and not due to large amplitude flows. The data are instead mostly affected by measurement errors and other effects such as gravitational lensing.[3]

6.2 Systematic Uncertainties

Systematic uncertainties associated with SNe Ia as distance indicators have been scrutinized carefully for the measurement of the expansion history of the Universe. Some of the main sources of redshift- or sample-dependent systematic error are connected to flux zero points, K-corrections and Malmquist bias (Amanullah et al., 2010; Regnault et al., 2009). They can also conspire in non-trivial ways, such as in the case of the "Hubble bubble" (Jha et al., 2007), an apparent 6% increase of the local Hubble parameter in a region out to $z \sim 0.25$. The Hubble bubble was explained in Conley et al. (2007) as the result of a combination of a bias in colour, i.e. the closest SNe in the sample show more reddening, and the choice of the reddening correction parameter β. Another example of a systematic effect that potentially shifts the measurement is the local star-formation bias (Rigault et al., 2013), according to which SNe Ia in locally star-forming regions are fainter than SNe in locally passive environments. Since the fraction of SNe in star-forming environments changes with the evolution of the universe, this can lead to a bias in the determination of cosmological parameters. In Rigault et al. (2015), the effect has been shown to reduce the tension between direct measurements of the Hubble constant from SNe Ia (Riess et al., 2011) and indirect measurements from the CMB (Planck Collaboration XVI, 2014) to $\sim 1\sigma$. The local star-formation bias affects the direct measurement because all of the very nearby SNe Ia whose absolute magnitude where determined using the Cepheid period–luminosity relation were located in star-forming region, while only $\sim 50\%$ of the SNe in the Hubble Flow were from such environments. In this section the measurement of anisotropies will be discussed in the context of redshift or sample-dependent systematic errors on the distance modulus and explicitly direction-dependent systematic errors.

Redshift-dependent effects To first order, a redshift-dependent systematic error averages out when inferring directional bulk flows. It is only because of e.g. anisotropic sky coverage, that the averaging process can result in a residual bias. For the analyses presented here the distribution of SNe on the sky has a great impact on the sensitivity in a given direction, e.g. if most observations lie in a direction perpendicular to the dipole, no good constraints on its value can be derived. Alternatively if a SN sample that lies in a preferred direction has a systematic bias, this will induce a false bulk flow signal.

---

[3] Perturbations of the SN luminosity distance due to gravitational lensing are also correlated to the structure but, unlike peculiar velocities, the are not caused by attractors near the SNe, but by the mass concentrations along the line of sight. Therefore, these perturbations become larger with distance and mostly affect smaller angular scales (multipole orders $\ell > 10$, see Bonvin et al. 2006a)

	Union2			SNFACTORY			Union2+SNFACTORY		
z	l [°]	b [°]	$\lvert\bar{\boldsymbol{n}}\rvert$	l [°]	b [°]	$\lvert\bar{\boldsymbol{n}}\rvert$	l [°]	b [°]	$\lvert\bar{\boldsymbol{n}}\rvert$
0.015-0.035	150	52	0.297	92	-25	0.409	136	45	0.259
0.035-0.045	163	45	0.255	82	-15	0.311	106	10	0.199
0.045-0.06	218	-75	0.375	79	-43	0.497	90	-66	0.384
0.06-0.1	139	-70	0.340	85	-12	0.394	91	-30	0.324
0.1-0.2	120	-64	0.666	–	–	–	–	–	–
0.2-0.3	92	-57	0.810	–	–	–	–	–	–
0.3-0.4	127	-56	0.571	–	–	–	–	–	–
0.4-0.5	167	9	0.209	–	–	–	–	–	–
0.5-0.6	165	-38	0.112	–	–	–	–	–	–
0.6-0.8	124	-2	0.132	–	–	–	–	–	–
0.8-1.4	133	33	0.351	–	–	–	–	–	–

Table 6.3: Sample characteristics of the SN Ia datasets in the redshift shells used for the dipole fit and smoothed residuals, calculated according to equation (6.2).

To quantify this effect, we calculate the weighted mean direction $\bar{\boldsymbol{n}}$ of the datasets, i.e.

$$\bar{\boldsymbol{n}} = \frac{\sum_i w_i \boldsymbol{n}_i}{\sum_i w_i} \quad \text{with} \quad w_i = \frac{1}{\sigma(\mu_i)^2} \frac{(1+z_i)^2}{H(z_i) d_{\mathrm{L}}^{(0)}(z_i)} \tag{6.2}$$

where $\boldsymbol{n}_i$ is the unit vector for the coordinates of a SN. The weights w_i are calculated from the uncertainty $\sigma(\mu_i)$ of the distance modulus and the ratio of the luminosity distance $d_{\mathrm{L}}^{(0)}$ to it first-order perturbation $d_{\mathrm{L}}^{(1)}$ as defined in equation (5.1) for a dipole anisotropy. The latter contribution to w_i corresponds to the fact that in the dipole fit analysis SNe at higher redshifts have a smaller weight on the inferred bulk motion because the effect of peculiar velocities on the distance modulus decreases with distance. Note that the dependence of $d_{\mathrm{L}}^{(1)}$ on the dipole velocity amplitude v_{d} cancels when dividing by the sum of the weights because it is linear in v_{d}. For a perfectly homogeneous distribution of observations $\bar{\boldsymbol{n}}$ would vanish. In that case the sources of systematic errors in cosmological analyses would average out in the measurement of the bulk flow. If, on the other hand, the amplitude of $\bar{\boldsymbol{n}}$ is non-zero, the systematic effects would shift the resulting bulk flow in the direction of $\bar{\boldsymbol{n}}$ proportionally. The absolute values of $\bar{\boldsymbol{n}}$ and its direction for each redshift shell are shown in table 6.3.

It can be expected that the different SN samples, which where obtained with different telescopes and analysis pipelines, will have a different degree of bias, i.e. all brighter or dimmer than expected. Amanullah et al. (2010) have investigated such biases within the Union2 compilation, and at the level of the statistical errors that range from 0.01 to 0.05 mag, have not found evidence for their presence. Furthermore the effect of redshift-dependent systematic uncertainties, e.g. reference star colours, which are the largest contributor to the systematic uncertainties (see Amanullah et al. 2010), is considerably smaller because the portion of our SN sample with a statistical weight spans a small redshift range. Assuming that all SNe in a redshift shell are biased by δm [mag], the resulting bias in velocity would be

$$\delta \boldsymbol{v}\,[\mathrm{km\,s^{-1}}] \approx 1.3 \times 10^5 z \cdot \delta m \cdot \bar{\boldsymbol{n}}, \tag{6.3}$$

where the factor was derived numerically by inverting and linearizing the relation for luminosity distance for a dipole anisotropy (5.1). Hence, for the lowest redshift bin ($|\bar{\boldsymbol{n}}| = 0.259$), assuming a bias of

0.03 mag, one would obtain a velocity bias of $\sim 25\,\mathrm{km\,s^{-1}}$. For the redshift shell $0.035 < z < 0.045$, one would obtain a velocity bias of $\sim 30\,\mathrm{km\,s^{-1}}$, while for the redshift bins $0.045 < z < 0.06$ and $0.06 < z < 0.1$ one would obtain a velocity bias ~ 80 and $\sim 100\,\mathrm{km\,s^{-1}}$, respectively. This potential bias should be put into context of the statistical uncertainty. The achievable statistical uncertainty can be approximated by linearizing the effect of the velocity on the distance modulus:

$$\mu = 5\log\left(H_0(cz+v)/10\,\mathrm{pc}\right),$$
$$\left.\frac{\partial\mu}{\partial v}\right|_{v=0} = \frac{5}{\ln 10cz}.$$

The dipole velocity derived by a fit of the amplitude in a certain direction can then the approximated by the following formula:

$$\sigma_v = \frac{\ln 10cz}{5}\frac{\sigma_\mu\sigma(\cos\theta)}{N_{\mathrm{SN}}^{1/2}}$$
$$\Rightarrow \sigma_v\ [\mathrm{km\,s^{-1}}] \approx 3.6\times10^4\cdot z\cdot N_{\mathrm{SN}}^{-1/2}, \tag{6.4}$$

where N_{SN} is the number of SNe and an isotropic distribution[4] and a distance modulus uncertainty $\sigma_\mu = 0.15$ was assumed. For all shells it can be seen that such a bias would be smaller than the statistical error. For a sample of ~ 1400 SNe with $\bar{\boldsymbol{n}} = 0.25$, the statistical uncertainty would be of the same order of magnitude as the bias. This estimate is independent of the redshift to first order because both $\delta\boldsymbol{v}$ and σ_v are linear in the redshift. Note furthermore that the bias as described by $\bar{\boldsymbol{n}}$ is a vectorial quantity and as such will have the strongest effect on the velocity if it is parallel or antiparallel to the bulk velocity – otherwise it will mainly change the direction.

Monopole To absorb any bias that may be present due to a constant redshift shell-dependent magnitude offset, a *monopole velocity* v_{m} was added to the luminosity distance in equation (5.1):

$$d_{\mathrm{L}}(z) = d_{\mathrm{L}}^{(0)}(z) + \frac{(1+z_i)^2}{H(z_i)}\left(\boldsymbol{n}\cdot\boldsymbol{v}_{\mathrm{d}} + v_{\mathrm{m}}\right). \tag{6.5}$$

This term corresponds to an isotropic boost to the recession velocity in the redshift shell that is analysed. For the SN magnitudes this translates to an equal shift of all luminosities in that bin, while a dipole term causes SNe in one half of the sky to appear brighter than expected from their redshift and those on the other half to appear fainter. In most redshift shells, the monopole velocities are consistent with zero and all effects on the dipole velocities are within 1σ of the fit without a monopole. Exceptions, for which a large monopole was found, include the SNFactory data at redshifts $0.035 < z < 0.045$ and Union2 data at $0.4 < z < 0.5$ but both of these shells had very low p-values for the dipole fit. When calculating p_B quickly using the χ^2-distribution and $\Delta\chi^2$ (see section 6.3), those shells have p-values of 0.179 and 0.143, respectively, which is a considerable improvement from 0.78 and 0.671 but still not significant. Also note that

Of greater interest are the first and fourth bin, where the best fit velocities have essentially not changed, indicating the absence of a potential bias due to a magnitude offset. For the case of the fourth bin ($0.06 < z < 0.1$), where the direction was fixed to the dark flow direction reported by Kashlinsky et al. (2010), the dipole velocity changes from $34 \pm 254\,\mathrm{km\,s^{-1}}$ for a fit without monopole term

---

[4] For an isotropic distribution the dispersion of the angle between the individual data points and a reference direction (e.g. of the bulk flow) is $\sigma(\cos\theta) = 1/\sqrt{3}$.

		dipole		**monopole**		
z	l [°]	b [°]	$\lvert v_\mathrm{d}\rvert$ [$\mathrm{km\,s^{-1}}$]	v_m [$\mathrm{km\,s^{-1}}$]	$\Delta\chi^2$	p_B
Union2						
0.015–0.035	289(23)	19(21)	283(96)	−29(61)	10.93	0.027
0.035–0.045	344(33)	−15(23)	816(581)	280(242)	2.82	0.589
0.045–0.06	40(41)	−22(32)	826(510)	258(301)	4.66	0.324
0.06–0.1	49(86)	−2(50)	536(621)	155(305)	1.09	0.895
0.1–0.2	249(113)	−0(80)	1029(1513)	276(483)	2.80	0.592
0.2–0.3	329(91)	11(48)	2232(5628)	789(2920)	1.08	0.898
0.3–0.4	160(51)	−24(45)	3806(4025)	−1878(1747)	2.91	0.573
0.4–0.5	158(16)	17(9)	11621(5444)	−4244(1881)	6.87	0.143
0.5–0.6	8(91)	−16(29)	4293(4344)	873(1705)	1.23	0.874
0.6–0.8	341(81)	−49(45)	5659(4530)	146(2192)	3.20	0.525
0.8–1.4	80(63)	−13(26)	8000(10912)	−553(4270)	0.68	0.954
SNfactory						
0.015–0.035	337(184)	25(208)	113(433)	149(203)	0.97	0.914
0.035–0.045	262(24)	3(15)	1431(621)	619(258)	6.49	0.166
0.045–0.06	301(42)	42(39)	1131(508)	321(361)	8.57	0.073
0.06–0.1	200(334)	22(149)	117(467)	−125(294)	0.63	0.959
Union2+SNfactory						
0.015–0.035	298(24)	14(22)	247(93)	7(56)	8.60	0.072
0.035–0.045	301(33)	−15(17)	654(331)	262(150)	5.37	0.252
0.045–0.06	356(35)	24(33)	637(369)	161(206)	3.93	0.416
0.06–0.1	292(1594)	−71(543)	42(322)	−74(194)	0.23	0.994

Table 6.4: Results for a dipole fit extended by a monopole component v_m. The p_B-values were calculated based on the $\Delta\chi^2$-values using the χ^2-distribution (5.10) with $k = 4$.

to $-31 \pm 295\,\mathrm{km\,s^{-1}}$ with monopole term of $-81 \pm 187\,\mathrm{km\,s^{-1}}$. As predicted in section 6.1, shells that have mostly positive or negative values for the smoothed residual statistic have a more significant monopole, notably the second shell ($0.035 < z < 0.045$) of the combined dataset has a monopole velocity of $262 \pm 150\,\mathrm{km\,s^{-1}}$ with the larger dipole amplitude but no significant change in the direction. The p_B-value decreases from 0.483 to 0.252, which is closer to the p-values from the smoothed residuals method. Another bin where this occurs is the Union2 dataset at redshifts $0.4 < z < 0.5$ where the p_B-value decreases from 0.671 to 0.142. Since the other shell do not show such a strong shift, this may very likely be just due to noise.

As SN datasets for redshifts $0.03 < z < 0.1$ are still limited, one needs to be careful when combining two datasets with $\bar{\boldsymbol{n}}$ pointing in opposite directions. For the combination of the Union2 and SNfactory datasets, one therefore needs to check that this is not the case, finding that the angles between $\bar{\boldsymbol{n}}$ do not exceed $\sim 90^\circ$ for all shells (see table 6.3). Additionally the amplitudes of $\bar{\boldsymbol{n}}$ are smaller than 0.5 for all shells with $z < 0.1$ and smaller than 0.45 for the combined data. For higher redshifts the absolute value can be larger, especially for $0.1 < z < 0.4$ because the SNe from SDSS (Holtzman et al., 2008) are clustered in one direction. At redshifts beyond that the SNe are still clustered in small fields, however, the directions to those fields are spread more evenly throughout the sky.

SN Ia standardization Another test for systematic differences can be preformed using alternative corrections of the SN magnitude that we can apply to the SNfactory dataset. As was shown in Bailey et al. (2009), using the ratio of spectral flux at 642 nm and 443 nm reduces the intrinsic scatter further than using the SALT2 lightcurve fit parameters x_1 and c. This correction was applied to 93 of the 117 SNfactory SNe and the results were compared with those for the SALT2-corrected distance moduli of the same SNe, finding the changes to be below 1.2σ for the direction and below 0.4σ for the bulk flow velocity. The change of direction can be that large if the velocity amplitude is small for the regularly corrected data and large for data correct using flux ratios (or vice versa). In that case the direction can differ greatly between the analyses and the one with a larger velocity amplitude will have lower uncertainties in the direction. There the direction can easily disagree by more than 1σ. The test of the tension using Cartesian coordinates described in section 5.1 (and used in section 6.1) is more robust against this. Using this test, the tension between the different methods of correcting the SN Ia magnitudes are found to have tension $\Delta^2 < 1.4$ corresponding to probabilities > 0.7 for random occurrence. Of course, these probabilities are expected to be large since the results are based on the same data and only the analysis method differs slightly.

Host bias Recent studies have shown that the standardized magnitudes of SNe Ia are correlated with the properties of their host galaxies, such that SNe in galaxies with higher stellar mass M_* are brighter on average (Kelly et al., 2010; Sullivan et al., 2010; Lampeitl et al., 2010; Childress et al., 2013b). To test the impact of this on the analyses, a mass step function was implemented, i.e. the SNfactory dataset was split at $\log(M_*/M_\odot) = 10$ (using host mass data presented in Childress et al. 2013a) and the analysis allowed for different normalizations of the split samples. There is no change in the bulk flow results (less than 0.15σ for the bulk flow velocity and 0.3σ in the direction.) Similarly, an extension of the SALT2 correction was tested by adding the logarithm of the host metallicty from Childress et al. (2013a). This limited the dataset to 68 SNe. The results did not change significantly (by less than 0.1σ for both bulk flow direction and velocity) when comparing the result for these 68 SNe with and without the additional correction.

Similarly to the global host galaxy properties, the properties of the local environment of a SN have been shown to affect its corrected magnitude (Rigault et al., 2013). Specifically, it was observed that

z	N_{SN}	l [°]	b [°]	$\lvert v_{\mathrm{d}}\rvert$ [km s^{-1}]
		with local star-formation bias		
0.015–0.035	34	4(27)	34(19)	538(198)
0.035–0.045	27	259(68)	−30(34)	424(321)
0.045–0.06	26	6(59)	12(37)	548(461)
0.06–0.1	53	185(143)	−44(113)	227(361)
		without local star-formation bias		
0.015–0.035	34	12(27)	36(18)	550(203)
0.035–0.045	27	254(74)	−29(39)	382(317)
0.045–0.06	26	359(67)	16(44)	483(456)
0.06–0.1	53	181(122)	−34(106)	223(408)

Table 6.5: Results of dipole fit to the combined dataset with and without local star-formation bias based on the results of Rigault et al. (2013, 2015).

the mean standardized magnitude of SNe Ia in regions with Hα emission is 0.094 ± 0.031 mag fainter than in regions without. As Hα emissions indicate active star formation, this bias is commonly referred to as the local star-formation bias. A followup paper to the original analysis of the bias (Rigault et al., 2015) confirmed the effect for the Constitution dataset (Hicken et al., 2009a). Since this dataset has an overlap with the Union2 compilation, the effect of the bias on the dipole fit can be tested for the combined dataset. Data of the local star-formation is available for 58 SNe at redshifts $z < 0.1$ in the Union2 compilation, of which 31 are in star-forming regions (called SNe Iaα) and 27 have passive environments (SNe Iaϵ). For the SNFACTORY dataset used in this analysis, 82 SNe have measurements of their local Hα line; half of those SNe are locally star-forming while the other half is passive. The results of Rigault et al. (2013, 2015) can be reproduced by fitting an offset of the normalization between the SNe Iaα and Iaϵ. Although this is in part the same data as used in those analyses, the exact methods of standardization may differ slightly and therefore this step needs to be repeated. The bias determined by this fit 0.062 ± 0.027 mag, which is consistent with the previous measurement by Rigault et al. (2013). The effect of the bias can then be assessed by repeating the dipole fit twice: in the first case the star-formation bias is included as the determined offset between SNe Iaα and Iaϵ; in the second fit this offset is neglected but the dataset is restricted to the same SNe. The results of these fits are shown in Table 6.5. The effect of the bias is well within the standard deviations of the results, the p-values for real tension between the results are larger than 0.99 for all redshift shells. This was expected because the bias is not correlated to the location of the SNe on the sky but SNe Iaα and Iaϵ are distributed evenly on the sky (see figure 6.7).

Dust extinction Finally, there are explicitly direction-dependent systematic errors that need to be investigated. As the effect of extinction by dust in the Galaxy is anisotropic, it is expected to have a larger contribution to the systematic error of the bulk flow than on cosmological parameters. To assess the effect of such uncertainties, the distance modulus of each SN was increased by 10% of the reported extinction in its direction (Schlegel et al., 1998). This changes the inferred bulk flow and its direction by less than 0.05σ. Hence Milky Way extinction can be considered a small source of systematic uncertainties for these datasets. Improper atmospheric extinction corrections can also lead to a directional bias. However, it is usually an integral part of a calibration procedure that relies on few

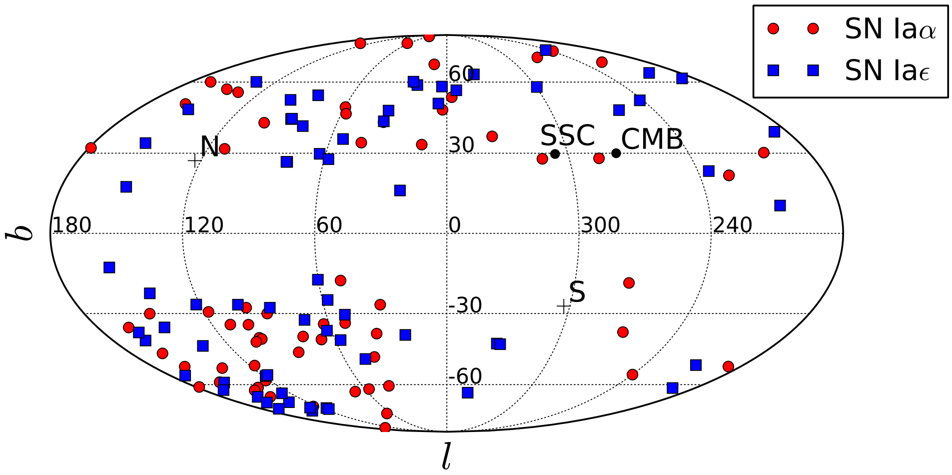

Figure 6.7: Locations of SNe in star-forming (SNe Iaα, red circles) and passive environments (SNe Iaϵ, blue squares) according to Rigault et al. (2013, 2015).

assumptions, hence resulting in a small contribution to the total magnitude error (see e.g. Regnault et al. 2009; Buton et al. 2013) that can safely be neglected for this work.

6.3 Comparison of randomization methods

In the first section of this chapter, the significances of the results in each redshift shell were expressed as p-values determined using two slightly different methods (as described in section 5.1). In this section the constraining power of both methods of randomization will be compared along with the difference between the two methods of detecting an anisotropy used in this analysis, dipole fit and smoothed residuals.

For the dipole fit the p-values from both randomization methods agree very well in nearly all redshift shells. Notable exceptions are the shell at $0.045 < z < 0.06$ for both datasets and their combination as well as the Union2 data at $0.3 < z < 0.4$. Figure 6.8 shows the distributions of the test statistics obtained from 250 000 realizations; they are plotted for two example shells of the Union2 compilation and one of the SNFACTORY dataset. In addition the expected test statistics were estimated using a modified version of randomization method B, in which the distance moduli were perturbed by coherent peculiar velocities before adding the random Gaussian noise. Two velocity models were used for this: the first only contained a dipole, while the second included a monopole term as well. The latter model was chosen because the better performance of the smoothed residuals methods in some redshift shells was attributed to a monopole term. Therefore, simulated data with a monopole term would be expected to give better p-values on average for the smoothed residuals than for the dipole fit The best-fit parameters for these models were used to set the velocity amplitudes. The dipole results are listed in table 6.1, whereas the monopole velocity results were discussed in section 6.2 and are listed in table 6.4. These simulations of anisotropic data were run 50 000 times for the shell shown in the plots and at least 5000 times for all other shells. Each time the analysis methods from sections 5.1 and 5.2 were applied to the same set of random data. This allows an analysis of the correlation of small/large p-values for the analysis methods to assess how consistently the methods will identify significant anisotropies.

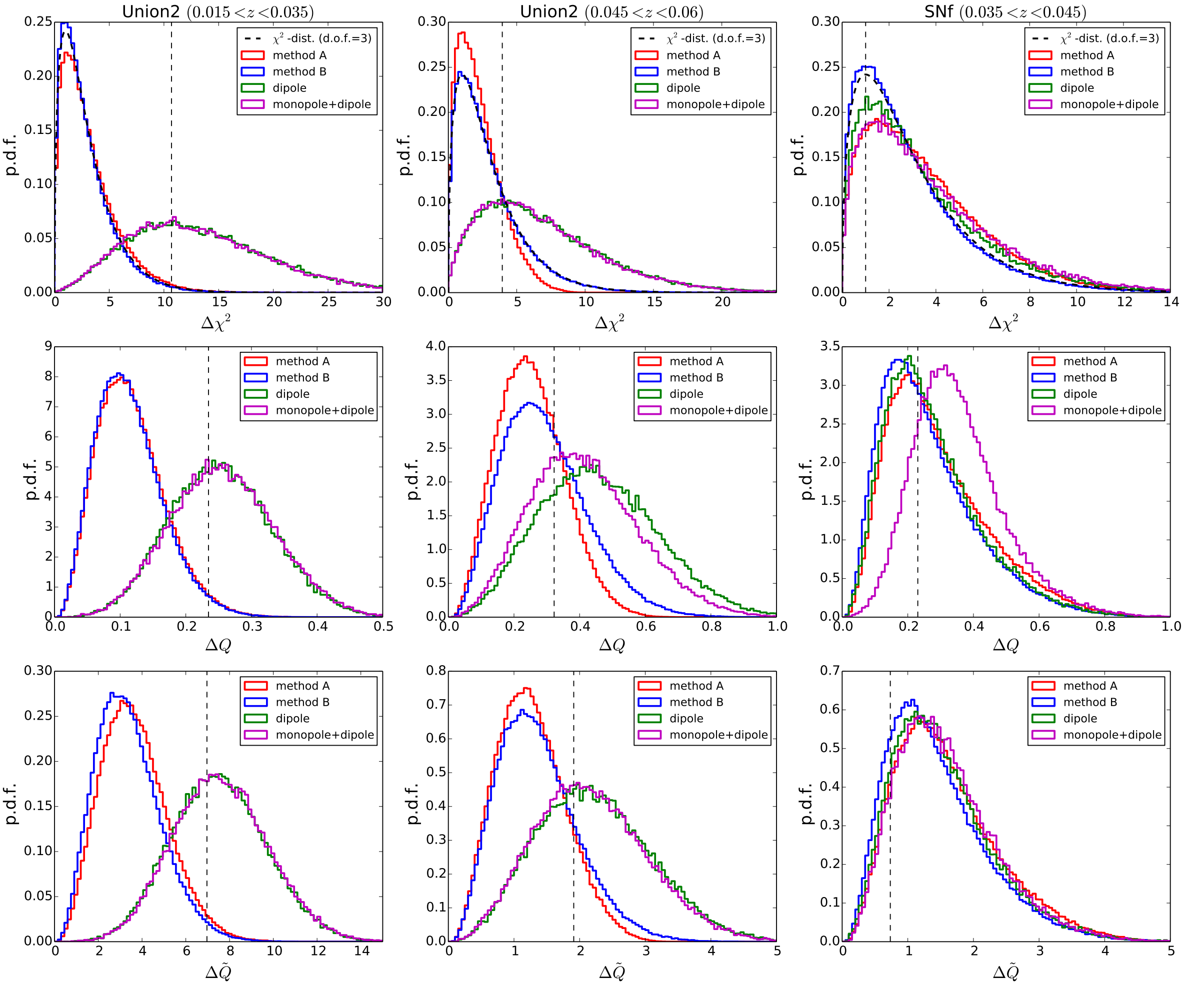

Figure 6.8: Comparison of randomization methods for p-value determination. The red and blue lines show distributions of the test statistic for random realizations of the null hypothesis (no anisotropy); the magenta and green lines show the distribution for dipole anisotropies with and without a monopole, respectively. The columns show results for the first and third shell of the Union2 as well as the second shell of the SNfactory dataset, respectively. The first rows shows the dipole fit method while the other two show the smoothed residual method, normalized and non-normalized, respectively. The vertical dashed lines show the value found for the real data. In the first row, the χ^2-distribution function (equation 5.10) is plotted for comparison.

The red and blue lines of figure 6.8 show the distributions of the test statistics for the two null-hypothesis methods described in section 5.1. In case of the dipole fit, the random realizations from method B (blue line) follow the χ^2 distribution function (equation 5.10; plotted as dashed line for reference) very well. Therefore, the p_B-value for the dipole fits can also be estimated more quickly from this distribution. This has already been used for tests of systematic effects in section 6.2 to save calculation time. The results for method A, on the other hand, do not follow this distribution exactly. This is expected, since this method redistributes the actual Hubble residuals randomly, which corresponds to drawing from an empirical distribution that is not fully Gaussian. The distribution for method A can have a shorter or longer tail, which in turn leads to smaller or larger p-values, respectively. This difference is not restricted to the dipole fit method but the same redshift shells tend to have larger p_B than p_A for both smoothed residual methods. However, for the smoothed residuals no analytical expression is known for the distribution of test statistics from either method.

Based on the simulated anisotropic data, one can determine the probability of the p-values for the real data occurring for anisotropic data. Note that regardless of the velocity model (dipole only or dipole+monopole), the simulated data was always analysed with the method used in section 6.1. In figure 6.8 these results are shown as green and magenta lines. In most examples the distributions are very similar. This includes the dipole fit in all shells; the only shell with a small difference is the second shell of the SNFACTORY dataset (upper left panel of figure 6.8), where the distribution for the dipole+monopole model has a marginally longer tail. Given that the monopole results in this shell have a considerably lower p_B-value than for a dipole fit (0.179 instead of 0.78), it is the best test case for a monopole that could lead to low p-values for the smoothed residual method while the dipole fit returns large ones. Thus, for the second shell of the SNFACTORY data (right column), the dipole+monopole simulations show a trend towards larger ΔQ (normalized smoothed residuals), leading to smaller p-values. The distributions for the two simulations cannot be distinguished by the other two methods in the same shell. In general, a difference between the simulations is only seen in the normalized smoothed residuals, the dipole fit and non-normalized smoothed residuals show very similar distributions for both simulations over the whole redshift range. Therefore, a large monopole term can only explain the smaller p-values found for the normalized smoothed residuals but not for the non-normalized method.

Figures 6.9 and 6.10 show the correlations of simulated p-values from the different analysis method as 2D-histograms for the third shell of the Union2 compilation and the second shell of the SNFACTORY dataset. In both figures, it becomes apparent that smaller and larger p-values are not fully correlated. Although small p-values for one method tend to correspond to small values for the other, there are occasional simulations, for which the one method finds large values, even if one of the others finds a small value. However, especially in the shells with better constraints the probability for this are low. For example, the p_A-values for the third shell of Union2 were 0.154, 0.121 for dipole fit and non-normalized smoothed residuals, respectively, showing no significant disagreement. According to the simulations, the probability of finding a larger p-value in a dipole fit while for the same data finding a smaller one with the smoothed residuals is 0.022 for simulations with only a dipole and 0.017 when including a monopole term in the simulation.

The second shell of the SNFACTORY dataset (figure 6.10) additionally shows the aforementioned trend towards lower p-values for normalized smoothed residuals in case of a monopole signal (lower left and lower right panel). The probability that a dipole fit gives a larger p-value in simulations than in real data while the normalized smoothed residuals give a smaller one is 0.011 for dipole only realizations but 0.056 for those with a monopole. Again this indicates that the normalized smoothed residual method can be affected by a monopole term, whereas this is not seen in the other methods.

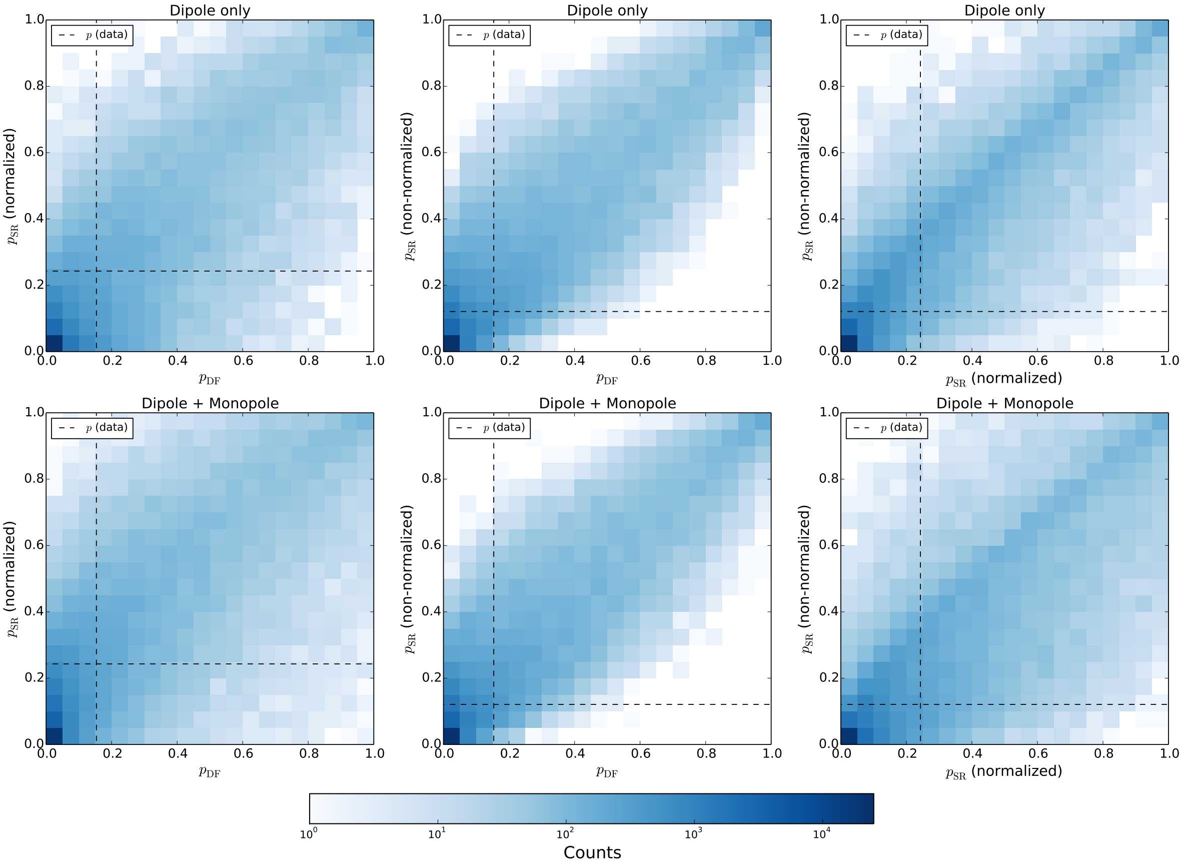

Figure 6.9: Comparison of p-value distributions for the third shell ($0.045 < z < 0.06$) of the Union2 compilation, based on 50 000 simulations of anisotropic data and 250 000 realizations of the null hypothesis using randomization method A. The rows show the results for simulation only a dipole (top) and a dipole and a monopole (bottom). Each column shows another combination of p-value estimates, marked by DF for the dipole fit and SR for smoothed residuals.

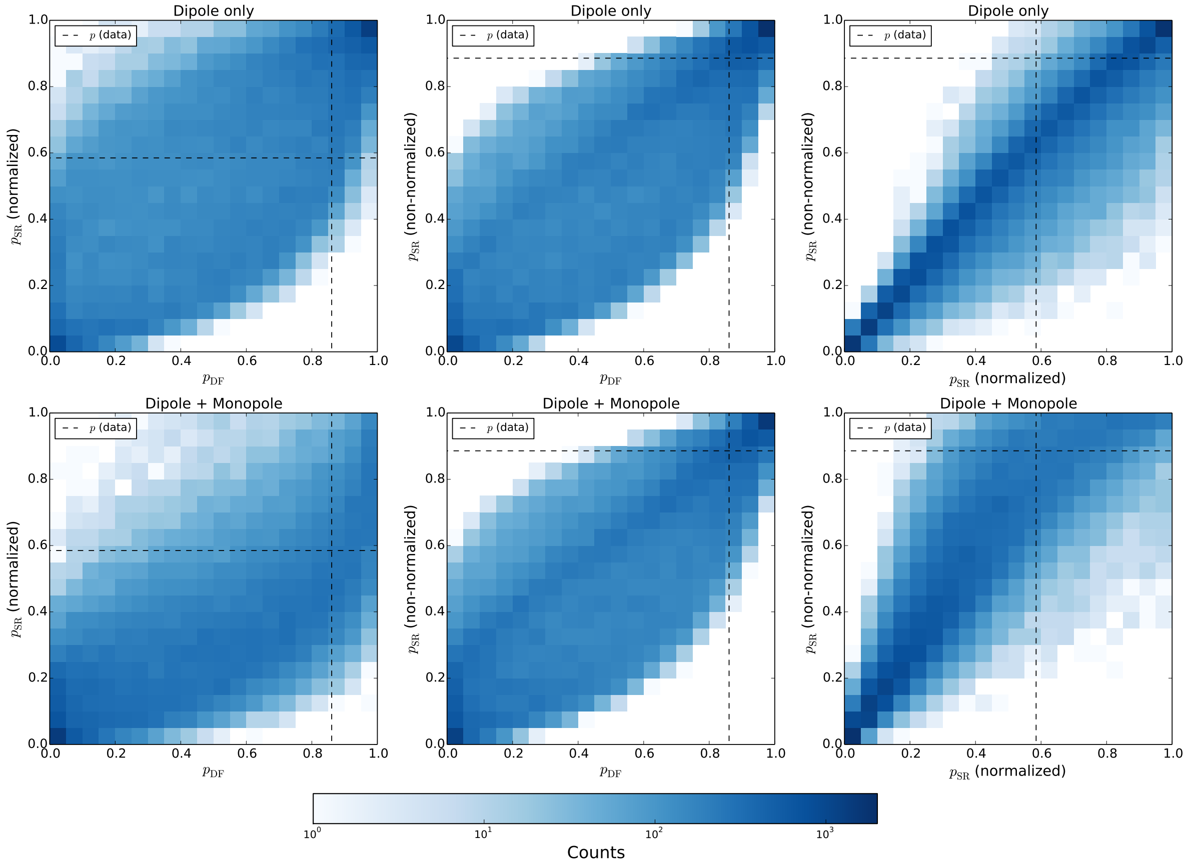

Figure 6.10: Comparison of p-value distributions for the second shell ($0.035 < z < 0.045$) of the SNFACTORY dataset, based on 50 000 simulations of anisotropic data and 250 000 realizations of the null hypothesis using randomization method A. Columns and rows as in figure 6.9.

CHAPTER 7

Gravitational Attractor

The results presented in the previous chapter have shown no evidence for a reversal of the dipole behind the Shapley supercluster (SSC), which therefore does not explain the bulk flow completely. However, the statistics in the redshift shells covering it were too low to find very significant results. On the other hand, splitting the data in shells was necessary to investigate the anisotropy in front of and behind the SSC in order to observe a potential backside infall. This chapter summarizes the results for an alternative, model-dependent approach that uses the whole dataset at once to constrain the flow towards a gravitational attractor. First, only a single spherical overdensity is used to investigate the role of the SSC and then a mass concentration in addition to the SSC is constrained, at first as a second spherical attractor and finally as a group of 13 attractors that model the Sloan Great Wall (SGW). Part of these results were presented in Feindt et al. (2013); the analysis has since been extended by the full determination the direction to the attractor and the model for the SGW.

7.1 Single Spherical Attractor

The SSC is a known mass concentration located in the direction ($l_{\mathrm{SSC}} = 306.44°, b_{\mathrm{SSC}} = 29.71°$; close to the CMB dipole) and therefore is expected to influence the motion of the Local Group (LG) causing the CMB dipole and the bulk observed at redshifts of $z \sim 0.03$. Previous studies of the SSC mass, e.g. based on the enhanced abundance of X-ray clusters (Muñoz & Loeb, 2008), have found it to contribute to the peculiar velocity of the LG only by $\sim 10\%$. Thus, combined with more local structures, e.g. the Great Attractor or the Local Void, which were found to explain $\lesssim 50\%$ of the Local Group velocity (see e.g. Kocevski & Ebeling 2006), it can apparently not explain the whole dipole. Other mass estimates of the SSC have found it to be 30% more massive (Lavaux & Hudson, 2011) or 40% less massive (Sheth & Diaferio, 2011) than found by Muñoz & Loeb (2008), with uncertainties between 5% and 20%. However, masses based on galaxy clusters depend on estimates of the functions relating the observables, e.g. abundance or luminosity, to the mass distribution, especially given that the major part of the matter in the universe is dark, and thus not observed directly. Studies using peculiar velocities, on the other hand, measure mass based directly on its gravitational effect that causes the velocities. They are therefore not affected by these biases. The SNFACTORY dataset is the first SN Ia sample that has sufficient coverage behind the SSC to measure its mass independently using the peculiar velocities and thereby verify previous mass estimates or contradict them.

Based on our prior knowledge about the SSC as a major mass concentration, the hypothetical attractor is first placed in the direction of the SSC while its redshift is varied to see what mass is required at different distances. Minimizing the expression in equation (5.26) yields the corresponding density contrast $\delta = \delta(z, l_{\mathrm{SSC}}, b_{\mathrm{SSC}})$ at redshift z that is necessary to account for the peculiar motions (see equation 5.23) present in the data. As a second analysis, the χ^2-function was minimized for the Galactic coordinates (l, b) along with the density contrast δ to test the assumption that the attractor is located in the direction of the SSC. As predicted velocity for a single SN can vary greatly when the attractor is placed too close to that SNe, and thus the χ^2-values as function of Galactic coordinates at a fixed redshift can have multiple local minima. The weighting for SNe inside the attractor (equation 5.25) increases this effect slightly since it reduces the value of χ^2 locally by deweighting the contribution of single data points. For comparability all results shown in this section will use this weighting scheme. However, this means that the directions found with this method depend greatly on the distribution of the data and should be taken with a grain of salt. To ensure that the numerical minimization converges in the global minimum, χ^2 is determined on a grid of directions within 45° of the direction to the SSC first and the minimum of that process is used as an initial guess for the optimization. This limits the possible best-fit directions to that part of the sky but this restriction is justified because the source of the bulk flow, which is known to point in that general direction, is the main interest in this analysis. To confirm that there are no well-fitting regions on other parts of the sky, χ^2 was calculated for the full sky at a few redshifts (see figure 7.1).

In figure 7.2 the required attractor mass for the peculiar velocity field extracted from all SNe at $z < 0.1$ in the combination of the Union2 and SNfactory datasets is shown as a function of redshift z in the direction of the SSC and for the best-fit direction. As the structures at lower redshift have already been mapped – using galaxies – to a greater extent than can be achieved with SNe, the redshift range of the model attractor was limited to $0.035 < z < 0.1$. Additionally, the angle between the direction to the SSC and the best-fit direction is shown in middle panel and the corresponding χ^2-values for the fit with equation (5.26) are shown in the bottom panel as a measure of the fit quality.

Attractor in SSC direction The main conclusion from this figure is that an attractor placed at large distances will have a large best-fit mass. This is because an attractor at larger distance leads to a more homogeneous peculiar velocity field (and thus less shear) in the nearby Universe. The attractor model thus asymptotically approaches the case of a dipole bulk flow. The mass increases with redshift because the density contrast δ at greater distance must be larger to cause the same bulk flow. It therefore grows with the square of the distance, i.e. $\delta \propto d^2$. Note that this result does not contradict our rejection of a Dark Flow in section 6.1 because this analysis uses all SNe at $z < 0.1$ and therefore SNe at low redshifts contribute to it, not just the ones at $0.06 < z < 0.1$.

A mass concentration in the proximity of the SSC is only marginally consistent with our data. The mass that is obtained for the redshift of the SSC ($z \sim 0.045$) is $6.7 \pm 2.0 \times 10^{16}\,M_\odot$, which is ~ 50% larger than the mass estimate by Muñoz & Loeb (2008) ($4.4 \pm 0.5 \times 10^{16}\,M_\odot$) that is shown as a green rectangle in figure 7.2. As mentioned above other studies found conflicting SSC masses: Lavaux & Hudson (2011) found a mass of $5.7 \pm 0.3 \times 10^{16}\,M_\odot$ while Sheth & Diaferio (2011), on the other hand, found a SSC mass of $2.6 \pm 0.6 \times 10^{16}\,M_\odot$; the mass found here is consistent with the former but disagrees at the 2σ-level with the latter. This considerable tension is discussed by Lavaux & Hudson, who point out that two biases may affect their measurement based on galaxies observed by the 2MASS infrared survey: (1) the results from luminosity-weighted 2MASS galaxies may be biased by a factor of $b_{K,n} = 1.56 \pm 0.16(\Omega_{\mathrm{m}}/0.3)^{0.55}$ (Davis et al., 2011a)[1], (2) their estimate was calculated in redshift space whereas the others are in real space, enhancing the result by $b_s = 1.2$ (Kaiser, 1987). These biases

---

[1] However, previous results for this bias were lower, e.g. $1.05 \pm 0.10(\Omega_{\mathrm{m}}/0.3)^{0.55}$ (Pike & Hudson, 2005).

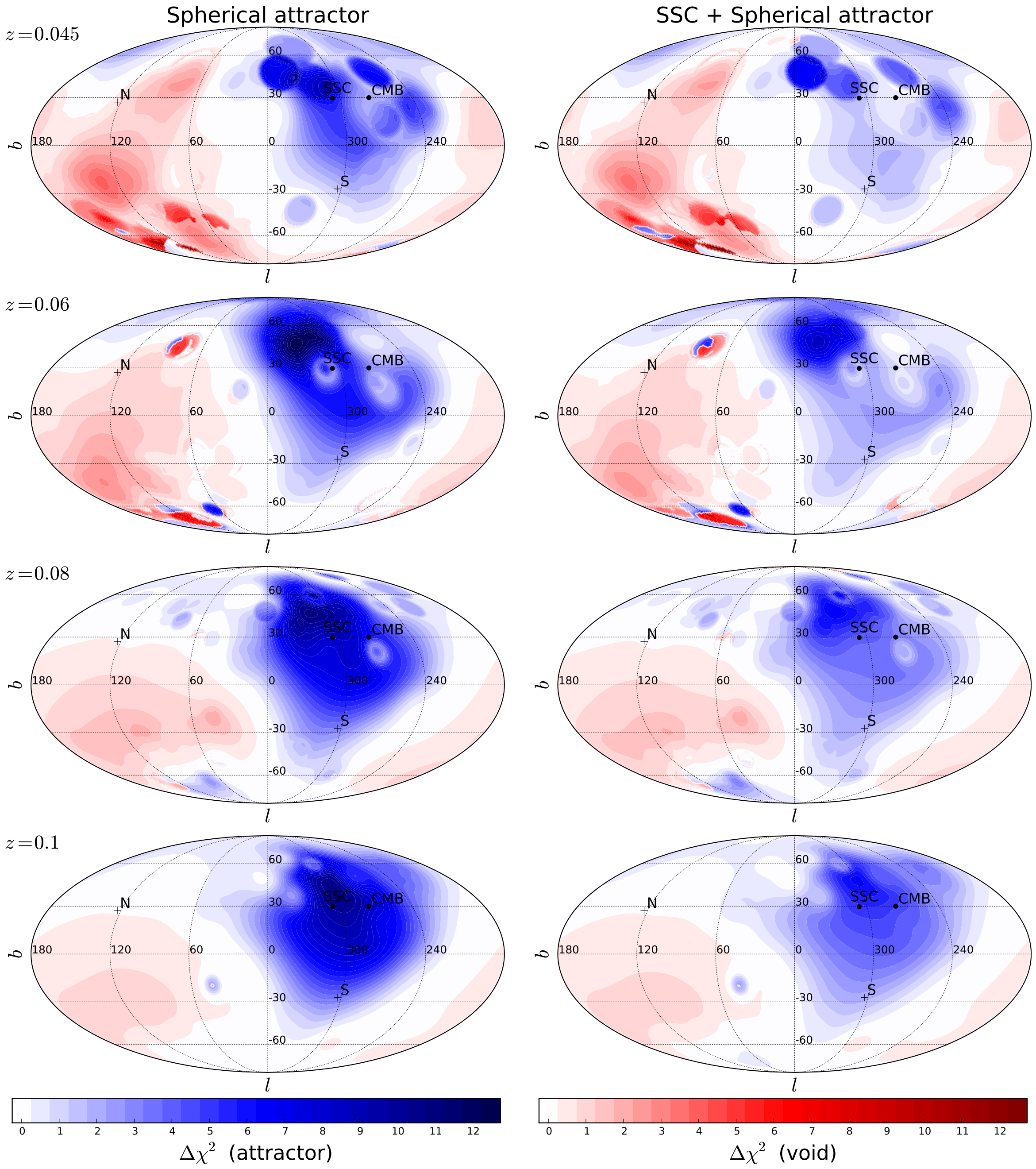

Figure 7.1: Variation of χ^2 for a spherical attractor fit of the combined dataset at redshift $z < 0.1$ as a function of Galactic coordinates (l, b) for four different attractor redshifts (rows). The left column shows results for a single attractor and the right column for an attractor in addition to the Shapley supercluster (see section 7.2). Two different colourmaps are used the distinguish attractors (density contrast $\delta > 0$, blue) from voids ($-1 < \delta < 0$, red).

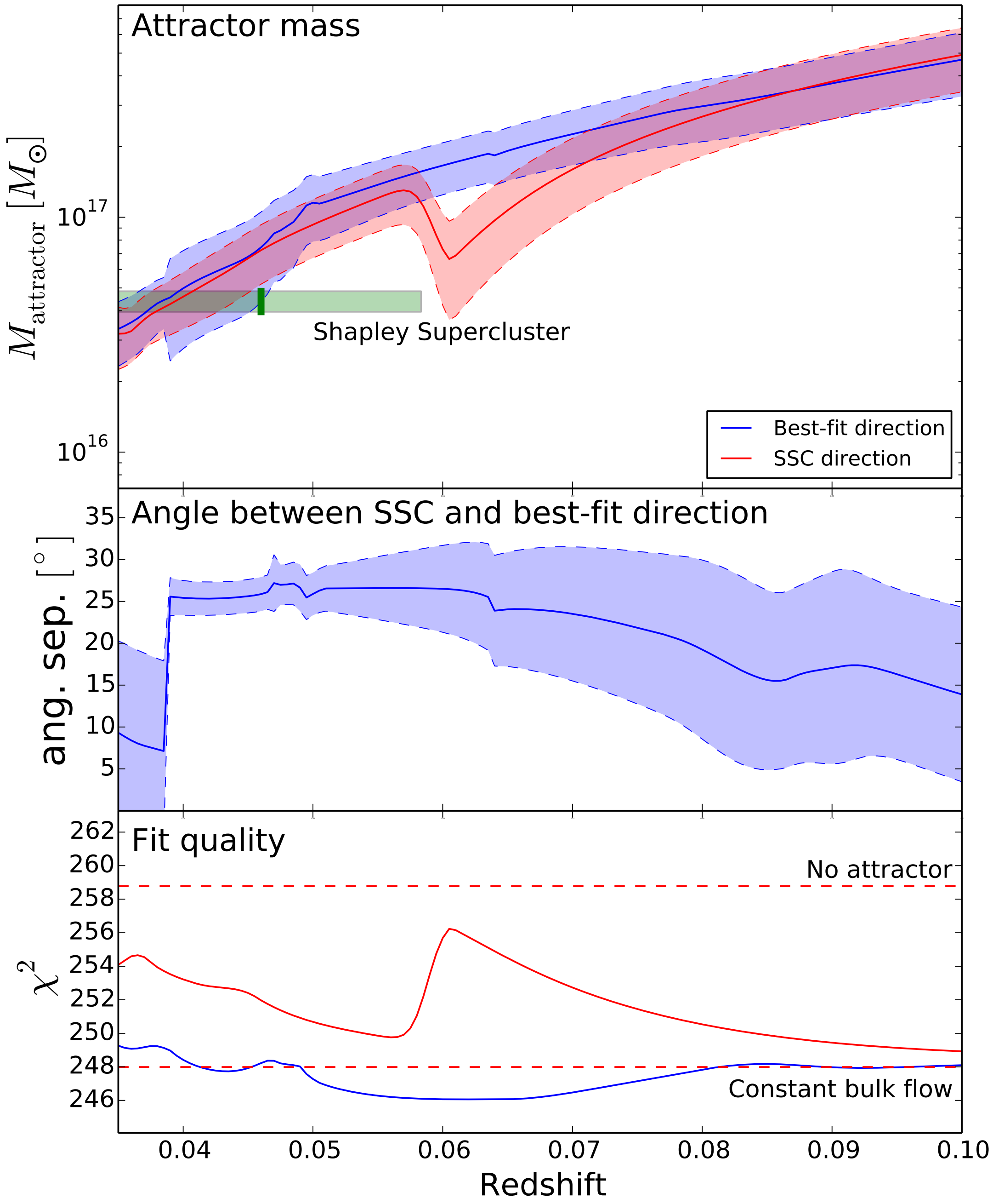

Figure 7.2: Attractor mass $M_{\mathrm{attractor}}$ as a function of redshift z accounting for the SNe Ia peculiar velocities in the combination of the Union2 and SNFACTORY datasets for the direction of the SSC (red) and for the best-fitting direction (blue). The lower panels show the angular separation between the direction to the SSC and best-fit direction and the minimum χ^2-values according to equation (5.26), respectively. The shaded areas show the uncertainties of the mass determined for a given attractor redshift. The green box shows the mass range as well as the approximate size of the SSC from Muñoz & Loeb (2008). The red dotted lines in the bottom panel show the χ^2-value for no attractor and for a constant bulk flow determined by a dipole fit to the data.

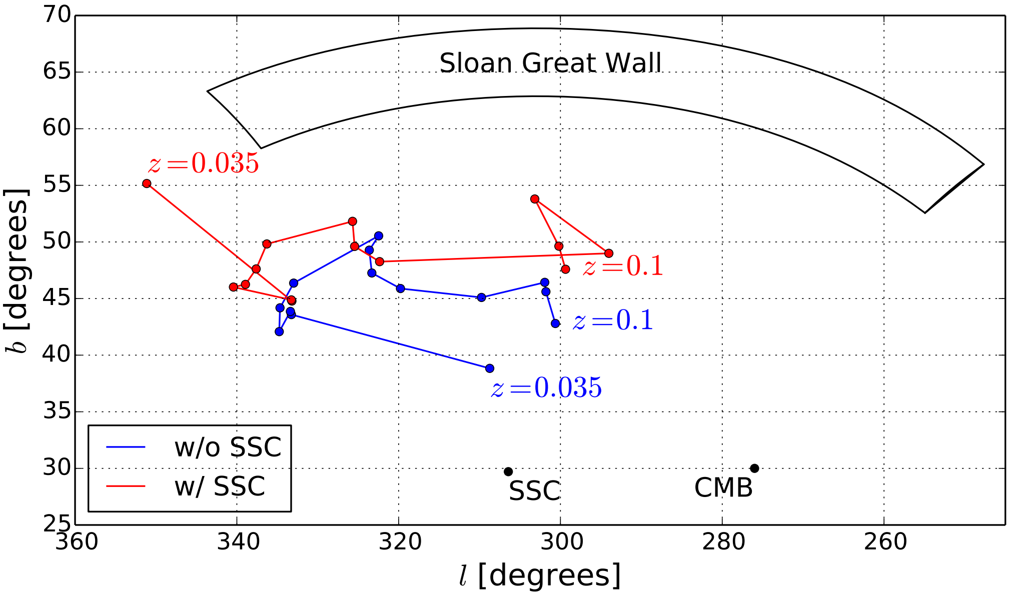

Figure 7.3: Best-fit attractor direction as a function of attractor redshift for fits of a single attractor (blue) and of an attractor in addition to the SSC (red). Each dot corresponds to a redshift step of 0.005. The approximate location of the Sloan Great Wall is shown as a box bounded by right ascensions $166° < \alpha < 210°$ and declinations $0° < \delta < 6°$ (Sheth & Diaferio, 2011).

could reduce the mass estimate by Lavaux & Hudson to a level that is more consistent with the others. In this case, the mass found in this study exceeds the other estimates, but is only inconsistent at 1.2σ with Muñoz & Loeb (2008). Therefore, our data mildly indicates that another attractor contributes to the bulk flow. Note that at this redshift the mass estimates show little dependence on the exact direction, in which the attractor is placed; for the best-fit direction the attractor mass increases insignificantly to $6.8 \pm 2.9 \times 10^{16}\,M_\odot$, though its uncertainty is larger because more parameters are inferred.

In addition to requiring more mass than observed by other studies, an attractor at the exact location of the SSC (direction and redshift) is disfavoured at a level of 2.1 σ ($\Delta\chi^2 = 4.4$) based on the quality of fit compared to a constant bulk velocity determined by a dipole fit of the same data. This $\Delta\chi^2$ decreases rapidly with redshift and disagrees by less than 2 σ at redshifts $0.046 < z < 0.058$, with a minimum of $\Delta\chi^2 = 1.8$ at $z = 0.056$. The fit quality at the end of the investigated redshift range $z = 0.1$, on the other hand, only differs from that of dipole fit by $\Delta\chi^2 = 0.9$. This conclusion is based purely on the shape of the gravitational field, and not the mass itself.

Attractor in best-fit direction For the full fit of direction and density contrast the fit quality is considerably flatter as a function of the redshift and roughly matches ($\Delta\chi^2 < 2$) that of a constant bulk flow for all redshifts. The global minimum is located around 0.62, where the full fit is better than the dipole fit by $\Delta\chi^2 = 1.9$. In addition to the angular separation shown in the middle panel of figure 7.2, the best-fit directions are shown in figure 7.3. At redshifts of $0.04 < z < 0.07$ the direction disagrees with that of the SSC by more than 3σ. However, due to the effect of single SNe on the χ^2-profile discussed at the beginning of this section, the uncertainties on the best-fit direction are likely underestimated. The χ^2-profile at exemplary redshifts is shown in figure 7.1. In general, the global minimum is located close to the direction to the SSC but some deviation are caused by the distribution of the data. For e.g.

$z = 0.045$ (upper left plot in that figure), the profile is very steep at the global minimum but this appears to be caused by the overlap of two regions of low χ^2-values. Since one of these regions extends to the SSC and has a local minimum near the SSC, it is not excluded at the degree that the uncertainties would indicate. For $z = 0.06$, on the other hand, there is a region of large χ^2-values around the SSC. Like the local minima, this is caused by a single SNe (SN 1993O) that is located in the SSC. Since this SN has a negative Hubble residual (appears to be moving towards us), placing the attractor behind SN 1993O leads to an increase in χ^2. This case shows a dependence on the assumed attractor radius (see below). Since the observed deviations are explainable by the data distribution, using the direction of the SSC in this analysis is still justified despite the apparent disagreement with the best-fit direction.

Effect of attractor radius Similarly, one must test whether the assumed radius of the attractor influences the fit results. As the velocity field outside the overdensity only depends on the total mass of the attractor, one can expect this influence to be small when fixing the direction to that of the SSC. However, as the velocity field inside the model attractor is sensitive to the radius, SNe inside the overdensity can affect the fit results. For the full fit, this has been observed as the multiple local minima near the direction of the SSC as discussed above. For the fixed-direction fit, five SNe are within the boundary of the attractor for some redshifts but their effect is limited by the deweighting according to equation (5.25). Only for SN 1993O (see also above) the effect remains noticeable as a dip in the χ^2-values and a bump in the attractor mass around $z \sim 0.05$, both of which become narrower for smaller radii. SN 1993O is located in the galaxy cluster Abell 3560 ($z = 0.49825$) within the SSC, 28 Mpc from its centre and therefore within the assumed spherical overdensity. For an attractor radius of 50 Mpc only the high-redshift edge of the χ^2-dip is visible as a large increase in the χ^2-value around at $z \sim 0.06$. This is not only caused by the SNe being inside the boundary of the attractor but rather by its proximity to the attractor in general. SN 1993O appears to be moving towards us and therefore an attractor placed behind it will lead to a much larger residual than an attractor in front of it. This effect is not seen immediately at the redshift of the SNe because it is suppressed by the weights w_i while the SNe is inside the overdensity. Removing SN 1993O from the dataset also removes the χ^2-step as well as the corresponding step in the attractor mass (see figure 7.4). For the SSC location ($z = 0.045$) variation of the attractor size or the exclusion of SN 1993O has little effect on the fit quality as the residual for SN 1993O is almost zero. Also the fit quality still approaches that of a constant bulk flow for larger distances.

Effect of voids In order to better understand the limitations of the simplified model the impact of inserting well-known major underdensities (voids) can be calculated. When including first the Local Void (modelled as a spherical region of radius $R = 30\,\mathrm{Mpc}$ and density contrast $\delta = -0.9$ located at $z = 0.007, l = 29.7°, b = 2.6°$), then the Boötes Void ($R = 50\,\mathrm{Mpc}, \delta = -0.7, z = 0.05, l = 34.7°, b = 70.2°$), the best fitting attractor mass in SSC direction only varies by $\sim 5\%$ and the quality of fit only changes by $\Delta\chi^2 \ll 1$. Likewise, older work based on the Abell cluster catalogue (Scaramella, 1995), or more modern works using very carefully constructed X-ray selected cluster catalogues (Kocevski et al., 2007) reinforce the view that the SSC is the major attractor within the redshift range of our supernova sample. Thus, though simple, the model employed here is sufficient for the purposes of exploring attractors in the direction of the SSC.

7.2 Attractor in Addition to the Shapley Supercluster

Additional spherical attractor Since a single SSC-like attractor was found to be insufficient, the analysis was repeated for an attractor in addition to the SSC. The fit was performed again with the SSC

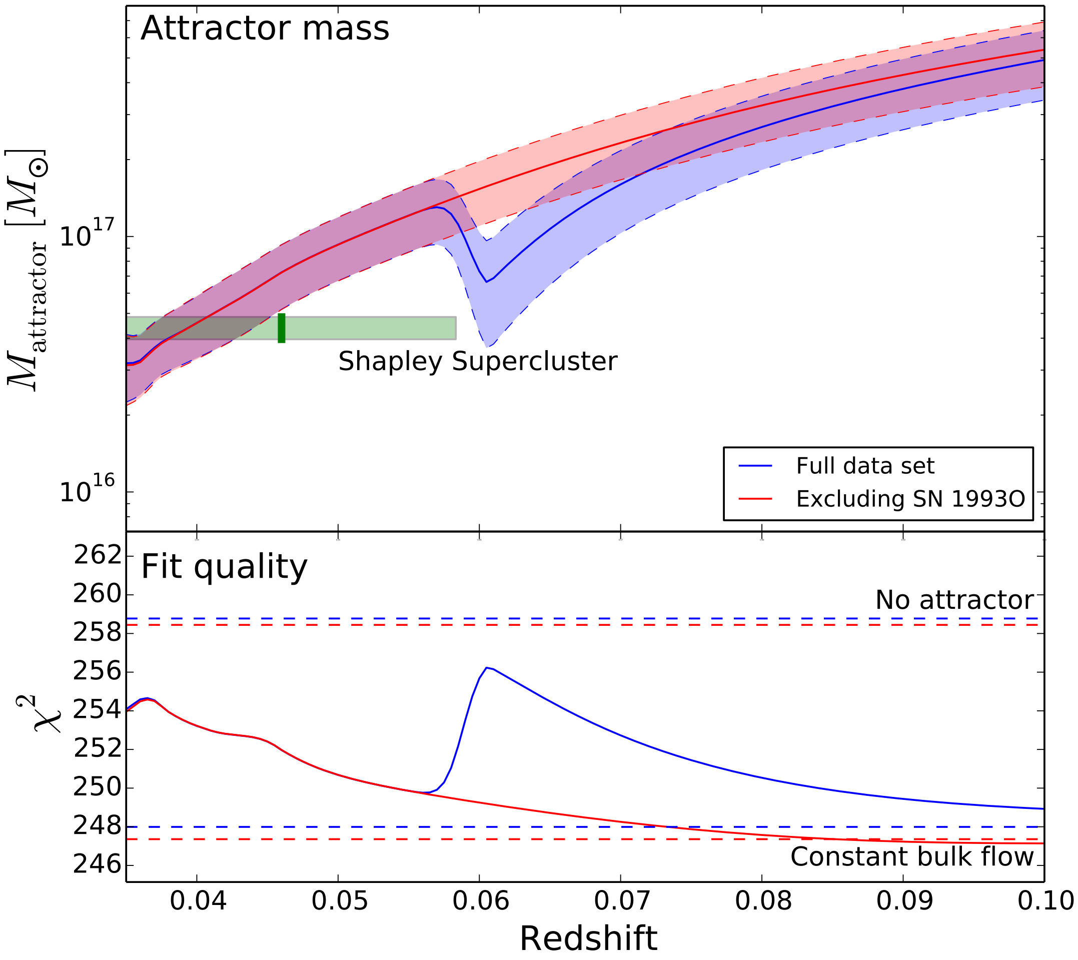

Figure 7.4: Attractor mass $M_{\text{attractor}}$ and fit quality as functions of redshift z as in figure 7.2 for the full dataset and excluding SN 1993O. The colours of the dashed lines in the lower panel correspond to those of the solid lines.

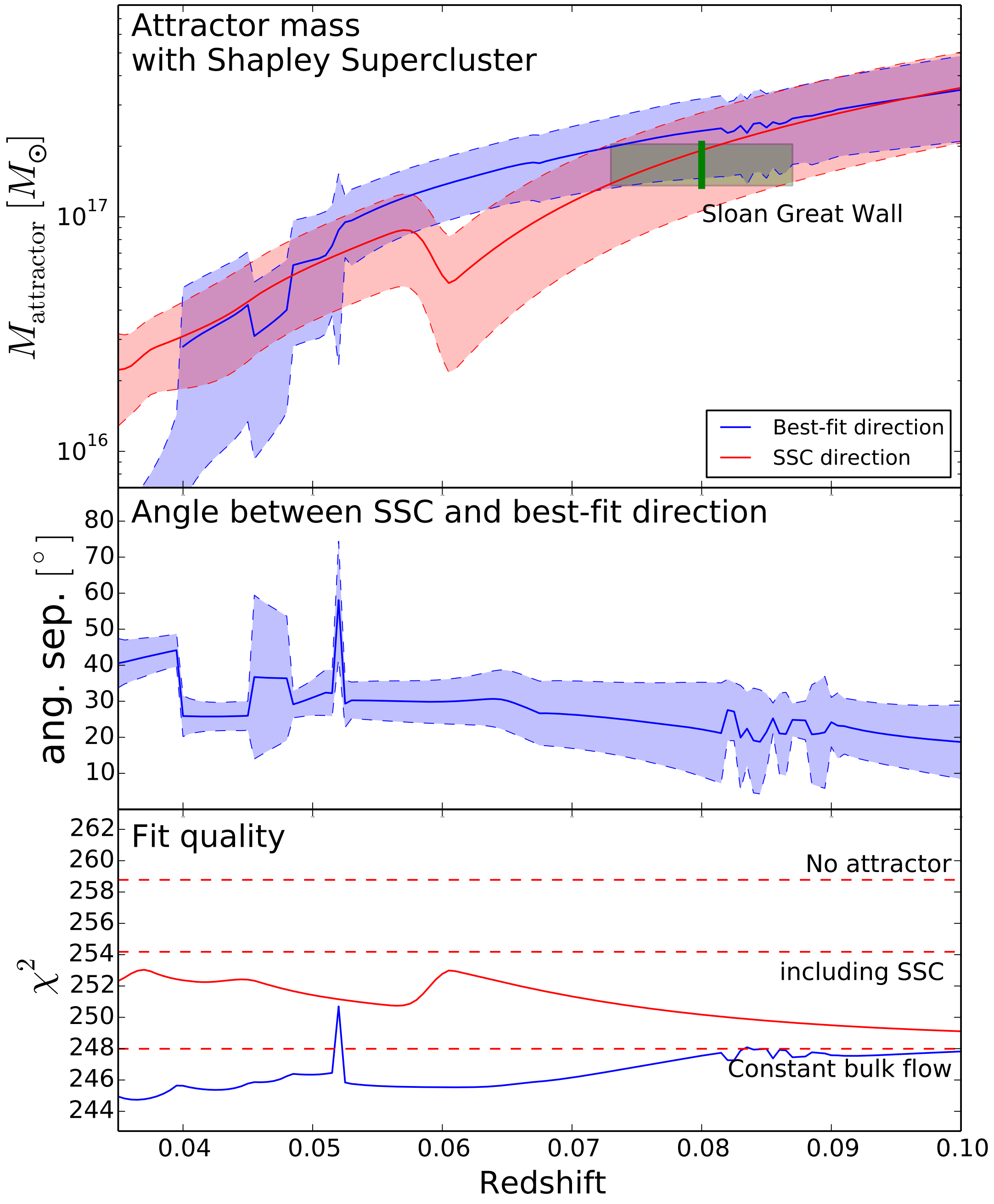

Figure 7.5: Attractor mass $M_\mathrm{attractor}$ as a function of redshift z as in Fig. 7.2 where an attractor of SSC mass and size ($4.4 \times 10^{16}\,M_\odot$, 50 Mpc) was inserted at $z = 0.045$. The green box shows the mass range as well as the approximate size of the Sloan Great Wall from Sheth & Diaferio (2011). The red dotted line shows the χ^2-values for the data after a Hubble fit without and attractor, when inserting the SSC and when fitting a constant bulk flow (dipole).

inserted as a fixed overdensity of mass $4.4 \times 10^{16}\,M_\odot$ and radius 50 Mpc at $z = 0.045$ (see figure 7.5). Figures 7.1 and 7.3 also show results for this model (right column and red line, respectively). For this mass fit in the SSC direction the local minimum of the χ^2-value near the SSC location becomes shallower, while the preference for a distant attractor remains. For the full fit, lower redshifts become more significant but not necessarily as an attractor. At redshifts $z < 0.04$ a void, i.e. a region of density lower than the average matter density of the universe ($-1 < \delta < 0$), about 40° from the SSC is favoured. Since the attractor mass cannot become negative, the density contrast needs to be restricted to values $\delta > -1$. Even when applying this restriction to the fit, voids have a lower χ^2-value at low redshifts. Recall that the initial guess for the full fit was restricted to a radius of 45° around the SSC direction. Figure 7.1 shows minima in the χ^2-profile for directions on the other side of the sky for the lower two redshifts shown (0.045 and 0.06). The positive-mass restriction was applied here as well; otherwise the best fit could be a negative mass attractor that causes a dipole much like the attractor fits show a growing mass for larger distances. Despite that there are also some realistic attractors in that part the sky, most notably around $z = 0.06$ and $l \sim 60°, b \sim -60°$ (possibly the Sculptor Wall at redshifts $0.03 < z < 0.054$ or the Pisces-Cetus superclusters at redshifts $0.039 < z < 0.072$, see Tully 1986; Maurellis et al. 1990; da Costa et al. 1994 for initial studies of that region and Springob et al. 2014 for a more recent survey), these were not studied further because the main interest of this study is the bulk, which they are not expected to contribute to. Furthermore, the χ^2-profile around the SSC extends almost to celestial south pole, where other mass concentration may be located. The Horologium-Reticulum supercluster has already been shown to contribute slightly to the LG motion Kocevski & Ebeling (2006) and another supercluster in the constellation Vela behind the Milky Way has recently been proposed[2]. These possible attractor could, however, not be constrained well by the current SN data because they are either too far south, where the coverage is low, or obstructed by the Milky Way.

The Sloan Great Wall It was shown in Sheth & Diaferio (2011) that a single supercluster of the mass of the SSC can still be expected for a sphere of $200\,h^{-1}$Mpc radius. An additional more distant supercluster seems an unlikely explanation, however, since it would need to be rather massive and hence would be rare: Extrapolating the mass function for superclusters from Lim & Lee (2014), one finds that e.g. a factor of 3 more massive cluster would already be ~50 times rarer. A better explanation might be a non-collapsed structure. The Sloan Great Wall (SGW) — the largest known structure in the universe — is located near the direction of the SSC, at a redshift $z = 0.07 - 0.08$. Its mass is estimated to be $1.2 \times 10^{17}\,h^{-1}M_\odot$ by Sheth & Diaferio (2011) and hence, together with the SSC, could explain the size of the bulk flow. The best-fit directions for the full fit are also mostly between the directions to the SSC and the SGW. However, since it is a strongly elongated mass concentration, the analysis using a spherical attractor cannot be applied directly.

Instead, as a simple first analysis of the effect of the SGW in addition to the SSC, it was modelled as a system of 13 superclusters as listed in table 1 of Einasto et al. (2011). Each supercluster was modelled as a spherical attractor of constant density contrast with radius according to the table. To model the different masses of those attractors without adding 13 additional parameters, the listed peak densities were used to fix all constituents' relative contributions $\tilde{\delta}_i$:

$$\tilde{\delta}_i = \frac{\rho_{\mathrm{peak},i}}{\sum\limits_i \rho_{\mathrm{peak},i}}, \tag{7.1}$$

---

[2] To date, there is no publication on the Vela supercluster but it has been presented by R. Kraan-Korteweg at conferences.

ID	l [°]	b [°]	d_{peak} [h^{-1}Mpc]	z_{peak}	ρ_{peak} [$\rho_{\mathrm{m},0}$]	Diam. [h^{-1}Mpc]
184+003+007	282.1	64.4	230.3	0.077	14.16	56.9
173+014+008	244.3	67.3	242.0	0.081	12.31	50.3
202-001+008	321.8	60.5	255.6	0.085	12.92	107.8
152-000+009	240.7	42.3	285.1	0.095	9.81	39.0
187+008+008	285.7	70.1	267.4	0.089	9.33	54.2
170+000+010	260.2	55.1	302.1	0.101	8.55	20.1
175+005+009	262.2	62.1	291.0	0.097	8.23	28.0
159+004+006	242.5	50.3	206.6	0.069	7.61	15.4
168+002+007	255.2	55.4	227.7	0.076	7.49	28.1
214+001+005	344.3	56.9	162.6	0.054	7.22	19.5
189+003+008	293.6	65.6	254.1	0.085	6.75	32.2
198+007+009	317.5	69.3	276.0	0.092	6.33	13.1
157+003+007	241.8	48.1	219.1	0.073	5.28	13.3

Table 7.1: Superclusters in the region of the Sloan Great Wall (data from Einasto et al. 2011). The ID denotes right ascension, declination and redshift of the clusters. The Galactic coordinates were calculated from to information in the ID while z was inferred from the distance to the cluster's peaks d_{peak}. The right-most two columns list the peak densities ρ_{peak} in units of the mean matter density of the universe and the supercluster diameter in units of h^{-1}Mpc.

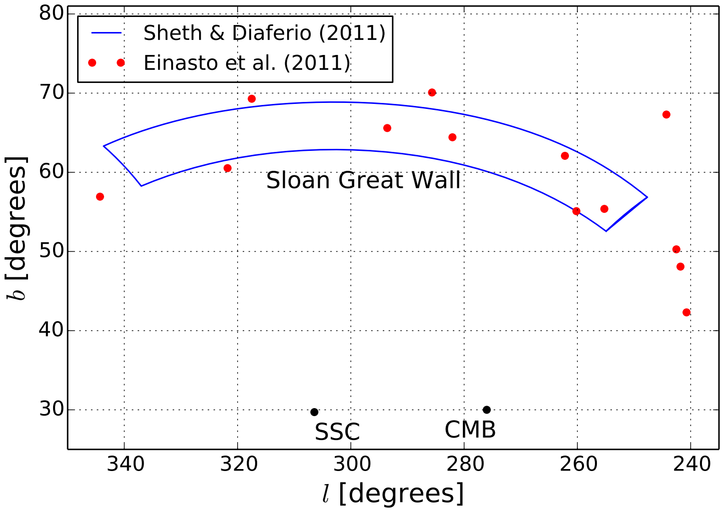

Figure 7.6: Locations of the superclusters in the SGW region. The red dots are the peak locations of the superclusters in the SGW from Einasto et al. (2011), cf. table 7.1. The blue box shows the approximate location of the SGW reported by Sheth & Diaferio (2011) (right ascension 166° $< \alpha <$ 210°, declination 0° $< \delta <$ 6°).

M_{SSC} $[M_\odot]$	M_{SGW} $[M_\odot]$	Source
$(4.4 \pm 0.5) \times 10^{16}$	—	Muñoz & Loeb (2008)
$(5.7 \pm 0.3) \times 10^{16}$	—	Lavaux & Hudson (2011)
$(2.6 \pm 0.6) \times 10^{16}$	$(1.7 \pm 0.4) \times 10^{17}$	Sheth & Diaferio (2011)
$(6.7 \pm 2.0) \times 10^{16}$	—	This work (SSC as single attractor at $z = 0.045$)
$(5.2 \pm 1.8) \times 10^{16}$	$(1.9 \pm 1.0) \times 10^{17}$	This work (SSC + SGW)

Table 7.2: Mass estimates of SSC and SGW from literature and this work.

where the $\rho_{\mathrm{peak},i}$ are the peak densities of the superclusters in units of the mean matter density. The supercluster data from Einasto et al. (2011) is reproduced in table 7.1 and their locations are shown in figure 7.6. Table 7.2 lists the results for the masses of the SSC and the SGW from this analysis along with values given in other publications. The best-fit SGW mass ($1.9 \pm 1.0 \times 10^{17}\ M_\odot$) matches the one found by Sheth & Diaferio (2011), but the uncertainty is larger by more than a factor three. The mass of the SSC is estimated to be smaller than when a single attractor is assumed and now consistent with the value given by Muñoz & Loeb (2008) (but not with the one in Sheth & Diaferio 2011). This further strengthens the hypothesis that the SGW contributes the unexplained component of the bulk flow. The χ^2-value for this model is 249.7, which is still slightly higher than the dipole fit ($\chi^2 = 247.99$). However, since only two (instead of three) parameters were used here the result is marginally better with $p = 0.0107$ opposed to $p = 0.013$ of the dipole fit.

CHAPTER 8

Simulations for Future Surveys

Only some of the results of the previous chapters were significant; for better constraints more data, especially at the distances of the SSC and SGW, will be required. Therefore, the prospect for analyses based on future SN survey needs to be investigated. Since the start of the presented analysis the available dataset has grown slightly; by now more low-redshift SNe have been published, e.g. by CSP (Hamuy et al., 2006; Stritzinger et al., 2011). However, these surveys mostly add to the first redshift shell ($z < 0.035$) used in the analyses and therefore are not expected to improve the constraints at the distance of the SSC or the SGW by much.

Ongoing and future SN surveys will improve the statistics at those distances, however. The Zwicky Transient Facility (ZTF[1]), a sky survey scheduled to start in 2017, is expected to find thousands of SNe Ia on the northern sky (down to declination $\delta \sim -20°$) within a few years. In addition, the Skymapper Southern Sky Survey[2], which is already in operation, is expected to add several hundred SNe in the south, which will decrease the potential bias due to an uneven distribution of data points. Furthermore, the Asteroid Terrestrial-impact Last Alert System (ATLAS[3]), which is designed to monitor the sky for hazardous asteroids, will be completed this year. During its operation it will also detect a large number of SNe at the same time.

In this chapter, the expected improvement of anisotropy results due to these new surveys will be studied by simulation.

8.1 Monte Carlo

The simulations used here are based on simple Monte Carlo approach, similar to the randomization method B used to determine p-values and the simulations of a dipole and dipole+monopole signal as used in section 6.3.

As the first step, a set of coordinates (redshift z and Galactic coordinates l, b) of the SNe is determined. In part these coordinates are taken from real data to obtain an estimate of the current capabilities. The datasets in use are the Union2.1 compilation (Suzuki et al., 2012) at $z < 0.1$ and a newer version of the SNFACTORY dataset called BEDELL, as well as the coordinates from newer data releases, viz. the second photometric data release of CSP (Stritzinger et al., 2011), CfA4 lightcurve set (Hicken et al.,

---

[1] `http://www.ptf.caltech.edu/ztf/`

[2] `http://rsaa.anu.edu.au/research/projects/skymapper-southern-sky-survey/`

[3] `http://fallingstar.com/`

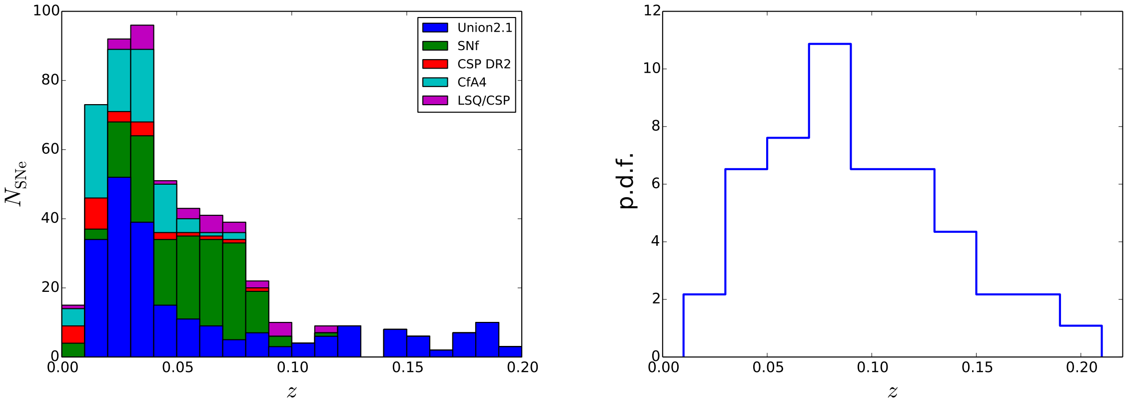

Figure 8.1: Redshift distribution of the current SN Ia datasets and probability density function (p.d.f.) of redshifts generated for the simulations. The distribution was estimated from figure 1 of Maguire et al. (2014).

2012) and the first LSQ/CSPII data release (Walker et al., in prep.). The new data were not used in the previous chapters because they were either released too recently (LSQ/CSPII) or their average redshift was to low, usually at $z < 0.04$. Therefore, these datasets would not have improved the results in the most interesting redshift shells ($0.045 < z < 0.06$ and $0.06 < z < 0.1$) greatly. Thus, the effort required to add the SNe to the compiled dataset would not have returned an adequate benefit. However, since the new data will likely be included in future compilations of the world's SN data, e.g. Union3, they should be included in the simulations. For simplicity, the coordinates of all SNe in these new datasets were included without applying any cuts, thus including more SNe than will likely make it into a compilation. This set of coordinates will from here on be referred as the *current* dataset. It consists of 419 SNe, for which the distributions of redshifts and Galactic coordinates are shown in the left panel of figure 8.1 and in figure 8.2, respectively.

To simulate future surveys, coordinates are drawn from distributions based on published PTF results. Since ZTF will be using the same telescope as PTF/iPTF, this is the best assumption to make. The redshift distribution is based on the distribution of the SNe published in Maguire et al. (2014) and is shown in the right panel figure 8.1. For the distribution of the directions, uniform distributions were used in right ascension α and the sine of the declinations $\sin(\delta)$, which leads to a uniform distribution on the sky. The declinations were limited to $-20° < \delta < 90°$, further a zone of avoidance 10° of the Milky Way, i.e. $-10° < b < 10°$, was excluded by redrawing coordinates in that region. A line of declination $\delta = -20°$ is shown in figure 8.2 for reference. In addition another set of simulations was run without the lower declination limit, thus covering the whole sky barring the Milky Way. This case can be used to assess the possible bias due to the uneven distribution of coordinates in a survey of the northern sky. In both cases new coordinates are drawn for each realization; they are not kept between runs.

The next step consists in calculating the distance moduli for a set of coordinates. Similarly to the method used in section 6.3, this is done by calculating the distance modulus for the redshifts for a fixed set of cosmological parameters. Then the distances are shifted according to one of the following velocity fields:

- **Constant bulk flow:** The velocity is set to 300 km s^{-1} towards $l = 300°$, $b = 30°$ for all SNe. This corresponds to the bulk flow observed at low redshifts. Simulating this case will allow making estimates for the uncertainties of future dipole fit analyses.

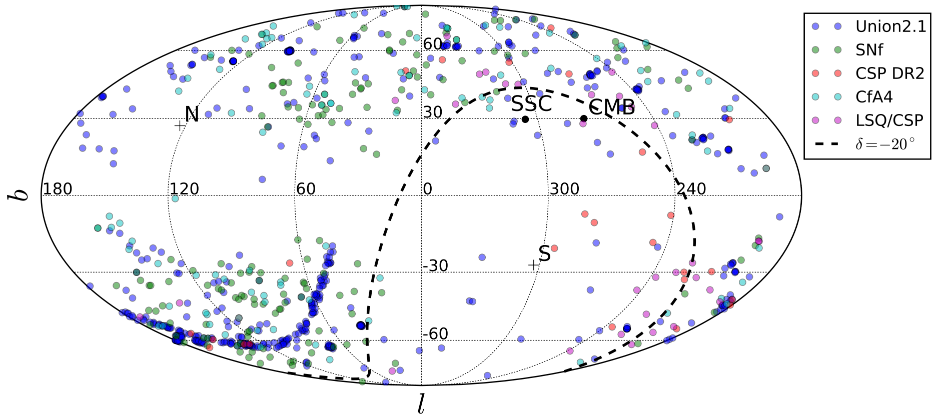

Figure 8.2: Galactic coordinates of the current SN Ia datasets. The dashed line shows the declination boundary at $\delta = -20°$ for a simulated northern survey.

- **Constant bulk flow and shear:** The velocity field is defined as in equation (5.27), consisting of a constant (dipole) velocity and a linear term defined by a symmetric (shear) tensor. The dipole velocity is set to the same value as in the first case, while the shear tensor is set to have an eigenvector in the direction of the dipole velocity with an eigenvalue $\lambda_1 = 1.5\,\mathrm{km\,s^{-1}\,Mpc^{-1}}$. The other two eigenvalues are set to $\lambda_2 = \lambda_3 = -\lambda_1/2$. This means that there is no monopole term in the velocity field and the shear corresponds the tidal field of a spherical attractor placed at a proper distance of 400 Mpc. This places the potential attractor at slightly larger distances than the SGW ($z \sim 0.1$), which can then be used to estimate potential future constraints on the shear.

- **Shapley supercluster/Sloan Great Wall:** The best-fit velocity field for a spherical attractor at $z = 0.045$ in the SSC direction and a set of superclusters around $z = 0.08$ as presented at the end of the previous chapter is used. Unlike the first two cases, the velocities are mostly low in this model except for the vicinity of the attractors. This case gives the physically most interesting results and can be used to better understand how a determination of the shear will evolve with the choice of redshift bins.

The thus determined distance moduli are then perturbed by a Gaussian with the a dispersion corresponding to their uncertainties and an additional intrinsic dispersion of 0.1 mag. For simplicity, all uncertainties are fixed to similar values. They were drawn from a Gaussian distribution with mean $\mu = 0.1$ mag and dispersion $\sigma = 0.02$ mag. To prevent too low uncertainties, values less than 0.03 mag were redrawn. Note that this dispersion is smaller than the uncertainties of some SNe, especially in the older samples of the Union2 compilation, but will on average still give a good estimate for the overall uncertainties.

Once the full dataset has been generated, the same analysis methods can be applied in the previous chapter. The analysis starts from the very beginning for each realization, i.e. with a Hubble fit without an anisotropy model, in which the intrinsic dispersion is determined. Since the result for the attractor model was used to generate the simulated data, it cannot be used for their analysis. Therefore, this chapter will only cover results for a dipole fit and a fit of a peculiar velocity tidal field. While the method of smoothed residuals would also provide good constraints, it is more complicated to interpret and compare to the simulation parameters because it does not give direct estimates of the velocity. Therefore, it was left out in this step.

8.2 Dipole Fit

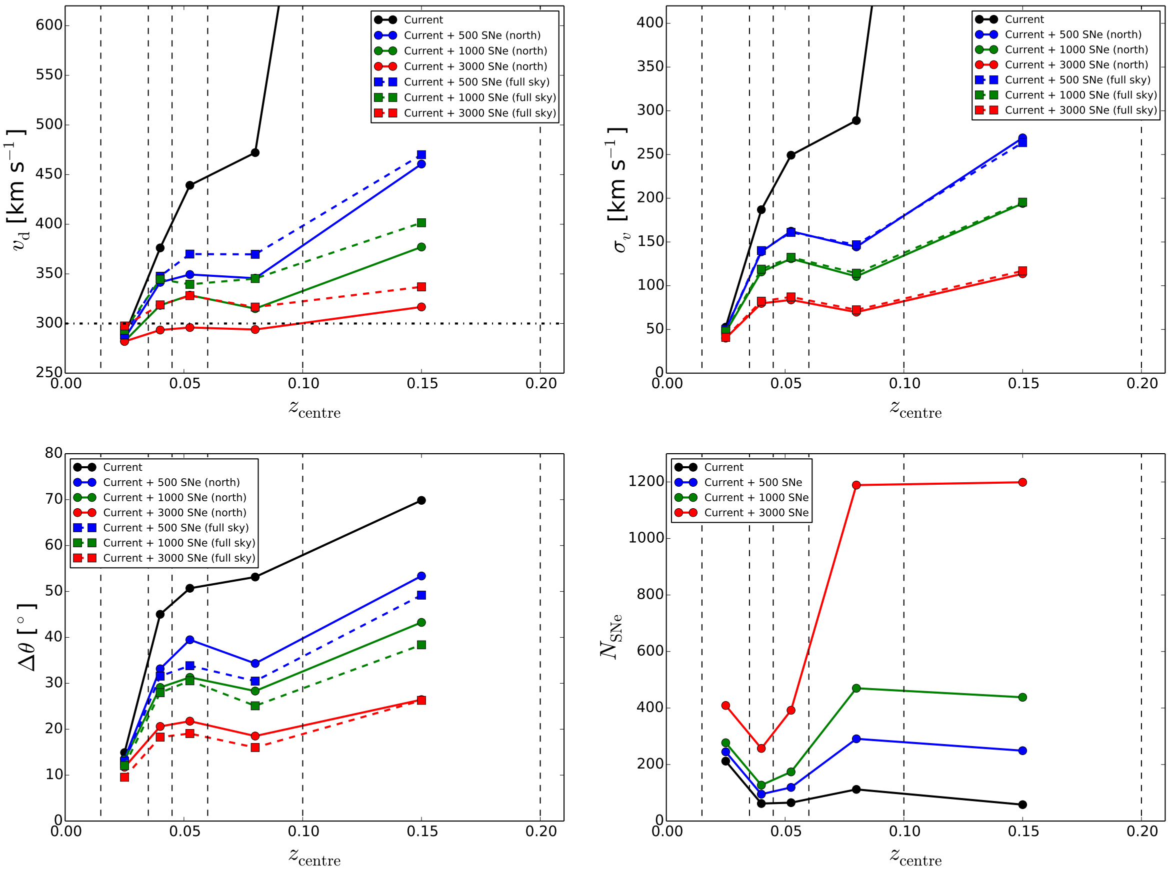

Figure 8.3: Results for a dipole fit to simulations of a constant bulk flow of 300 km s^{-1} towards (l = 300°, b = 30°) based on 1000 random realizations. The panels show the median of the reconstructed dipole velocity $v_{\rm d}$, its uncertainty σ_v, the misalignment $\Delta\theta$ of the reconstructed dipole direction to the true direction (simulation input), and the number of SNe as functions of the centre redshift $z_{\rm centre}$ of each bin. For the future surveys the results for a northern survey (declinations $\delta > -20°$) are shown as circles connected by solid line, while those for a full-sky survey are shown as squares connected by dashed lines. The velocity amplitude and its uncertainty for the last bin ($0.1 < z < 0.2$) of the current SN data are at $\sim$ 1500 km s^{-1} and $\sim$ 1700 km s^{-1}, respectively; the scale was not adjusted to show these values in order not to blur the other results. The dash-dotted horizontal line shows the input velocity amplitude of 300 km s^{-1} for reference. The dashed vertical lines show the boundaries of the redshift bins.

The dipole fit analysis was applied to 1000 realizations of the first and third simulation case listed above (constant bulk flow and SSC/SGW). The former simulation yields useful information on how well a known dipole can be reconstructed by the method, while the latter helps to better understand what velocity fields to expect for a real attractor. The data are split into redshift shells as used in section 6.1. Since ZTF is expected to find SNe at redshifts $z > 0.1$, the redshift shell at $0.1 < z < 0.2$ is included as well.

8.2.1 Constant Bulk Flow

Figure 8.3 shows the results for each simulation with a constant bulk flow. The subplots show the median[4] of the dipole amplitude, its uncertainty, the deviation of the best fit direction from the true direction ($l = 300°, b = 30°$ in this case), and the number of SNe per bin[5]. The results for the current data are only marginally better than those presented in the previous chapter. The dipole uncertainty is only $\sim 30\%$ better at best and especially in the last shell ($0.1 < z < 0.2$) the velocity is completely unconstrained with uncertainties of $\sim 1700\,\mathrm{km\,s^{-1}}$. A future survey will improve the constraints greatly in the higher-redshift shell, while the uncertainty in the first shell ($0.015 < z < 0.035$) does not decrease by much. This occurs because the assumed redshift distribution is low at redshifts $z < 0.03$ and the results at that redshift range were the most tightly constrained to begin with. With 500 additional SNe the uncertainties in the shells at redshifts $z < 0.1$ will already be reduced to $\lesssim 160\,\mathrm{km\,s^{-1}}$, vastly improving the constraints around the SSC and SGW. With the full 3000 new SNe, all dipole uncertainties reduced to $\lesssim 110\,\mathrm{km\,s^{-1}}$, which will in addition allow constraining the Dark Flow out to larger redshifts than done in this thesis and to a degree comparable to the Planck results ($\sim 130\,\mathrm{km\,s^{-1}}$, Planck Collaboration Int. XIII 2014). The effect of the uneven sky coverage of a northern sky survey can also be seen in figure 8.3. Surprisingly the reconstructed velocities match the input amplitude less well for a full-sky survey, overestimating the amplitude slightly more, even though one would expect a better sky coverage to lead to better constraints. On the other hand, the full-sky survey gives slightly better matching directions. This can be explained by looking at the results in Cartesian velocity components, which were not plotted. The median results match the input parameters better when surveying the whole sky and thus reconstruct the direction better, whereas the results are biased by $\sim 20\,\mathrm{km\,s^{-1}}$ in each coordinate for a northern survey. This bias shifts two components to smaller absolute values and one to higher values and hence the average is closer to the input values. When calculating the disagreement of the simulation results with the input velocity as the difference of the velocity vectors in Cartesian coordinates, the mismatch becomes almost the same for northern and all-sky surveys in all redshifts. It is worth noting that the median of the velocity amplitude is almost consistently larger than the input value. This is expected because the velocity amplitude is a non-linear function of the Cartesian velocity components, for which a Gaussian distribution is found in the simulations. The absolute value of the velocity, however, has a distribution that is skewed towards large values, especially if the distribution of the velocity components are very noisy (as can be seen in the correlation of large velocity amplitudes and uncertainties). Note further that this analysis did not incorporate any correlations between the SNe — which would be stronger for a northern survey due to the smaller average separation between the SNe — and therefore may not give a full picture of such an effect.

8.2.2 Shapley Supercluster/Sloan Great Wall

When using the velocity field from the fit to the SSC+SGW attractor model at the end of chapter 7, the results for the uncertainties are similar to those for a constant bulk flow, see figure 8.4. This is expected because the fit of the Cartesian components of the dipole velocity is nearly linear and thus the uncertainties do not depend strongly on the best-fit values. The best-fit velocities, on the other hand, vary with redshift as expected. When adding 3000 SNe, it is relatively stable for the first two shells and then drops for the next two shells, which cover the space in between the SSC and the SGW. Especially the fourth shell ($0.06 < z < 0.1$, with the SGW roughly in the middle between the boundaries) has a

---

[4] The mean could be used here instead of the median because the results are roughly Gaussian but some results in the next section can have strong outliers. For that reason the more robust median was consistently used to show the results.

[5] The number of SNe per bin is not fully fixed because it is drawn randomly from a redshift distribution.

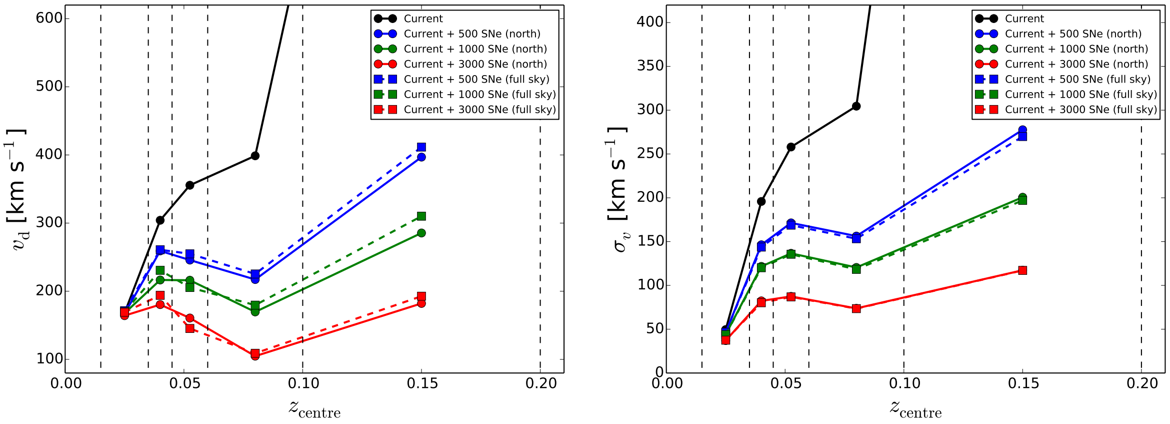

Figure 8.4: Results for a dipole fit to simulations using the velocity field based on the attractor model for the SSC and SGW used at the end of chapter 7. As in figure 8.3 the median values are plotted against the centre redshift. Since the dipole amplitude and direction are not as clearly predictable for this simulation case, no reference for the amplitude is given and the misalignment $\Delta\theta$ is not calculated. The values for the last redshift bin of the current data again are off the scale at $v_\mathrm{d} \sim 1500\,\mathrm{km\,s^{-1}}$ and $\sigma_v \sim 1700\,\mathrm{km\,s^{-1}}$.

very low velocity amplitude of $\sim 100\,\mathrm{km\,s^{-1}}$ because the SNe in front of and behind the SGW cancel out. For simulations of fewer new SNe (or none), the amplitudes are consistently larger due to the larger uncertainties making a larger best-fit amplitude more likely. Again the amplitude results for the a full-sky survey are larger than those for a northern survey but only marginally. Figure 8.5 shows the median dipole direction for both cases of 3000 additional SNe (northern and full-sky). In general, the reversal of the dipole direction due to the backside infall into the attractors is clearly visible as the direction shifts further away from the SSC direction with increasing redshift. It is noteworthy that the results in the third and fourth redshift shell are shifted further north when using SNe on the whole sky instead of northern SNe. This shifts the directions further away from the SSC, which is between us and the SNe in those shells. Therefore, a dipole pointing towards the SSC is not expected at those redshifts. Incidentally, the direction for a full-sky survey and the shell at $0.045 < z < 0.06$ matches the best-fit direction for the combined dataset in that shell (see figure 6.1).

8.3 Velocity Tidal Field

The peculiar velocity tidal field is defined by 9 parameters (1 monopole scalar, 3 dipole components, 5 components of a traceless symmetric tensor). The results for a dipole fit are already not very significant in all redshifts; even when adding 3000 SNe the uncertainties are still $\sim 100\,\mathrm{km\,s^{-1}}$ in individual redshift shells, corresponding to significances of $\lesssim 2\sigma$ for the higher-redshift shells in the SSC/SGW case. Therefore, no significant results can be expected for the tidal field if redshift shells are used. Instead the analysis of the shear is better done in cumulative redshift bins or *spheres*: the lower redshift cut at 0.015 is kept from the previous studies as minimum redshift z_min for all bins while the maximum redshift z_max is increased by step similar to those of the redshift shells. Since the SGW is located near $z = 0.08$ a step in between $z = 0.06$ and $z = 0.1$ was introduced. Similarly another step at $z = 0.15$ is added to better trace the evolution of the shear at larger distances. This approach also corresponds better to the interpretation of the tidal field as presented in section 5.4, i.e. a tidal field caused by an attractor outside the observed volume. The median numbers of SNe as a function of z_max are shown in the lower panel of figure 8.7.

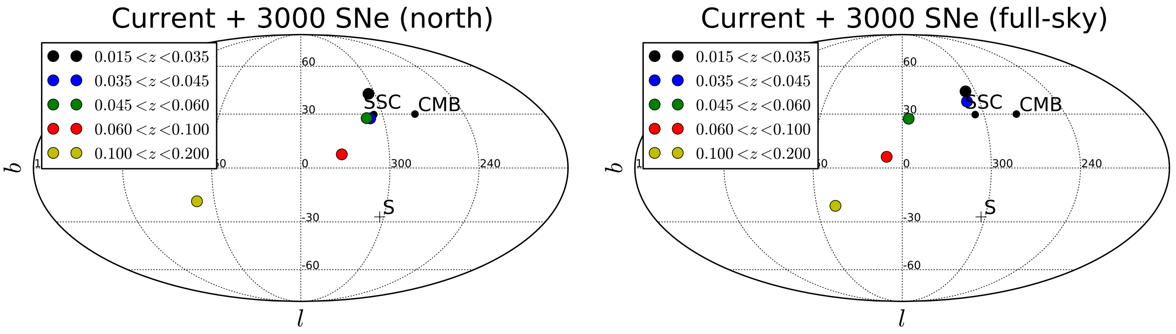

Figure 8.5: Median dipole direction for simulations of 3000 new SNe using the velocity field based on the attractor model for the SSC and SGW used at the end of chapter 7. The left and right panels show the results for survey of the northern sky and the full sky, respectively.

8.3.1 Constant Bulk Flow and Shear

For the second simulation case, in which bulk flow and shear are kept constant for all SNe, the input values are reconstructed very well, as is to be expected when the model used to simulate the data is used to fit it. The most interesting values are the dipole velocity amplitude v_d, and shear projected in the dipole direction $\tilde{\Sigma}$ and the monopole term $\tilde{H}$, which are shown in figure 8.6 along with their uncertainties. Recall that the input parameters for the simulation corresponded to $v_\mathrm{d} = 300\,\mathrm{km\,s^{-1}}$, $\tilde{\Sigma} = 1.5\,\mathrm{km\,s^{-1}\,Mpc^{-1}}$, and $\tilde{H} = 0$. The medians of the reconstructed values notably deviate to one side of the input values, with the dipole and monopole being larger and the shear lower. This deviation is still fully consistent with the input values based on the median uncertainties but especially in the case of the dipole amplitude and shear, the expectation would be that the median results are scattered around the true value and not consistently on one side. The overestimation of the dipole is consistent with that seen for the dipole fits. This deviation is due to skewed distributions of the results, which are caused by the non-linear transformation of the Cartesian components to the absolute value.

The consistently positive results for the monopole are of interest beyond the study of velocity fields because the monopole term corresponds to a local change of the Hubble constant. Therefore, a large positive monopole could explain the tension between direct measurements of the Hubble constant using a distance ladder including SNe Ia (e.g. Riess et al. 2011) and indirect measurements (e.g. using the CMB, Planck Collaboration XVI 2014. The monopole found here, however, is too small to be the sole explanation for the tension, and fully consistent with zero.

Unlike the dipole fit, the tidal field has a greater dependence on the sky coverage. This is expected because the tidal field adds terms corresponding to a quadrupole to the model, which have a better angular resolutions and are thus more sensitive to the coverage. The uncertainties for all parameters shown in figure 8.6 are smaller for full-sky surveys. For the dipole and monopole, the uncertainties for 500 SNe from a full-sky survey can even be lower than those from 1000 northern SNe.

The top row of panels in figure 8.7 shows the distance estimate R defined in section 5.4 as

$$R = \frac{2v_\mathrm{d}}{\tilde{\Sigma}}.$$

The simulation input corresponds to $R = 400\,\mathrm{Mpc}$, which is again not exactly found by the fit. Instead the distance is slightly overestimated, though still well within the uncertainties. This can be assumed to

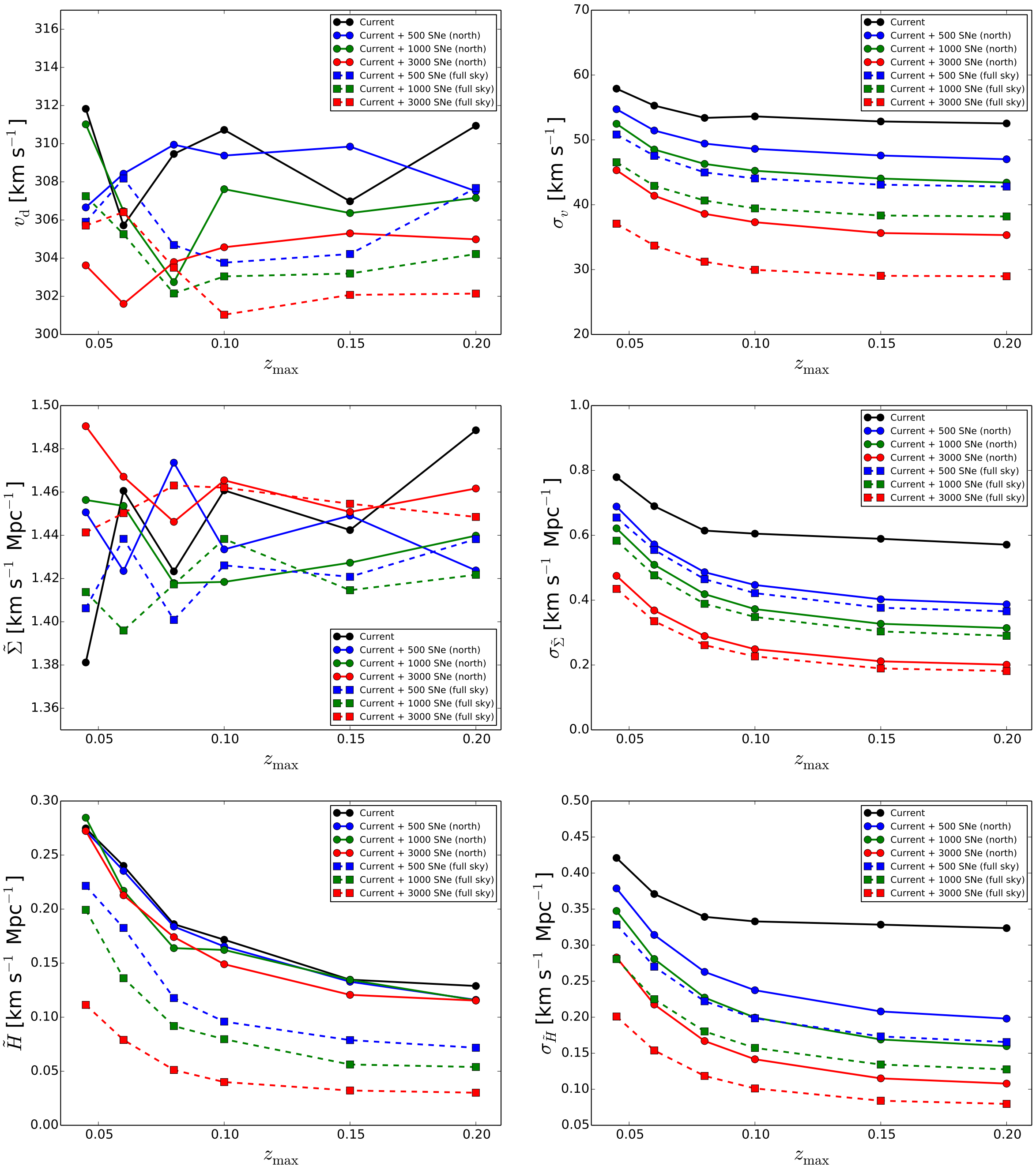

Figure 8.6: Results for a tidal field fit to simulations of a constant bulk flow of 300 km s^{-1} towards ($l = 300°, b = 30°$) and a shear corresponding to an attractor at a distance of 400 Mpc based on 1000 random realizations. The panels show the median of the reconstructed dipole velocity v_d, the shear in dipole direction $\tilde{\Sigma}$, and the monopole term $\tilde{H}$ (all in the left column) as well as their uncertainties (right column) as a function of the upper redshift cut-off z_{max}. For the future surveys the results for a northern survey (declinations $\delta > -20°$) are shown as circles connected by solid lines, while those for a full-sky survey are shown as squares connected by dashed lines.

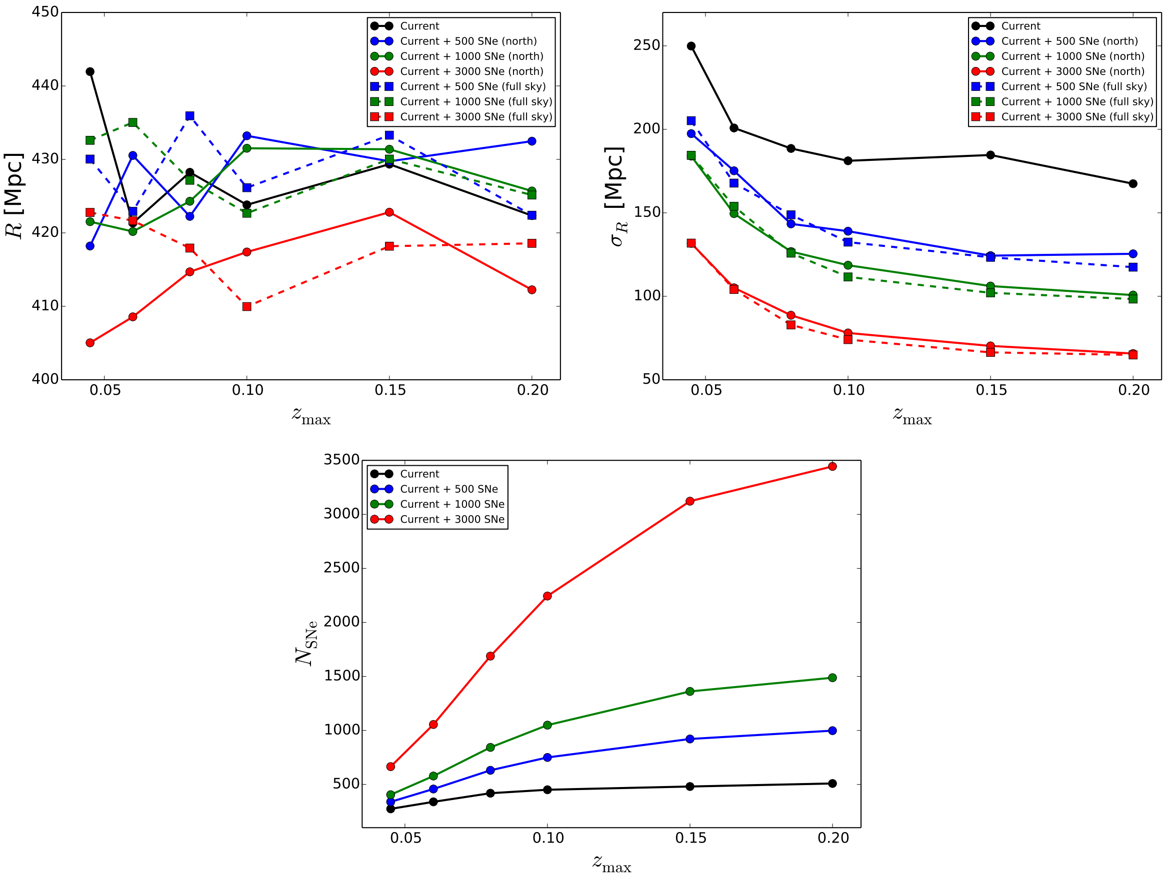

Figure 8.7: Distance estimates and number of SNe per bin for simulations of a constant bulk flow and shear as in figure 8.6. The top row of panels shows the medians of the distance estimate $R = 2v_{\mathrm{d}}/\tilde{\Sigma}$ (left) and its uncertainty as a function of the upper redshift cut-off z_{max} (right). The bottom row of plots shows the number of SNe in each bin used for the simulation.

be an effect of the combined deviations of the dipole and shear measurements and the monopole term that does not fully vanish. Recall that the distance estimate was derived assuming no monopole and changes slightly for a non-vanishing term. The uncertainties appear to be decreasing monotonously but it should be noted that this is largely due to the stability of the shear over redshift. For a lower shear the uncertainty σ_R of the distance estimate will increase along with the distance estimate itself because it is defined by

$$\sigma_R^2 = \left(\frac{2\sigma_v}{\tilde{\Sigma}}\right)^2 + \left(\frac{2v_\mathrm{d}\sigma_{\tilde{\Sigma}}}{\tilde{\Sigma}^2}\right)^2 - \frac{8v_\mathrm{d}}{\tilde{\Sigma}^3}\mathrm{Cov}(v_\mathrm{d}, \tilde{\Sigma}). \tag{8.1}$$

For a more realistic attractor, the shear is expected to decrease with distance and thus the distance estimate will become less well constrained (see below).

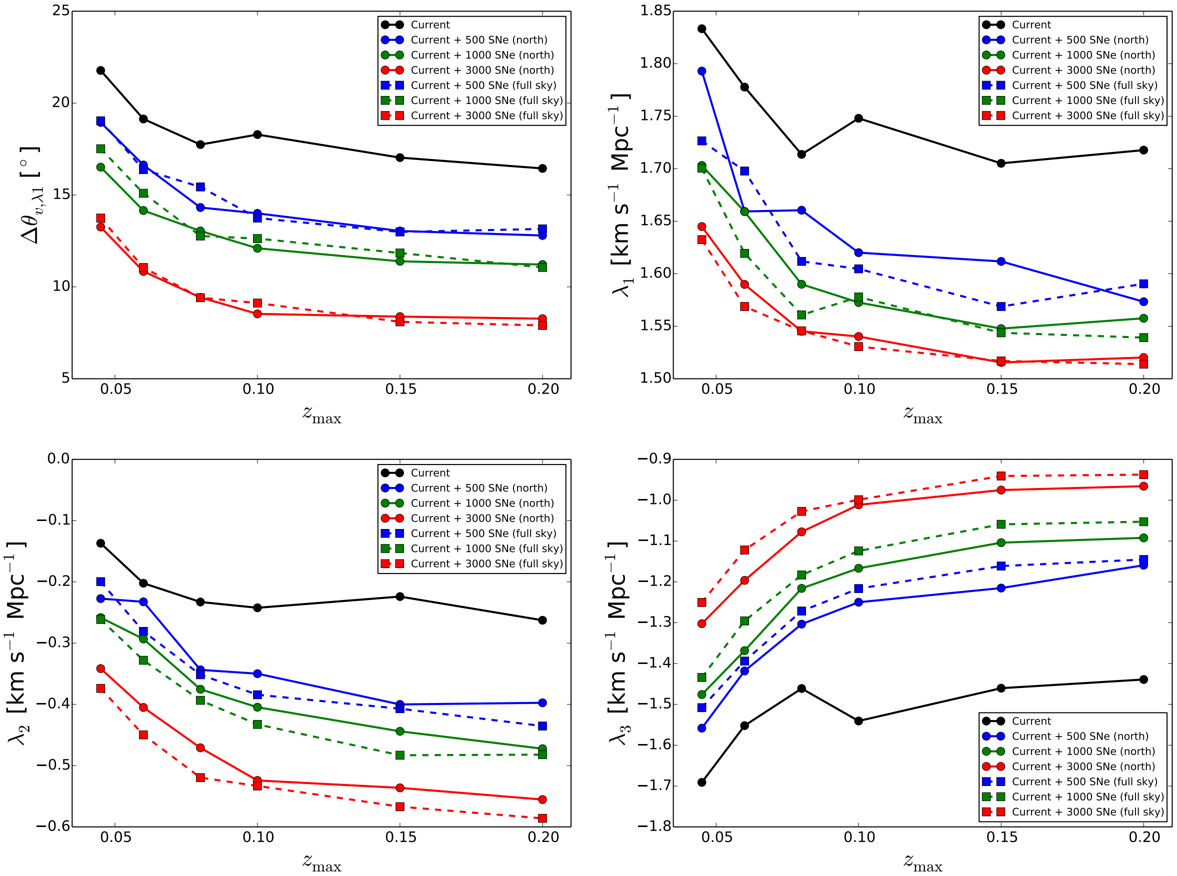

Figure 8.8: Eigenvalues of the shear matrix and number of SNe simulations of a constant bulk and shear as in figure 8.6. The panels show the median of the angle Δ_{v,λ_1} between the dipole direction and the first eigenvector, the eigenvalues λ_1, λ_2 and λ_3 as a function of the upper redshift cut-off z_{max}.

The final result of interest for the tidal field is the shape of the shear. This can be best expressed by four values: the three eigenvalues of the shear tensor and the alignment of the first eigenvector (for the largest eigenvalue) and dipole direction, see figure 8.8. The eigenvalues are sorted in descending order, i.e. $\lambda_1 > \lambda_2 > \lambda_3$, and were calculated for the traceless shear tensor, i.e. $\lambda_2 = \lambda_3 = -\lambda_1/2$. The simulation input values were to $\lambda_1 = 1.5\,\mathrm{km\,s^{-1}\,Mpc^{-1}}$ and $\lambda_2 = \lambda_3 = -0.75\,\mathrm{km\,s^{-1}\,Mpc^{-1}}$ with the first eigenvector aligned with the dipole. The fit results show a misalignment of $\sim 20°$ for the current data, which decreases to < 10° for the 3000 addition SNe in spheres above redshift 0.08. The first eigenvalue λ_1, which would be expected to be similar to the shear in bulk flow direction, shows a deviation to the other side of the true value. Hence, the deviation of the shear is a combined effect of the misaligned eigenvector and the overestimated eigenvalues. Lastly, the ratio of the other two eigenvalues gives a estimate of the shear's rotational symmetry around the axis defined by the first eigenvector. While λ_2 is almost zero for the current data, the values are much closer to λ_3 for larger statistics. Here it is important to remember that $\lambda_2 > \lambda_3$ is strictly enforced by sorting the eigenvalues. Therefore, the remaining deviation for 3000 additional SNe is only marginal.

8.3.2 Shapley Supercluster/Sloan Great Wall

As noted above, the previous simulation case had extremely well fitting results because the same model was used for simulation and fit. Although this case is still useful for understanding the limitations of the tidal field, a more realistic model is required to make predictions for future surveys. This can be achieved by the third simulation case, which is based on the SSC/SGW attractor model from the end of chapter 7. The results for dipole, shear, and monopole and their uncertainties are shown in figure 8.9. As for the comparison of the different simulation cases for the dipole fits in the previous section, the uncertainties are very similar to those of the simulation for constant bulk flow and shear. The full-sky surveys again lead to smaller uncertainties and the best-fit values now show some evolution with redshift. In case of the monopole this is only a small decrease in the median around the attractor redshift, which is completely marginal, since the values are scattered around zero. Therefore, a monopole from a massive attractor is even less likely as an explanation for the tension of the Hubble constant measurements.

The results for the dipole amplitude and the shear in dipole direction decrease with redshift. This is expected since the relative number of SNe affected by the attractors decreases for larger spheres and the velocities become dominated by noise. This had not been the case for the simulation of a constant bulk flow and shear, which applied similar velocities to all SNe. It is worth noting that the values at large distances decrease slightly faster for the full-sky survey than for a northern one.

A better understanding of the tidal field, however, can be derived from the distance estimate R shown in figure 8.10. In general, the distance to the attractor is overestimated; the SGW is located at a proper distance of $\sim 300\,\mathrm{Mpc}$. The more interesting result is the evolution of the distance estimate. Although it increases for all simulations, the slope becomes larger the more SNe are added. However, this only occurs above a certain redshift. Up to $z_{\max} = 0.08$ the values for R are much closer to each other; above it they begin to diverge at a higher rate. Similarly the uncertainties of R increase drastically between $z_{\max} = 0.08$ and 0.1 . This is especially apparent when adding 3000 SNe to the data: the uncertainties are almost constant up to 0.08 and then rise to values large than those for smaller surveys. This is the effect as predicted above, in which the shear drops quickly behind the attractors where no coherent motion is found and since R is anti-proportional to the shear, its uncertainty rapidly increases.

The study of the shape of shear tensor leads to similar conclusions, see figure 8.11. Even though the alignment of dipole and first shear eigenvector is clearly worse than for the constant bulk flow and shear simulation, it is markedly lower for 3000 additional SNe up to $z_{\max} = 0.08$. For larger spheres the direction of the eigenvector then deviates much stronger from the dipole direction. Again this occurs because the average motion behind the attractor becomes less coherent. The eigenvalues show a less symmetric shear than for the previous example, with λ_2 being closer to zero. Additionally λ_1 and λ_3 both approach zero for larger $z_{\max}$, again matching the decrease in shear for spheres extending beyond the attractor.

In conclusion these simulations of tidal field fits to the SSC/SGW attractor system suggest that while the distance estimate R does not estimate the distance to the attractor all that well, its evolution with $z_{\max}$

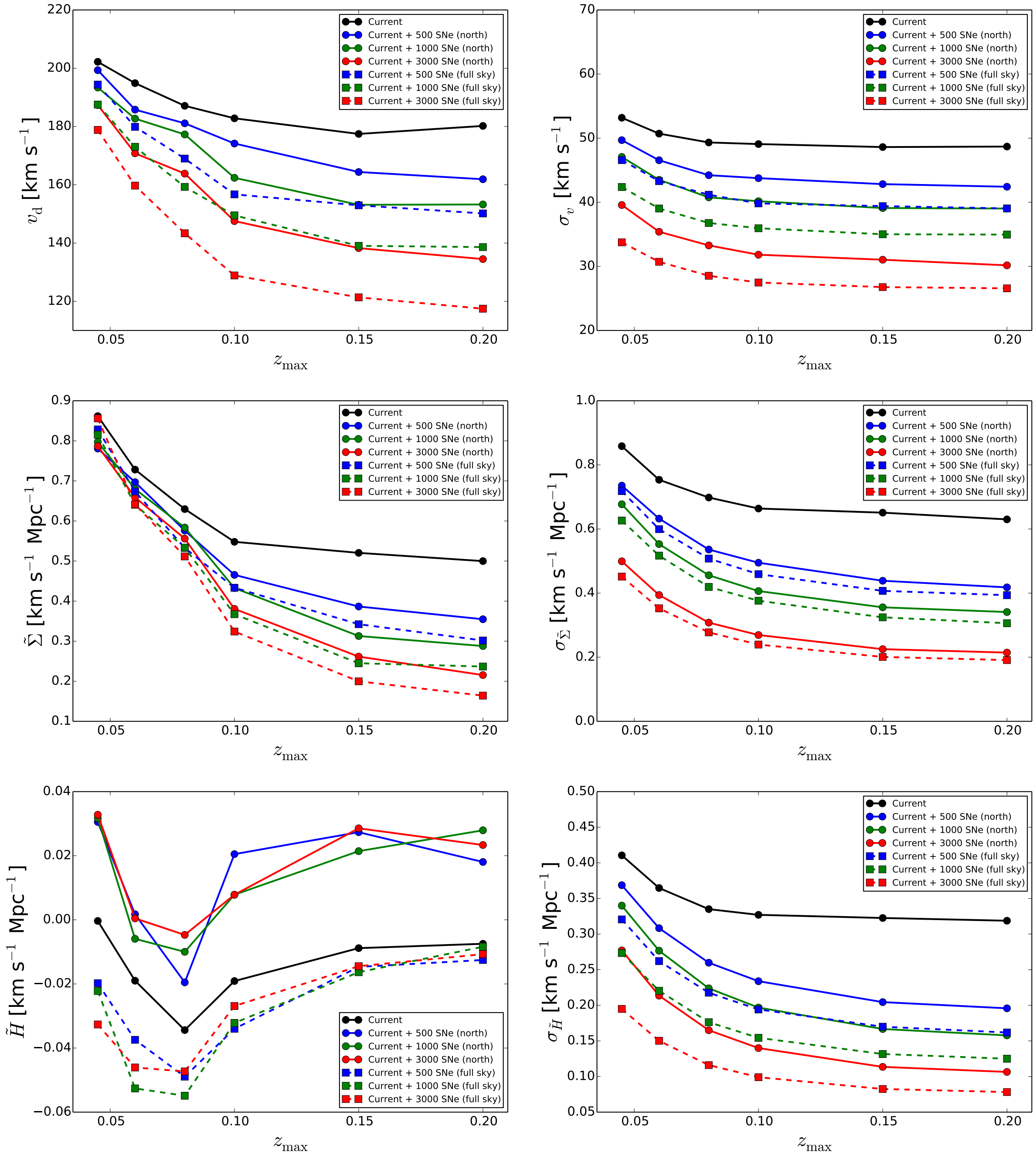

Figure 8.9: Results for a tidal field fit to simulations using the velocity field based on the attractor model for the SSC and SGW used at the end of chapter 7. The panels show the median of the reconstructed dipole velocity v_d, the shear in dipole direction $\tilde{\Sigma}$, and the monopole term $\tilde{H}$ (all in the left column) as well as their uncertainties (right column) as a function of the upper redshift cut-off z_{max}.

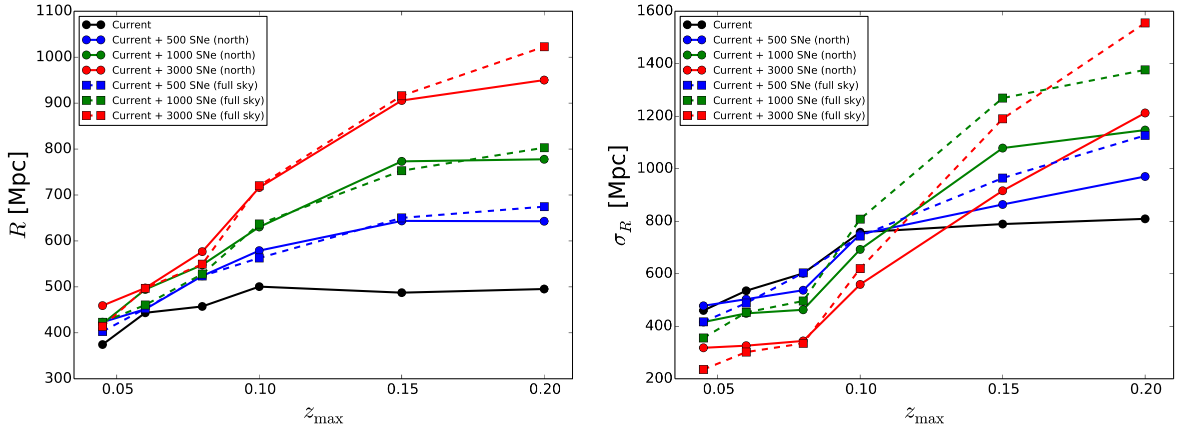

Figure 8.10: Distance estimates for simulations of a velocity field as in figure 8.9. The left panels shows the medians of the distance estimate $R = 2v_\mathrm{d}/\tilde{\Sigma}$ as a function of the upper redshift cut-off $z_{\max}$, while the right one shows its uncertainty.

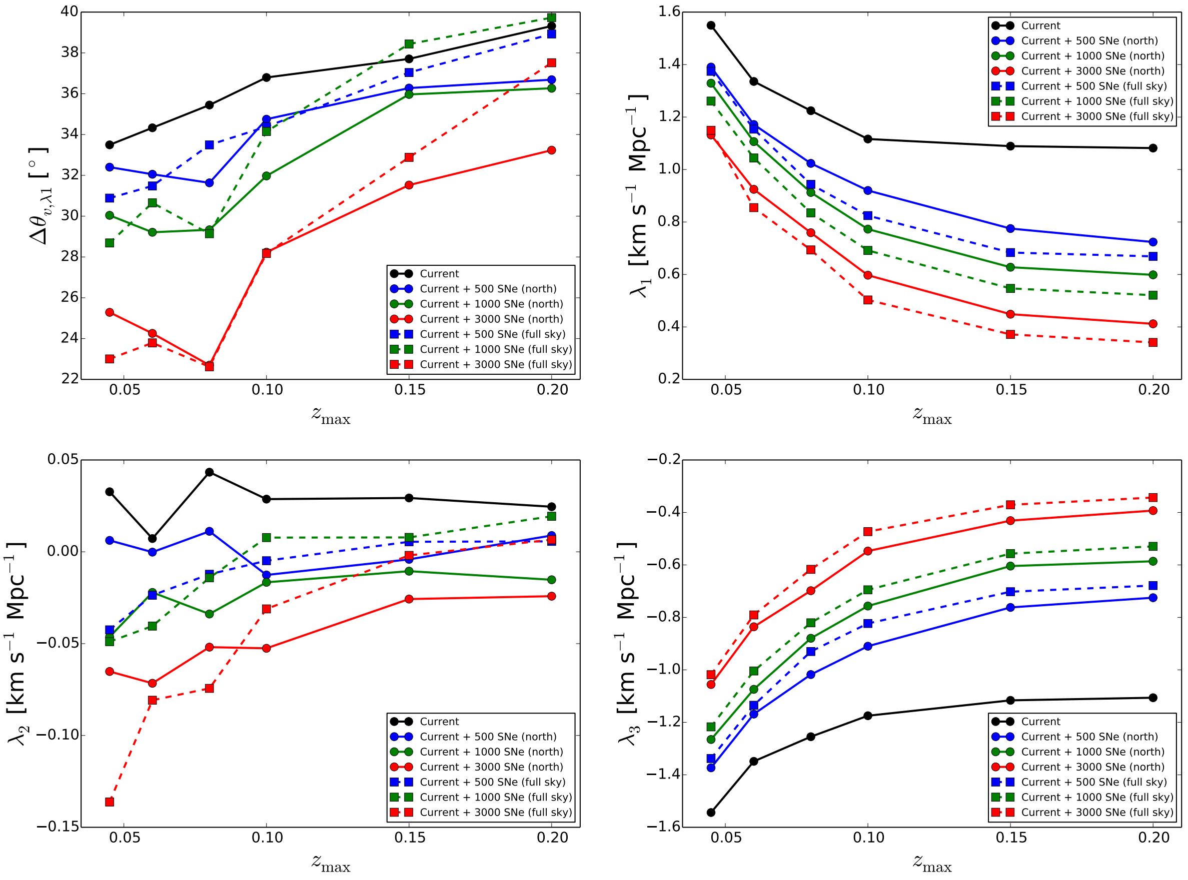

Figure 8.11: Distance estimates for simulations of a velocity field as in figure 8.9. The panels show the median of the angle Δ_{v,λ_1} between the dipole direction and the first eigenvector, and the eigenvalues λ_1, λ_2 and λ_3 as a function of the upper redshift cut-off $z_{\max}$.

can indicate the location of the attractor. This can be found based on a sharp increase in uncertainty if data behind the attractor is included in the fit. That way the location of the attractor can be constrained by this model-independent approach which will then justify a more model-dependent investigation such as a gravitational attractor model.

8.4 Conclusions

The simulation results presented in this chapter have demonstrated the potential of supernovae in the intermediate redshift range between 0.05 and 0.1. This bears implications for the planning of future SN surveys in this redshift range, e.g. ZTF, and possible follow-up programmes that provide lightcurve points at more phases and in more filters than the survey telescope can.[6] Observations of SNe at larger distances will have a lower signal-to-noise ratio at the same exposure times, and thus one must weigh the gain in higher-redshift data against the potential loss in quality for the individual data points.

Based on the assumed redshift distribution (see figure 8.1) $\sim 40\%$ of the discovered SNe are expected in the redshift shell $0.06 < z < 0.1$, in which the dark flow has been reported (Kashlinsky et al., 2010). The simulations of the dipole fit have shown that observations of ~ 200 of the SNe in that shell (as from the simulation for 500 additional SNe) could rule out a dark flow of $1000\,\mathrm{km\,s^{-1}}$ in any direction at more than 6σ. Therefore, ZTF could potentially solve these open questions soon after its start, if SNe at redshifts beyond $z > 0.05$ are followed. A detection of the shear, on the other hand, will likely require ~ 1000 new SNe in that redshift range. Since the shear from a SSC/SGW attractor would decrease at redshifts beyond $z = 0.08$, SN data up to $z = 0.1$ may suffice to study this attractor because they could detect both the expected decline in shear and a backside infall.

Furthermore, it is worth noting that SNe at lower redshifts do not have the same relative potential for bulk flow studies because the galaxy data on these smaller scale will continue to grow due to future all-sky Tully-Fisher and Fundamental Plane surveys, e.g. TAIPAN[7] or WALLABY[8]. Even though these surveys will extend to $z \sim 0.1$, their main weight still lies at lower redshifts and SNe Ia will remain the best peculiar velocity probes in this range.

Future constraints on the masses of the SSC/SGW attractor structures – which were not simulated here – will also benefit from new SNe Ia at redshifts $z > 0.05$ because they could trace the backside infall to the SSC or the SGW. However, this model requires SNe closer to the attractors and a survey based on the northern hemisphere such as ZTF (at Mount Palomar, USA; latitude 33.36° N) will thus only be able to observe the SGW (declination $\delta \sim 0°$) well. The SSC ($\delta \sim -30°$), on the other hand, will only be visible in spring and never rise more than 30° above the horizon, so only SNe on its northern fringes may be observable. Superclusters further south, e.g. Horologium-Reticulum ($\delta \sim -50°$), will not be observable from the north at all. In order to study them, SN Ia data from a southern survey such as Skymapper will be required to complement the northern sample.

---

[6] The possibility of such a follow-up programme using the STELLA Robotic Observatory on Tenerife (`http://www.aip.de/en/research/facilities/stella/stella-robotic-observatory`) is currently being investigated.

[7] `http://www.taipan-survey.org/`

[8] `http://www.atnf.csiro.au/research/wallaby/`

CHAPTER 9

Summary and Outlook

In this thesis, open questions regarding the anisotropy and peculiar velocities in the local universe were investigated, in particular the properties of anomalous bulk flows reported by previous studies and the effect of the SSC on the local peculiar velocities. These questions were studied using SN Ia data from two independent samples: the Union2 compilation and a dataset of 117 SNe from the SNFACTORY. The latter sample provides SNe in redshift range $0.03 < z < 0.08$, where the larger Union2 sample lacks data. This range covers important structures in the local universe including the SSC and therefore provides the optimal dataset to investigate their contribution to the bulk flow.

Dipole Fit and Smoothed Residuals We first analysed the data using a velocity dipole model and two methods of smoothed Hubble residuals. For each method the data were separated into concentric redshift shells to trace the evolution of the bulk flow and anisotropy with redshift. Two methods of randomization – one shuffling the coordinates of the SNe, the other applying random noise to the null hypothesis of isotropy – were used to determine the significance of the detected signals. The key results for these methods are:

- In the lowest redshift shell ($0.015 < z < 0.035$), the bulk direction is compatible with both the direction of LG motion and the SSC and the amplitude does not exceed the expectation from ΛCDM. It matches the results of previous studies, which found bulk flows of $\sim 250\,\mathrm{km\,s^{-1}}$, with a p-value of 0.03. For the smoothed residuals methods the results are slightly less significant with p-values between 0.05 and 0.065. These results are based mostly in the Union2 data that dominates the dataset in this shell.

- In the intermediate shell ($0.035 < z < 0.045$), only the normalized smoothed residuals method finds a weak anisotropy with p-values around 0.18. However, this method is found to be susceptible to the monopole term found in this shell.

- The third redshift shell ($0.045 < z < 0.06$) contains SNe located behind the SSC. The tentative backside infall seen in the Union2 data is shown to be caused by SNe in the other side of the sky that should not be influenced by the SSC. A significant ($p = 0.04$) bulk flow in a direction compatible with the SSC and CMB dipole is detected in the SNFACTORY data alone in this shell but in combination, the datasets show no significant anisotropy. While this finding does not fully rule out a small backside infall, it refutes previous studies that found it in the Union2 sample.

- The redshift shell at ($0.06 < z < 0.1$) extends to distances, at which an anomalously large bulk flows of $\sim 1000\,\mathrm{km\,s^{-1}}$ have been reported, the "dark flow". The dipole is found to be fully consistent with the null hypothesis here and limited to $400\,\mathrm{km\,s^{-1}}$ for all directions. When restricting the dipole direction to that of this dark flow, the amplitude is constrained to $250\,\mathrm{km\,s^{-1}}$, ruling the reported values out at $\sim 4\sigma$.

- For redshifts $z > 0.1$, the uncertainties on peculiar velocities of individual SNe become too large to detect bulk flows or make any claim regarding anisotropy.

- At all scales analysed in this study, the statistical uncertainties dominate over the systematic uncertainties and except for a few cases the different analysis methods find consistent significances.

Gravitational Attractor Since the dipole fit and smoothed residual methods found no evidence for a backside infall in to the SSC, a gravitational attractor model was used to constrain the mass required to explain the observed peculiar velocities of the SNe. The attractor was modelled as a spherical overdensity of constant density contrast. Although this model is too simple to perfectly model the local velocity field in the local universe, its use is justified by the current size of the SN Ia datasets; cosmography studies that reconstruct the flow of galaxies to greater detail rely on catalogues of $> 10\,000$ galaxies (Courtois et al., 2013).

For a single attractor placed at the redshift of the SSC and in its direction, the reconstructed mass exceeds previous estimates by $\sim 50\%$ based on independent methods. When varying the redshift of the overdensity, a more massive attractor at $z = 0.1$ is favoured at $\sim 2\sigma$, showing that a continuing bulk flow fits the data better than a converging flow with a backside infall. However, this result shows some dependence on the direction to the attractor. When allowing the direction to vary along with the mass while keeping the redshift fixed, directions up to $\sim 25°$ away from that of the SSC are favoured and generally give a marginally better fit quality than the a bulk flow. The best-fitting redshift for this approach is around $z \sim 0.062$ but the χ^2-profile is very flat in z and thus does not give tight constraints on the distance to the attractor.

Since the single attractor model indicates that the SSC has insufficient mass to explain the bulk flow and independent mass estimates exist, the attractor fit was repeated including a fixed overdensity corresponding to the SSC. Even though the fit results do not change significantly, the mass found at redshift $z \sim 0.08$ is consistent with that of the Sloan Great Wall (SGW). The best-fit directions around this redshift are also located between the SSC and the SGW, further indicating its contribution to the bulk flow. Since the SGW is strongly elongated and thus cannot be modelled as a spherical attractor, a list of superclusters in its region was used to describe its effect on the peculiar velocities. Mass estimates from this model are consistent with those found by previous studies, but are not very well constrained, especially in the case of the SGW. In general, the results of the attractor model should be considered tentative because the velocity field originates from a complicated interplay of the whole structure in the local universe. Out of necessity, several mass concentrations known to contribute to the LG motion to a lesser degree could not be investigated here. For instance, the Vela and Horologium-Reticulum superclusters were not accessible with the current dataset, since they are located behind the Milky Way and too far south, respectively.

Simulations for Future Surveys As a final analysis, simulations of future SN surveys were run to assess their prospect for peculiar velocity studies. Only models for the bulk flow and a tidal field that also contains shear and monopole components were used, whereas the results of the attractor fit to SSC and SGW were used as an input to test against. The simulations showed that 500 additional SNe with a redshift distribution similar to that of PTF, will allow constraints on the dark flow at better levels than the current Planck results of $\lesssim 250\,\mathrm{km\,s^{-1}}$ (95% confidence level). The possible backside infall behind the SSC and SGW is also expected to become visible as a significant reversal of the dipole direction in the shells at larger redshifts.

The simulations for the peculiar velocity tidal field show that even with 1000 additional SNe at redshifts $0.05 < z < 0.1$, i.e./ in the distance range of the SSC and SGW, the shear caused by them will only be detectable at $\sim 2\sigma$. This limits the feasibility of using the ratio of bulk flow and shear as a proposed model-independent estimate for the distance to the main attractor(s). However, the evolution of this estimator for growing spheres of observed SNe may provide good constraints for the attractor location and thereby motivate a more restricted search for significant mass concentrations. The simulation used a redshift distribution that extended far beyond the SGW and only about half of the simulated SNe were at $z < 0.1$. Based on our current understanding of the attractors, SNe at $z > 0.1$ will not be required for an analysis of the structure, since they are not expected to improve the masses constraints for SSC and SGW by much. However, they may still help to constrain the dark flow at larger distances than shown here.

Outlook The analyses presented in this thesis demonstrate the ability of SNe Ia to investigate the open questions regarding the local bulk flows and the SSC. Compared to previous studies, the SNFACTORY has more than doubled the number of available SNe in the redshift range from 0.03 to 0.08. This bridges the gap between local bulk flow measurements using the distances of galaxies and measurement on larger scales using the kSZ effect in galaxy clusters. The continuously growing number SNe from active and future survey, e.g. Skymapper and ZTF, will settle these open issues in the near future.

Furthermore peculiar velocities from SNe Ia will also become competitive as probes of the statistics of structure formation, by measuring the peculiar velocity power spectrum. Measurements of the power spectrum based on the distribution of galaxies are dependent on the relation between the observable light and the underlying matter distribution. Using peculiar velocities, which directly trace the matter distribution, removes this requirement. For galaxies this has recently been demonstrated using ~ 9000 distances based on the Fundamental Plane from the Six-degree-Field Galaxy Survey (6dFGS) (Johnson et al., 2014), and will be further extended by peculiar velocity surveys such as TAIPAN or WALLABY (see Koda et al. 2014). Since SN distances can be measured up to five times more precisely, a sample of 1000 SNe may have the statistical weight of 25 000 galaxies. The larger mean separation between the data points will limit their constraining power for the small scales, but SNe Ia from the upcoming surveys can be expected to contribute significantly to the measurement of the power spectrum at larger scales.

Bibliography

Aldering, G., Adam, G., Antilogus, P., et al. 2002, in Society of Photo-Optical Instrumentation Engineers (SPIE) Conference Series, Vol. 4836, Survey and Other Telescope Technologies and Discoveries, ed. J. A. Tyson & S. Wolff, 61–72

Aldering, G., Antilogus, P., Bailey, S., et al. 2006, ApJ, 650, 510

Amanullah, R., Lidman, C., Rubin, D., et al. 2010, ApJ, 716, 712

Appleby, S. & Shafieloo, A. 2014, J. Cosmology Astropart. Phys., 3, 7

Appleby, S., Shafieloo, A., & Johnson, A. 2015, ApJ, 801, 76

Astier, P., Guy, J., Regnault, N., et al. 2006, A&A, 447, 31

Atrio-Barandela, F. 2013, A&A, 557, A116

Atrio-Barandela, F., Kashlinsky, A., Ebeling, H., Fixsen, D. J., & Kocevski, D. 2015, A&A, submitted [`arXiv:1411.4180`]

Atrio-Barandela, F., Kashlinsky, A., Ebeling, H., Kocevski, D., & Edge, A. 2010, ApJ, 719, 77

Bailey, S., Aldering, G., Antilogus, P., et al. 2009, A&A, 500, L17

Balland, C., Baumont, S., Basa, S., et al. 2009, A&A, 507, 85

Baltay, C., Rabinowitz, D., Andrews, P., et al. 2007, PASP, 119, 1278

Baltay, C., Rabinowitz, D., Hadjiyska, E., et al. 2013, PASP, 125, 683

Barris, B. J., Tonry, J. L., Blondin, S., et al. 2004, ApJ, 602, 571

Betoule, M., Kessler, R., Guy, J., et al. 2014, A&A, 568, A22

Blakeslee, J. P., Ajhar, E. A., & Tonry, J. L. 1999, Post-Hipparcos Cosmic Candles, 237, 181

Bongard, S., Soulez, F., Thiébaut, É., & Pecontal, É. 2011, MNRAS, 418, 258

Bonvin, C., Durrer, R., & Gasparini, M. A. 2006a, Phys. Rev. D, 73, 023523

Bonvin, C., Durrer, R., & Kunz, M. 2006b, Physical Review Letters, 96, 191302

Buton, C., Copin, Y., Aldering, G., et al. 2013, A&A, 549, A8

Cardelli, J. A., Clayton, G. C., & Mathis, J. S. 1989, ApJ, 345, 245

Chandrasekhar, S. 1931, MNRAS, 91, 456

Chandrasekhar, S. 1935, MNRAS, 95, 207

Childress, M., Aldering, G., Antilogus, P., et al. 2013a, ApJ, 770, 107

Childress, M., Aldering, G., Antilogus, P., et al. 2013b, ApJ, 770, 108

Chotard, N., Gangler, E., Aldering, G., et al. 2011, A&A, 529, L4

Colin, J., Mohayaee, R., Sarkar, S., & Shafieloo, A. 2011, MNRAS, 414, 264

Conley, A., Carlberg, R. G., Guy, J., et al. 2007, ApJ, 664, L13

Copin, Y. 2013, Habilitation à diriger des recherches, Université de Lyon 1

Courteau, S., Willick, J. A., Strauss, M. A., Schlegel, D., & Postman, M. 2000, ApJ, 544, 636

Courtois, H. M., Pomarède, D., Tully, R. B., Hoffman, Y., & Courtois, D. 2013, AJ, 146, 69

da Costa, L. N., Geller, M. J., Pellegrini, P. S., et al. 1994, ApJ, 424, L1

Dai, D.-C., Kinney, W. H., & Stojkovic, D. 2011, J. Cosmology Astropart. Phys., 4, 15

Davis, M., Nusser, A., Masters, K. L., et al. 2011a, MNRAS, 413, 2906

Davis, T. M., Hui, L., Frieman, J. A., et al. 2011b, ApJ, 741, 67

Djorgovski, S. & Davis, M. 1987, ApJ, 313, 59

Dressler, A., Lynden-Bell, D., Burstein, D., et al. 1987, ApJ, 313, 42

Ebeling, H., Mullis, C. R., & Tully, R. B. 2002, ApJ, 580, 774

Einasto, M., Liivamägi, L. J., Tempel, E., et al. 2011, ApJ, 736, 51

Einstein, A. 1917, Sitzungsberichte der Königlich Preußischen Akademie der Wissenschaften (Berlin), Seite 142-152., 142

Erdoğdu, P., Lahav, O., Huchra, J. P., et al. 2006, MNRAS, 373, 45

Faber, S. M. & Jackson, R. E. 1976, ApJ, 204, 668

Feindt, U., Kerschhaggl, M., Kowalski, M., et al. 2013, A&A, 560, A90

Feindt, U., Kerschhaggl, M., Kowalski, M., et al. 2015, A&A, 578, C1 (Corrigendum to Feindt et al. 2013)

Feldman, H. A., Watkins, R., & Hudson, M. J. 2010, MNRAS, 407, 2328

Friedmann, A. 1922, Zeitschrift für Physik, 10, 377

Frieman, J. A., Bassett, B., Becker, A., et al. 2008, AJ, 135, 338

Gordon, C., Land, K., & Slosar, A. 2007, Physical Review Letters, 99, 081301

Gordon, C., Land, K., & Slosar, A. 2008, MNRAS, 387, 371

Grishchuk, L. P. & Zeldovich, I. B. 1978, Soviet Ast., 22, 125

Gurovich, S., Freeman, K., Jerjen, H., Staveley-Smith, L., & Puerari, I. 2010, AJ, 140, 663

Guy, J., Sullivan, M., Conley, A., et al. 2010, A&A, 523, A7

Guy, J. et al. 2005, A&A, 443, 781

Guy, J. et al. 2007, A&A, 466, 11

Hadjiyska, E., Rabinowitz, D., Baltay, C., et al. 2012, in IAU Symposium, Vol. 285, IAU Symposium, ed. E. Griffin, R. Hanisch, & R. Seaman, 324–326

Hadjiyska, E. I., Cenko, B., Miller, B. P., et al. 2013, in American Astronomical Society Meeting Abstracts, Vol. 221, American Astronomical Society Meeting Abstracts #221, 439.10

Hamuy, M., Folatelli, G., Morrell, N. I., et al. 2006, PASP, 118, 2

Hamuy, M., Phillips, M. M., Suntzeff, N. B., et al. 1996a, AJ, 112, 2391

Hamuy, M., Phillips, M. M., Suntzeff, N. B., et al. 1996b, AJ, 112, 2391

Hamuy, M. et al. 1996c, AJ, 112, 2398

Harrison, E. R. 1974, ApJ, 191, L51

Haugbølle, T., Hannestad, S., Thomsen, B., et al. 2007, ApJ, 661, 650

Hernández-Monteagudo, C., Ma, Y.-z., Kitaura, F.-S., et al. 2015, A&A, submitted [`arXiv:1504.04011`]

Hicken, M., Challis, P., Kirshner, R. P., et al. 2012, ApJS, 200, 12

Hicken, M., Wood-Vasey, W. M., Blondin, S., et al. 2009a, ApJ, 700, 1097

Hicken, M. et al. 2009b, ApJ, 700, 1097

Hillebrandt, W. & Niemeyer, J. C. 2000, ARA&A, 38, 191

Hoffman, Y., Eldar, A., Zaroubi, S., & Dekel, A. 2001, ArXiv Astrophysics e-prints [`arXiv:astro-ph/0102190`]

Hogg, D. W. 1999, ArXiv Astrophysics e-prints [`arXiv:astro-ph/9905116`]

Holtzman, J. A., Marriner, J., Kessler, R., et al. 2008, AJ, 136, 2306

Howell, D. A., Sullivan, M., Perrett, K., et al. 2005, ApJ, 634, 1190

Hubble, E. 1929, Proceedings of the National Academy of Science, 15, 168

Hudson, M. J., Smith, R. J., Lucey, J. R., & Branchini, E. 2004, MNRAS, 352, 61

Hui, L. & Greene, P. B. 2006, Phys. Rev. D, 73, 123526

Jerjen, H. & Tammann, G. A. 1993, A&A, 276, 1

Jha, S., Riess, A. G., & Kirshner, R. P. 2007, ApJ, 659, 122

Johnson, A., Blake, C., Koda, J., et al. 2014, MNRAS, 444, 3926

Kaiser, N. 1987, MNRAS, 227, 1

Kaiser, N. 1991, ApJ, 366, 388

Kaiser, N. & Hudson, M. J. 2015, MNRAS, 450, 883

Kalus, B., Schwarz, D. J., Seikel, M., & Wiegand, A. 2013, A&A, 553, A56

Kasen, D., Röpke, F. K., & Woosley, S. E. 2009, Nature, 460, 869

Kashlinsky, A. & Atrio-Barandela, F. 2000, ApJ, 536, L67

Kashlinsky, A., Atrio-Barandela, F., & Ebeling, H. 2012, ArXiv e-prints [`arXiv:1202.0717`]

Kashlinsky, A., Atrio-Barandela, F., Ebeling, H., Edge, A., & Kocevski, D. 2010, ApJ, 712, L81

Kashlinsky, A., Atrio-Barandela, F., Kocevski, D., & Ebeling, H. 2008, ApJ, 686, L49

Kashlinsky, A., Atrio-Barandela, F., Kocevski, D., & Ebeling, H. 2009, ApJ, 691, 1479

Keisler, R. 2009, ApJ, 707, L42

Kelly, P. L., Hicken, M., Burke, D. L., Mandel, K. S., & Kirshner, R. P. 2010, ApJ, 715, 743

Kessler, R., Becker, A. C., Cinabro, D., et al. 2009, ApJS, 185, 32

Knop, R. A., Aldering, G., Amanullah, R., et al. 2003, ApJ, 598, 102

Kocevski, D. D. & Ebeling, H. 2006, ApJ, 645, 1043

Kocevski, D. D., Ebeling, H., Mullis, C. R., & Tully, R. B. 2007, ApJ, 662, 224

Koda, J., Blake, C., Davis, T., et al. 2014, MNRAS, 445, 4267

Kogut, A., Lineweaver, C., Smoot, G. F., et al. 1993, ApJ, 419, 1

Kowalski, M., Rubin, D., Aldering, G., et al. 2008, ApJ, 686, 749

Kraan-Korteweg, R. C., Woudt, P. A., Cayatte, V., et al. 1996, Nature, 379, 519

Lampeitl, H., Smith, M., Nichol, R. C., et al. 2010, ApJ, 722, 566

Lantz, B., Aldering, G., Antilogus, P., et al. 2004, in Society of Photo-Optical Instrumentation Engineers (SPIE) Conference Series, Vol. 5249, Optical Design and Engineering, ed. L. Mazuray, P. J. Rogers, & R. Wartmann, 146–155

Lavaux, G., Afshordi, N., & Hudson, M. J. 2013, MNRAS, 430, 1617

Lavaux, G. & Hudson, M. J. 2011, MNRAS, 416, 2840

Lavaux, G., Tully, R. B., Mohayaee, R., & Colombi, S. 2010, ApJ, 709, 483

Law, N. M., Kulkarni, S. R., Dekany, R. G., et al. 2009, PASP, 121, 1395

Lemaître, G. 1927, Annales de la Société Scientifique de Bruxelles, 47, 49

Lim, S. & Lee, J. 2014, ApJ, 783, 39

Linder, E. V. 2005, Phys. Rev. D, 72, 043529

Lynden-Bell, D., Faber, S. M., Burstein, D., et al. 1988, ApJ, 326, 19

Ma, Y.-Z. & Pan, J. 2014, MNRAS, 437, 1996

Macaulay, E., Feldman, H. A., Ferreira, P. G., et al. 2012, MNRAS, 425, 1709

Magoulas, C., Springob, C. M., Colless, M., et al. 2012, MNRAS, 427, 245

Maguire, K., Sullivan, M., Pan, Y.-C., et al. 2014, MNRAS, 444, 3258

Maurellis, A., Fairall, A. P., Matravers, D. R., & Ellis, G. F. R. 1990, A&A, 229, 75

McGaugh, S. S., Schombert, J. M., Bothun, G. D., & de Blok, W. J. G. 2000, ApJ, 533, L99

Miknaitis, G., Pignata, G., Rest, A., et al. 2007, ApJ, 666, 674

Mody, K. & Hajian, A. 2012, ApJ, 758, 4

Muñoz, J. A. & Loeb, A. 2008, MNRAS, 391, 1341

Nusser, A., Branchini, E., & Davis, M. 2011, ApJ, 735, 77

Nusser, A. & Davis, M. 2011, ApJ, 736, 93

Osborne, S. J., Mak, D. S. Y., Church, S. E., & Pierpaoli, E. 2011, ApJ, 737, 98

Peebles, P. J. E. 1980, The Large-Scale Structure of the Universe (Princeton University Press)

Pereira, R. 2008, Theses, Université Paris-Diderot - Paris VII

Pereira, R., Thomas, R. C., Aldering, G., et al. 2013, A&A, 554, A27

Perlmutter, S. 2003, Physics Today, 56, 040000

Perlmutter, S., Aldering, G., Goldhaber, G., et al. 1999, ApJ, 517, 565

Phillips, M. M. 1993, ApJ, 413, L105

Pike, R. W. & Hudson, M. J. 2005, ApJ, 635, 11

Planck Collaboration Int. XIII. 2014, A&A, 561, A97

Planck Collaboration XVI. 2014, A&A, 571, A16

Rabinowitz, D., Baltay, C., Emmet, W., et al. 2003, in Bulletin of the American Astronomical Society, Vol. 35, American Astronomical Society Meeting Abstracts, 1262

Rabinowitz, D., Schwamb, M. E., Hadjiyska, E., & Tourtellotte, S. 2012, AJ, 144, 140

Rabinowitz, D., Tourtellotte, S., Rojo, P., et al. 2011, ApJ, 732, 51

Raychaudhury, S., Fabian, A. C., Edge, A. C., Jones, C., & Forman, W. 1991, MNRAS, 248, 101

Regnault, N., Conley, A., Guy, J., et al. 2009, A&A, 506, 999

Riess, A. G., Filippenko, A. V., Challis, P., et al. 1998, AJ, 116, 1009

Riess, A. G., Kirshner, R. P., Schmidt, B. P., et al. 1999, AJ, 117, 707

Riess, A. G., Macri, L., Casertano, S., et al. 2011, ApJ, 730, 119

Riess, A. G., Press, W. H., & Kirshner, R. P. 1995, ApJ, 445, L91

Riess, A. G., Press, W. H., & Kirshner, R. P. 1996, ApJ, 473, 88

Riess, A. G., Strolger, L.-G., Casertano, S., et al. 2007, ApJ, 659, 98

Riess, A. G., Strolger, L.-G., Tonry, J., et al. 2004, ApJ, 607, 665

Rigault, M., Aldering, G., Kowalski, M., et al. 2015, ApJ, 802, 20

Rigault, M., Copin, Y., Aldering, G., et al. 2013, A&A, 560, A66

Robertson, H. P. 1929, Proceedings of the National Academy of Science, 15, 822

Rubart, M. & Schwarz, D. J. 2013, A&A, 555, A117

Rugh, S. E. & Zinkernagel, H. 2000, ArXiv High Energy Physics - Theory e-prints [`arXiv:hep-th/0012253`]

Scalzo, R., Aldering, G., Antilogus, P., et al. 2012, ApJ, 757, 12

Scalzo, R. A., Aldering, G., Antilogus, P., et al. 2010, ApJ, 713, 1073

Scaramella, R. 1995, Astrophysical Letters and Communications, 32, 137

Scaramella, R., Baiesi-Pillastrini, G., Chincarini, G., Vettolani, G., & Zamorani, G. 1989, Nature, 338, 562

Schlegel, D. J., Finkbeiner, D. P., & Davis, M. 1998, ApJ, 500, 525

Schmidt, B. 1938, Mitteilungen der Hamburger Sternwarte in Bergedorf, 7, 15

Schwarz, D. J. & Weinhorst, B. 2007, A&A, 474, 717

Shapley, H. 1930, Harvard College Observatory Bulletin, 874, 9

Sheth, R. K. & Diaferio, A. 2011, MNRAS, 417, 2938

Sim, S. A., Seitenzahl, I. R., Kromer, M., et al. 2013, MNRAS, 436, 333

Springob, C. M., Magoulas, C., Colless, M., et al. 2014, MNRAS, 445, 2677

Stark, D. V., McGaugh, S. S., & Swaters, R. A. 2010, AJ, 139, 312

Strauss, M. A. & Willick, J. A. 1995, Phys. Rep., 261, 271

Stritzinger, M. D., Phillips, M. M., Boldt, L. N., et al. 2011, AJ, 142, 156

Sullivan, M., Conley, A., Howell, D. A., et al. 2010, MNRAS, 406, 782

Suzuki, N., Rubin, D., Lidman, C., et al. 2012, ApJ, 746, 85

Tonry, J. & Schneider, D. P. 1988, AJ, 96, 807

Tonry, J. L., Schmidt, B. P., Barris, B., et al. 2003, ApJ, 594, 1

Tripp, R. 1998, A&A, 331, 815

Tully, R. B. 1986, ApJ, 303, 25

Tully, R. B., Courtois, H., Hoffman, Y., & Pomarède, D. 2014, Nature, 513, 71

Tully, R. B. & Fisher, J. R. 1977, A&A, 54, 661

Tully, R. B., Shaya, E. J., Karachentsev, I. D., et al. 2008, ApJ, 676, 184

Turnbull, S. J., Hudson, M. J., Feldman, H. A., et al. 2012, MNRAS, 420, 447

Turner, M. S. 1991, Phys. Rev. D, 44, 3737

Vivas, A. K., Jaffé, Y. L., Zinn, R., et al. 2008, AJ, 136, 1645

Walker, A. G. 1933, MNRAS, 94, 159

Watkins, R. & Feldman, H. A. 2015, MNRAS, 447, 132

Watkins, R., Feldman, H. A., & Hudson, M. J. 2009, MNRAS, 392, 743

Weyant, A., Wood-Vasey, M., Wasserman, L., & Freeman, P. 2011, ApJ, 732, 65

Wiltshire, D. L., Smale, P. R., Mattsson, T., & Watkins, R. 2013, Phys. Rev. D, 88, 083529

Wood-Vasey, W. M., Miknaitis, G., Stubbs, C. W., et al. 2007, ApJ, 666, 694

Woosley, S. E., Almgren, A., Bell, J. B., et al. 2007, Journal of Physics Conference Series, 78, 012081

Zeldovich, Y. B. & Sunyaev, R. A. 1969, Ap&SS, 4, 301

List of Figures

List of Tables

List of Abbreviations

2dFGRS Two-degree-Field Galaxy Redshift Survey (`http://2dfgrs.net`).
6dFGS Six-degree-Field Galaxy Survey (`http://6dfgs.net`).

BAO baryon acoustic oscilations.

C-O WD carbon-oxygen white dwarf.
CMB cosmic microwave background.

FLRW Friedmann-Lemaître-Robertson-Walker metric of an expanding universe.

GA Great Attractor.
GR general theory of relativity.

IFU integral field unit.
iPTF intermediate Palomar Transient Factory (`http://ptf.caltech.edu/iptf`).

JLA joint light-curve analysis (Betoule et al., 2014).

kSZ kinematic Sunyev-Zeldovich effect.

LG Local Group.
LSQ La Silla/QUEST (Baltay et al., 2013).

NED NASA/IPAC Extragalactic Database (`http://ned.ipac.caltech.edu/`).

PSF point spread function.
PTF Palomar Transient Factory (`http://ptf.caltech.edu`).

SDSS Sloan Digital Sky Survey (`http://sdss.org`).
SGW Sloan Great Wall.
SN Supernova (Plural: SNe).

SN Ia Type Ia supernova (Plural: SNe Ia).

SNFACTORY Nearby Supernova Factory (Aldering et al., 2002).

SNIFS SuperNova Integral Field Spectorgraph (Lantz et al., 2004).

SNLS Supernova Legacy Survey (`http://cfht.hawaii.edu/SNLS`).

SSC Shapley supercluster.

SZ Sunyev-Zeldovich effect.

tSZ thermal Sunyev-Zeldovich effect.

ZTF Zwicky Transient Facility (`http://ptf.caltech.edu/ztf`).

Acknowledgements

I would like to take the opportunity to thank everyone who helped me along the way to this PhD thesis:

- First of all, Prof. Marek Kowalski, for the supervision of this project and his contagious enthusiasm for it;
- Dr Matthias Kerschhaggl, whose work on anisotropies laid the path for my studies;
- all my colleagues in Bonn and Berlin, who made these past years a great experience, especially my office mates and co-graduate-students Peter Greškovič, Simona Lombardo, Daniel Küsters, Dustin Hebecker;
- Dr Jakob Nordin and Dr Mickaël Rigault, for all the discussions that shaped my project near its end and for commenting on and proof-reading my thesis so thoroughly;
- all members of the SNFACTORY collaboration, especially Dr Greg Aldering, whose many comments and suggestions helped shape this analysis;
- the LSQ group at Yale, Prof. Charles Baltay, Dr David Rabinowitz, Dr Ellie Hadjiyska and Dr Nancy Ellman, for their hospitality during my research visit and the continued work on the supernova search;
- all my friends, for the great times at game nights, conventions, concerts, festivals etc.;
- and lastly, my parents, for their unending support throughout my studies.

I would also like to acknowledge support by the DFG through TRR33 “The Dark Universe” and by the Bonn-Cologne Graduate School of Physics and Astronomy.